TIME-CONTROLLED CMOS SINGLE-PHOTON AVALANCHE DIODES RECEIVERS TOWARDS OPTICAL WIRELESS COMMUNICATION APPLICATIONS

TIME-CONTROLLED CMOS SINGLE-PHOTON AVALANCHE DIODES RECEIVERS TOWARDS OPTICAL WIRELESS COMMUNICATION APPLICATIONS

By

Junzhi Liu

B. Sc. XI'AN UNIVERSITY OF POSTS AND TELECOMMUNICATIONS, 2021

A Thesis Submitted to the School of Graduate Studies in Partial Fulfilment of the Requirements for the Degree of Master of Applied Science

McMaster University
Hamilton, Ontario

Master of Applied Science (2023)
(Electrical and Computer Engineering)

TITLE: Time-Controlled CMOS single-photon avalanche diode receivers towards optical wireless communication applications

AUTHOR: Junzhi Liu,
B. Sc. Xi'an University of Posts and Telecommunications, Xi'an, China

SUPERVISOR: Dr. M. Jamal Deen

NUMBER OF PAGES: xviii, 131

Lay Abstract

Optical communication involves using light as a signal to transmit information, and it is currently a highly popular field of research. However, optical receivers used in this type of communication often require specific conditions, which can limit the overall performance of the communication system. To address this issue, we have developed an optical sensor tailored for optical communication. This sensor boasts exceptional sensitivity, allowing it to detect individual particles of light, thereby substantially reducing the demand for signal intensity in the optical communication system.

Moreover, we have devised three operational circuits that enhance the sensor's responsiveness to signals under specific communication conditions. We have created a mathematical model to evaluate the proposed optical sensor and the designed circuits, and subsequently manufactured the optical sensor. Both the simulation results and the actual test outcomes unequivocally demonstrate that our proposed sensor has the potential to enhance the performance of optical communication systems.

Abstract

Single-photon avalanche diodes (SPADs) capable of single photon detection are promising optical sensors for use as receivers in optical wireless communication (OWC) systems. In SPAD-based receivers, the intersymbol interference (ISI) effect caused by dead time is an important drawback that limits performance. In this thesis, we propose two novel SPAD operation receivers to reduce the ISI effect in SPAD-based OWC. To validate the feasibility of these two modes, we design a free-running SPAD front-end circuit with post-layout transient simulation results. This SPAD circuit is improved by a novel mixed passive-active quench and reset front-end circuit that achieves a very short dead time. Based on the traditional free-running mode, we design the clock-driven mode and time-gated mode to reduce the ISI effect through time-controlled operating signals.

In this work, we develop a new simulation system to assess the ISI effect in On-Off Keying (OOK) modulated communication and pulse position modulated (PPM) communication. To accurately evaluate these three modes, we build a OWC platform to test our proposed SPAD receiver manufactured by TSMC 65 nm process. The Test results demonstrate that the clock-driven mode and time-gated mode receivers can improve the bit error rate (BER) performance in low data rate communication and high data rate high optical power communication, respectively. Moreover, compared to the free-running mode, the two proposed time-controlled modes achieve higher data rate communication and better noise tolerance ability in SPAD-based OWC.

Acknowledgements

I would like to extend my sincerest gratitude to Dr. Jamal Deen for his invaluable assistance and guidance. His exceptional academic expertise, mentorship and excellent teaching methods have provided me with a wealth of knowledge in my field of study and enabled me to accomplish much more that I thought possible. Most importantly, I am grateful to him for granting me the opportunity to pursue this life-changing graduate experience. Furthermore, I would like to express my gratitude to Dr. Wei Jiang for his assistance in my studies and his care in my personal life. Without his support, I would not have achieved the accomplishments. I also extend my appreciation to Dr. Kumar and Dr. Kitai for their significant help in my research. Lastly, I would like to express my gratitude to all members of Dr. Deen's group who accompanied me throughout these two years. Their dedication to academic rigor and their optimistic approach to life have deeply influenced me.

I am thankful to my parents, my grandparents and other family members for their financial and emotional support. As the only child of my parents, I deeply feel their love and care for me. I want to give special thanks to my friends who are like families to me: Dian Zou, Heng Li, Minqing Yang, Qiancheng Luo, Wenxin Zhao, Yifeng Jiang, and Yuhan Sun. I love you all so much! Lastly, I want to extend my heartfelt gratitude to Yuheng Feng. Thank you for your irreplaceable companionship, having you around means a lot to me.

As a young man who is not very experienced, I walked a long way and faced many difficulties. I spent two years working hard and finally finished this thesis. I also want to thank those sleepless nights and painful moments. They have changed me and made me stronger.

Table of Contents

List of Figures

List of Tables

List of Abbreviations

AP	Afterpulsing
APD	Avalanche Photodiode
AQR	Active Quench and Reset
ASK	Amplitude-Shift Keying
BER	Bit Error Rate
BTBT	Band-To-Band Tunneling
CD	Clock-Driven
CMOS	Complementary Metal-Oxide-Semiconductor
DCR	Dark Count Rate
DFF	D-type Flip Flop
DPPM	Differential Pulse Position Modulation
ED	Event-Driven
e-h	electron-hole
FEC	Forward Error Correction
FPGA	Field-Programmable Gate Array
FR	Free-Running
Ga	Germanium
GaInAsP	Gallium Indium Arsenide Phosphide
GM	Geiger-Muller
InGaAs	Indium Gallium Arsenide
ISI	Intersymbol Interference
LD	Laser Diode
LED	Light Emitting Diode
LiFi	Light Fidelity
MIMO	Multiple Input Multiple Output
MPPM	Multi-Pulse Position Modulation

NSF	National Science Foundation
OFDM	Orthogonal Frequency Division Multiplexing
OOK	On-Off Keying
PCB	Printed Circuit Board
PCM	Pulse Code Modulation
PD	Photodiode
PDE	Photon Detection Efficiency
PDP	Photon Detection Probability
PET	Positron Emission Tomography
PPM	Pulse Position Modulation
PQR	Passive Quench and Reset
PSK	Phase-Shift Keying
QAM	Quadrature Amplitude Modulation
SDO	Software Defined Optics
Si	Silicon
SMA	SubMiniature version A
SNR	Signal-to-Noise Ratio
SPAD	Single-Photon Avalanche Diode
TAT	Trap-Assisted Tunneling
TG	Time-Gated
UWOC	Underwater Wireless Optical Communication

List of Symbols

a	Ionization coefficient
A_i	The constant of the i^{th} energy trap
b	Ionization coefficient
c	Ionization coefficient
d	Ionization coefficient
E	Electric field [eV]
f_0	The frequency of incident photon [Hz]
G_L	The generation rate and of excess carriers
h	The Plank constant (= $6.62607015 \times 10^{-34}$ m^2 kg / s)
k	The number of detected photons
k_{max}	The maximum value of detected photons
L	The average photon arrival rate
L_e	The effective count rate of SPAD receiver
N	The number of SPAD pixels in a SPAD array
n_0	The concentration of electron in dark condition
$P_{ap}(t)$	The afterpulsing probability
$P(k)$	The photon count probability
p_o	The concentration of hole in dark condition [cm^{-3}]
P_R	The received optical power [W]
q	The charge of an electron (= 1.6×10^{-19} C)
R_Q	Quench resistor [Ω]
T	Time interval [s]
T_b	The block time [s]
T_d	The dead time [s]
T_S	The bit time interval [s]
V^+	The threshold of state ‘1’ in Schmitt trigger [V]

V^-	The threshold of state '0' in Schmitt trigger [V]
V_C	The cathode voltage of SPAD [V]
V_{CON}	The control voltage of SPAD circuit [V]
V_{HV}	The anode voltage of SPAD [V]
V_{OUT}	The output of SPAD circuit [V]
V_{TN1}	The threshold voltages of N1 transistor [V]
V_{TP1}	The threshold voltages of P1 transistor [V]
w	The thickness of the multiplication layer [m]
α	The impact ionization rate of electron
β	The impact ionization rate of hole
β_{N1}	The width and length ratio of transistor N1
β_{N3}	The width and length ratio of transistor N3
β_{P3}	The width and length ratio of transistor P1
β_{P3}	The width and length ratio of transistor P3
Δn	Non-equilibrium electron concentration [cm^{-3}]
Δp	Non-equilibrium hole concentration [cm^{-3}]
μ_n	The Mobility of electron [$cm^2 V^{-1}s^{-1}$]
μ_p	The Mobility of hole [$cm^2 V^{-1}s^{-1}$]
μ_j	The mean of photon count distribution of the j^{th} bit
σ_j^2	The variance of photon count distribution of the j^{th} bit
τ	The fixed delay element
τ_i	The de-trap time of the i^{th} trap [s]
τ_p	The excess minority carrier lifetime [s]

Declaration of Academic Achievement

This thesis was written by Junzhi Liu under the supervision and guidance of Dr. M. Jamal Deen from McMaster University.

- **Chapters 1 and 2:** I conducted a literature review on sensors for optical wireless communication applications with a focus on single-photon avalanche diode (SPAD) based receiver.
- **Chapter 3:** I designed the time-controlled SPAD receivers in 3 operation modes with the introduction of the front-end circuits, data process circuits and the layout design.
- **Chapter 4:** I analysed the photon count process of SPAD and built a SPAD-based OWC model with ISI effect analysis to simulate the 3 proposed SPAD receivers. The Monte-Carlo simulation method is used to get the bit error rates (BERs) of these SPAD receivers in different communication conditions and different modulations.
- **Chapter 5:** I designed a OWC test platform and measured a SPAD pixel with proposed front-end circuit using a standard TSMC 65 nm CMOS process. The basic SPAD parameters are measured and the BERs of 3 SPAD receivers are tested by the OWC platform. In this work, Tyler Ackland assembled the printed circuit board needed for the measurements.
- **Chapter 6:** I wrote a conclusion of this thesis, and discussed 3 key research fields for the future work.

Chapter 1
Introduction

1.1. Optical Wireless Communication

1.1.1. Concept of Optical Wireless Communication

Optical Wireless Communication (OWC) or Optical Communication, is a cutting-edge wireless communication technology that utilizes optical signals to transmit information. In the context of the rapid development of wireless internet, the people's daily lives and productivity are closely interconnected with wireless technologies. With the rapid evolution of mobile terminal devices, the advancements in 5G technology, and the groundbreaking progress in emerging fields like artificial intelligence and big data, the demand for high-quality wireless communication has escalated. Figure 1-1 illustrates the growth of global mobile data transmission over the past six years (2017-2022) on a monthly basis. In 2017, the world's monthly mobile data transmission volume stood at 11.51 exabytes, and by 2022, this number had escalated to 77.49 exabytes. Over this six-year period, the annual growth rate reached an impressive 46% [1]. The congestion of the radio frequency spectrum has been caused by these developments, which is particularly evident in indoor and space wireless radio transmissions [2]. To address the saturation issue faced by the radio frequency spectrum, various techniques have been developed, such as spectrum sharing and intelligent spectrum management [3], [4]. Among these techniques, Optical Wireless Communication (OWC) is considered to have promising prospects for alleviating the current wireless communication challenges. By modulating the intensity, frequency, or phase of light signals, OWC can carry data, offering high data transmission rates and bandwidth [5].

The field of OWC has captured the interest of numerous research institutions and scholars worldwide. One noteworthy European initiative in OWC research is the IC1101 OPTICWISE project under the COST Programme (European Cooperation in Science and Technology), which is funded by the European Science Foundation. This project facilitates the coordination of nationally funded research efforts on a European scale, with the goal of establishing a prominent interdisciplinary platform for OWC research activities. Initiated in November 2011, the project is set to continue until November 2015 and involves participation from over 20 countries [6]. In the United States, several OWC endeavors have also emerged. Among these is the "Smart Lighting Engineering Research Center," established in 2008 through funding from the National Science Foundation (NSF). This center operates as a collaboration between Rensselaer Polytechnic Institute (as the lead institution), Boston University, and the University of New Mexico. Additionally, outreach partnerships have been formed with Howard University, Morgan State University, and Rose-Hulman Institute of Technology [7]. Notably, in July 2023, IEEE introduced the 802.11bb standard, which provides guidelines for optical networking in the 800–1000 nm band, focusing online-of-

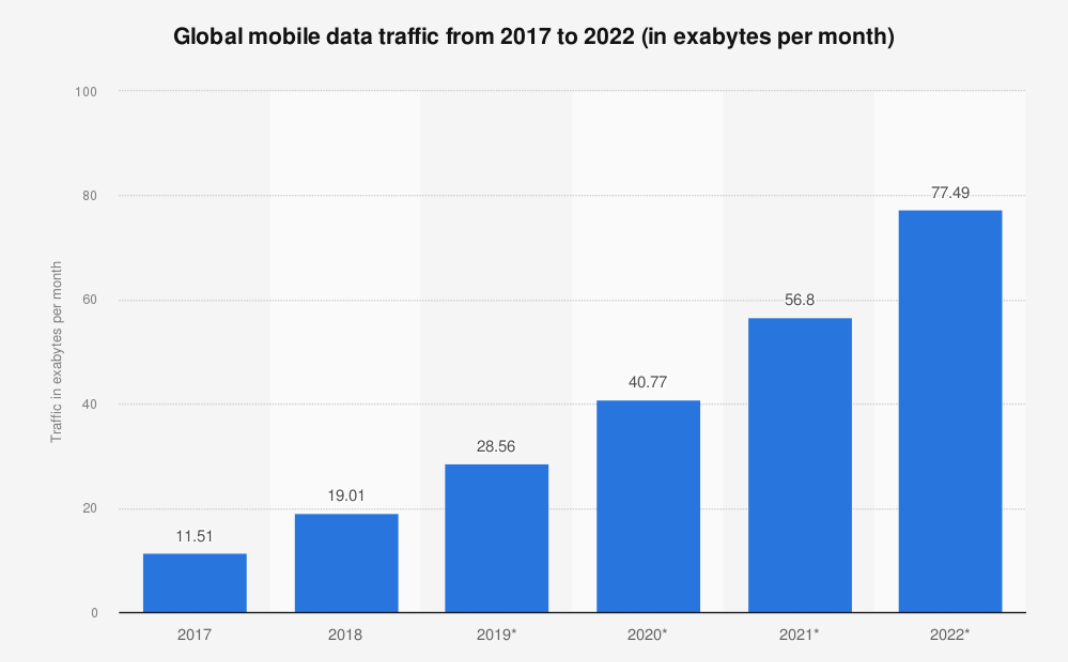

Figure 1-1: Global mobile data traffic [1].

sight applications [8]. As early as the 1960s, laser communication attracted considerable attention from scientists. In 1962, the Hughes group achieved sound transmission over 30 km using laser communication, in 1966, the wide-band pulse code modulation (PCM) was first used in laser communication [9]. By the 1990s, visible light was utilized for wireless communication, and it was known as "Li-Fi" [10].

OWC technology is being tested and applied in an increasing number of fields, as shown in Figures 1-2. For the optical satellite communication, over 30 years of research and application have made OWC mature and reliable in this field. In recent years, with the rapid growth of information flow demand, satellite communication technology using microwaves as the information carrier has gradually shown limitations in increasing communication data rates. In contrast, satellite optical communication technology has many advantages over satellite microwave communication technology, such as smaller equipment size, strong interference resistance, and higher confidentiality [11]. Furthermore, it offers significant potential for increasing communication data rates. Kaur et al. (2012) achieved a communication distance of 5000 km at a data rate of 10 Gbps [12]. Another study (Ref. [13]) demonstrated the application of OWC in the Ground-to-satellite link, where a laser transmitter was implemented in low-earth orbit and geostationary orbit, enabling long-distance transmission at the order of Gbps data rates [14].

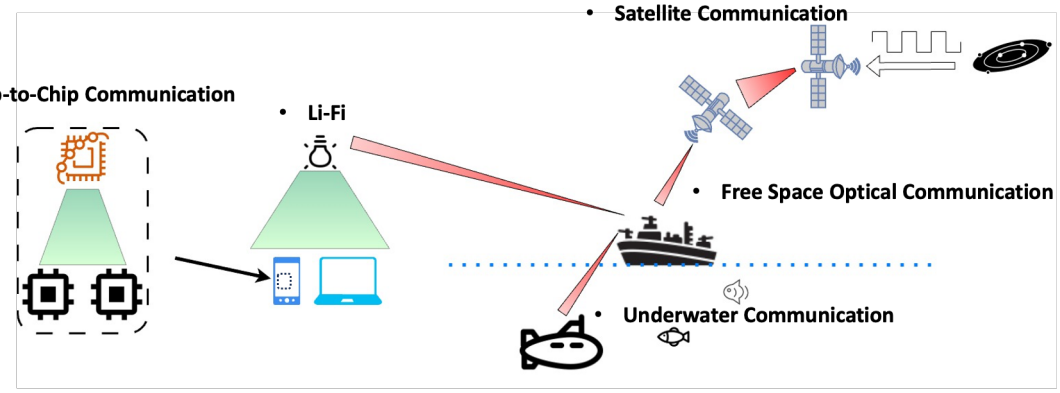

Figure 1-2: The main applications of Optical Wireless Communication

RF communication in underwater environments faces challenges due to high signal attenuation, multipath propagation, scattering, Doppler effects, and limited bandwidth. These

limitations affect data rate, transmission range, and signal quality [15]. To address these limitations, underwater wireless optical communication (UWOC) has emerged as a promising alternative for OWC in this domain. UWOC utilizes optical signals, such as laser light, to transmit data through the water medium [16]. Unlike traditional RF and acoustic communication, optical communication in water encounters lower attenuation, enabling higher data rates and longer communication distances. Y. Huang's group realized 10.8 Gbps data rate in 10.2 m communication distance [17]. J. Wang's group realized 100m communication distance with 500 Mbps data rate [18]. In 2020, a team in Fudan University uses SPAD as the receiver to build a UWOC system that realized 500bps data rate in 144m distance and 2 Mbps in 117m distance [19]

Light Fidelity (LiFi) is an emerging wireless transmission technology that exploits the visible light spectrum, leveraging light sources like LEDs to facilitate data communication [20]. As a part of OWC research, LiFi exhibits distinctive characteristics, including bidirectional communication, multiuser capability, and mobility support [21]. Moreover, LiFi can coexist with RF-based networks without mutual interference [22]. Comparatively, LiFi boasts higher data rates and lower power consumption than WiFi. LiFi can simultaneously provide both lighting and communication, making it suitable for applications in smart cities, such as intelligent transportation systems and smart lighting systems, offering more solutions for interconnectivity within the city. Furthermore, LiFi has vast potential in high-speed mobile communication fields, such as high-speed trains and autonomous driving scenarios. LiFi can overcome the limitations of traditional wireless communication affected by multipath effects, achieving higher data transmission efficiency and lower latency, thus enabling more reliable communication. In recent research, LiFi systems utilizing LEDs and LDs achieved a remarkable data rate of 488 Gbps [23], while a SPAD-based LiFi system, integrating a SPAD array within a 130 nm complementary metal-oxide-semiconductor (CMOS) image sensor technology, achieved 480 Mbps in an ambient light intensity of 1 klx [24].

The chip-to-chip optical communication or intra-chip optical communication enables high-speed, low-latency, and energy-efficient data exchange between different components

on a single circuit board or within a multi-chip module [25]. By employing light as the information carrier, chip-to-chip optical communication offers advantages over traditional electrical interconnects, such as higher data rates, reduced electromagnetic interference, and lower power consumption. In chip-to-chip optical communication, data is transmitted in the form of optical pulses. The data signals are modulated onto the optical carrier, and the optical pulses are then transmitted through the waveguides to the receiving chip [26]. At the receiving end, the optical pulses are detected and demodulated to recover the original data. IBM has developed chip-to-chip optical communication technology using silicon photonics. In one of their demonstrations, they achieved data transfer rates of 100 Gbps between two chips placed in proximity on a silicon wafer [27]. Intel has also been working on integrated silicon photonics for chip-to-chip communication. They demonstrated a 50 Gbps optical link between two chips, using a silicon photonic modulator and detector [28].

OWC stands as a promising technology with numerous advantages in modern communication systems. One of its key benefits lies in the ability to achieve high-speed data transmission, surpassing traditional RF methods. With its use of the visible light spectrum and infrared signals, OWC offers a wide bandwidth, enabling greater data capacity and facilitating multi-user communications. Additionally, OWC ensures enhanced security, as light signals do not penetrate walls, providing inherent protection against eavesdropping. The low electromagnetic interference of OWC also reduces the likelihood of signal interference, making it suitable for deployment in densely populated urban areas or sensitive environments. Furthermore, OWC presents energy-efficient solutions, utilizing LEDs for data transmission, which contributes to overall energy conservation. Its dual functionality in both illumination and communication lends itself to smart city applications, supporting intelligent traffic systems and smart lighting solutions.

OWC, while offering several advantages, also faces certain challenges and limitations. One significant limitation is the susceptibility to atmospheric conditions. Optical signals are highly susceptible to atmospheric disturbances, such as fog, rain, and other adverse weather conditions, which can cause signal attenuation and hinder reliable communication [29]. In addition, optical signals are susceptible to atmospheric absorption and scattering, leading to

limited transmission distance in OWC systems. Over long-distance transmission, the signal strength can significantly decrease. Moreover, the interference caused by ambient lighting sources, especially in indoor environments with varying lighting conditions, impacting the reliability of data transmission. OWC typically employs directional transmission, requiring precise alignment between the transmitting and receiving devices, which adds complexity to system deployment and maintenance.

With the development of OWC, high-speed transmission, high stability and low power consumption have become important research topics. In recent years, an increasing number of technological innovations have been applied to the field of OWC. For example, multiple input multiple output (MIMO) technology increases communication channels in space, enhancing data transmission rates and reliability. Adaptive modulation technology enables OWC systems to automatically adjust parameters based on channel conditions and environmental changes, optimizing system performance. Software Defined Optics (SDO) technology allows flexible configuration of optical resources, improving the flexibility and controllability of optical signal transmission.

1.1.2. Components in Optical Wireless Communication System

An OWC system primarily comprises a transmitter, an optical channel, and a receiver. These components collectively facilitate the transmission of information through optical signals [30]. As shown in the Figure 1-3. The transmitter encodes electrical signal onto optical signals for transmission. The optical channel functions as the propagation medium for

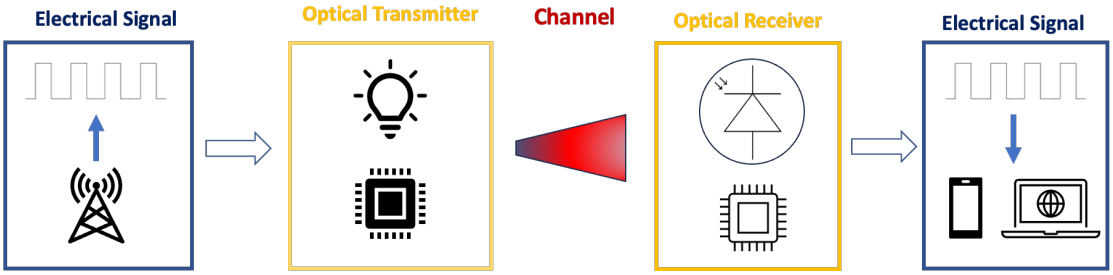

Figure 1-3: The components of an optical wireless communication (OWC) system.

transmitting the optical signals. The receiver captures and decodes the received optical signals back into electrical data.

A. Transmitter

The light emitting diodes (LEDs) and Laser Diodes (LDs) are two semiconductor devices commonly utilized as the transmitters in OWC system. The two devices operated based on distinct principles of light emission and resulting different characteristics. LEDs generate light through spontaneous recombination of charge carriers within a semiconductor material, producing incoherent light with a broad spectrum [31]. This property makes LEDs suitable for applications like indicator lights, display backlighting, and short-range OWC due to their energy efficiency and cost-effectiveness. LDs produce coherent light through stimulated emission, resulting in a narrow and well-defined spectral output [32]. This coherence allows LDs to create intense, focused beams, making them ideal for applications requiring high data rates and long-range transmission, such as high-speed OWC links, fiber optic communication, and laser-based medical treatments.

Table 1-1: Advantages and limitations of LED and LD

	LED	LD
Advantage	a. High energy efficiency. b. longer life span. c. Switching light intensities rapidly;	a. Lasers are monochromatic and Coherent. b. Light can travel long distances. c. higher data rate;
Limitation	a. Light is incoherent. b. Low optical power transmitted. c. Easy to cause interference;	a. low aperture. b. has possible health threats;

As widely employed receivers in the field of OWC, LEDs and LDs exhibit distinct characteristics in terms of transmission speed, transmission distance, and bit error rate. When used as transmitters, LEDs demonstrate lower radiative efficiency and wider spectral features, resulting in lower transmission speeds suitable for low data rates and short-range communication [33]. Nevertheless, their simplicity, cost-effectiveness, and adaptability confer advantages in scenarios like indoor communication. Conversely, LDs, functioning as

receivers, capitalize on their high energy density, narrow spectral features, and high modulation bandwidth, allowing for higher transmission speeds and longer transmission distances [33]. The laser properties of LDs confer directionality, making them apt for point-to-point communication, although their sensitivity to pointing errors is a trade-off. Due to external factors affecting the transition process between excited and ground states, LDs may experience elevated bit error rates during long-distance transmissions.

B. Communication Channel

In OWC communication systems, communication channels refer to the transmission pathways of optical signals between transmitters and receivers. As depicted in Figure 1-2, these channels primarily include space optical channels, free-space optical channels, indoor optical channels, and underwater optical channels.

Optical signals propagate differently across various channels, experiencing distinct influences. In the Space Optical Channel, optical signals traverse the space, susceptible to factors like space environment and interstellar background radiation. In the Free-Space Optical Channel, optical signals propagate through the atmosphere, being impacted by atmospheric absorption, scattering, and turbulence, thereby affecting transmission distance and quality. Channels employed for indoor communications are generally unaffected by atmospheric conditions. However, indoor channels can be influenced by reflections and scattering caused by objects like walls and furniture. Underwater optical transmission faces challenges such as water absorption and scattering, resulting in limited transmission distances and the need to account for water quality and environmental factors.

C. Receiver

The receiver in the OWC system typically consists of a high-performance photodetector that can detect and convert incoming optical signals into electrical pulses. Following detection, the received signal is subjected to further processing stages, including amplification, filtering, and signal conditioning, to enhance its quality and prepare it for subsequent demodulation and decoding [34]. The choice of receiver architecture and components is influenced by the specific application requirements, desired data rates, environmental conditions, and the characteristics of the transmitted optical signal [34].

Advanced receiver designs, adaptive algorithms, and error correction techniques are frequently employed to mitigate impairments induced by noise, channel attenuation, and other sources of signal degradation, thereby enhancing the overall reliability and performance of the OWC system.

Table 1-2: Comparison of different OWC systems

	[35]	[36]	[37]	[36], [38]	[38]	[37]
Data Rate	400Mbps	2 Mbps	200 Mbps	800 Kbps	3 Gbps	5.6Gbps
Distance	5 m	1.2 km	2 m	333.362 m	1300 km	5000 km
BER	2×10^{-3}	10^{-6}	1×10^{-3}	1.22×10^{-3}	10^{-47}	10^{-16}
Receiver	4-SPAD Array	SPAD	128×32 SPAD for each channel	SPAD-based	APD	APD+LPF
Transmitter	RC LED (650nm)	LED	RGB LED	single red LED (630nm)	Continuous-wave Laser (1550nm)	Continuous-wave Laser(1550nm)
Modulation	NRZ	NRZ-OOK	DCO-OFDM	——	NRZ	NRZ

In OWC applications, the choice of receivers holds paramount importance. The selection of receivers depends on the specific application scenarios. In indoor environments with limited optical power, Therefore, highly sensitive optical sensors, such as single photon avalanche diodes (SPADs), can be employed as receivers. For outdoor settings, where longer distances and varying atmospheric conditions are challenges, avalanche photodiodes (APDs) are favored as receivers, because they enhance signal detection in such scenarios.

In general, OWC has a wide range of application scenarios, and the choice of transmitter and receiver may vary with changing conditions. Table 1-2 summarizes recent research, validating our analysis. Compared to OWC systems based on APDs and lasers, OWC systems based on photon counting technologies such as SPAD and LEDs often achieve shorter communication distances, higher error rates, and lower data rates. However, this does not imply a lack of advantages in such combinations. For instance, in indoor OWC scenarios, the combination of photon counting and LEDs presents a safer and more cost-effective choice.

Therefore, the judicious selection of transmitters and receivers is crucial in OWC applications [35].

1.2. Photosensors for OWC Receivers

A photosensor is a detector that can convert light signal to electrical signal [39]. As the receiver in OWC system, photosensor is regarded as the key component that can determine the whole OWC system performance. Semiconductor photosensors, especially fabricated by CMOS technology, are widely used optical receivers due to their high integration, high stability and low cost [30]. As p-n junctions under different bias voltages, photodetector (PD), APD and SPAD are most employed in OWC system. The light signal is converted to current signal or voltage signal by the read-out circuits due to the gains of these three devices are different [40].

1.2.1. Photodiode (PD)

Photodiodes (PDs) detect light signal by converting photon energy into electrical current. In the past few years, PD is regarded as a promising receiver for OWC and was included in the IEEE standard (802.15.13) [29]. As a simple p-n junction, PD is biased reversely, and a very limited reverse current can be generated in the diode under dark environment [41]. The incident photons generate photocurrent that linearly proportional to the optical power. It is worth noting that one photon can be absorbed when the photon energy equal or higher than the width of band gap in the semiconductor material (Figure 1-4. (a)).

When photon comes, the semiconductor materials in PD usually strongly absorb light energy and excite electron to transition from a lower energy level to a higher energy level, thus causing an electron-hole pair, as shown in Figure 1-4. (a) [42]. When excess electrons and holes are generated in a semiconductor, there is an increase in the conductivity of the material, which is the basis of photoconductor [43]. the conductivity with illumination can be written as:

$$\sigma = q(n\mu_n + p\mu_p) \tag{1-1}$$

where $n = \Delta n + n_0$ and $p = \Delta p + p_0$, n_0 and p_o are the concentrations of electron and hole in dark condition, Δn and Δp are the non-equilibrium carries concentrations, μ_n and μ_p are the mobilities of electron and hole, the q is the electron charge. We can consider an n-type semiconductor ($\Delta n = \Delta p$) and the concentration of excess carriers is Δp that can be given by $\Delta p = G_L \tau_p$, that G_L is the generation rate and of excess carriers and τ_p is the excess minority carrier lifetime. The current density of the semiconductor will be increased due to the increase of conductivity, leading the photocurrent is directly proportional to the excess carrier generation rate, that is proportional to the incident photon flux [43].

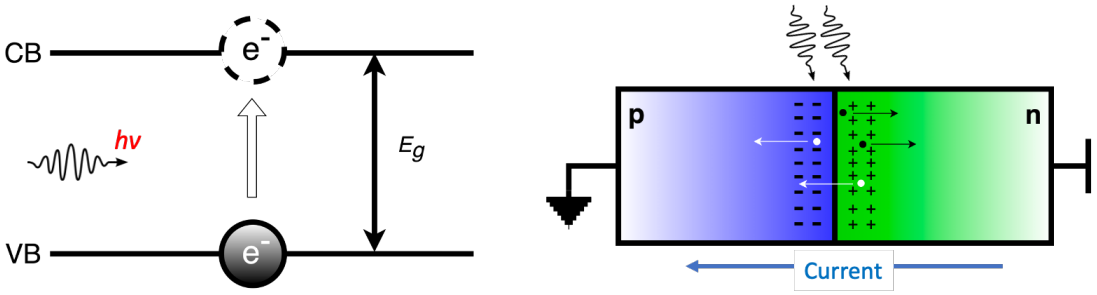

Figure 1-4: (a) Simplified conventional structure; (b) Simplified high-voltage biasing network.

When light of a specific wavelength illuminates the p-n junction, the built-in electric field resulting from the non-uniformity of the semiconductor material induces an electromotive force, known as the photogenerated voltage. If the p-n junction is short-circuited, a photogenerated current will flow. Due to the built-in field in the p-n junction barrier region, the photogenerated carriers on both sides of the p-n junction are affected by the electric field and move to opposite directions. It is equivalent to adding a forward voltage at both ends of the p-n junction and generate forward current [44]. This phenomenon is defined as the photoelectric effect, as shown in Figure 1-4. (b).

The PD is always reliable due to operate in a low bias voltage, thus causing a low noise level [45]. In PD receiver, the thermal noise plays the dominant role, as a comparison, APD receiver suffers from the effects of thermal noise and shot noise [46]. On the other hand, PD is cheap and easy to fabricate, which make PD is s good optical receiver [46]. However, the gain of PD receiver is 1, results in a low sensitivity [40]. In the domain of OWC, PDs serve

as a prevalent type of detector suitable for indoor optical communication scenarios [47]. Furthermore, the advantageous attribute of low noise levels associated with PDs has positioned them effectively within the ambit of OWC applications in the medical domain [48]. In conclusion, the PD is suitable for low-bandwidth and short distance OWC applications [46].

1.2.2. Avalanche Photodiode (APD)

When the p-n junction is in reverse bias, the reverse current flowing through the p-n junction is mainly composed of the electron current diffused from the p region into the barrier region and the hole current diffused from the n region into the barrier region [42]. When a p-n junction diode is biased by a high reversed voltage (close to the breakdown voltage), the electric field in the barrier region is very strong, any free electrons or holes in the barrier region will have a high kinetic energy when drifting in the strong electric field. When the high-energy carriers collide with lattice atoms, the electrons in the valence band can be excited out to the conduction band to become free electrons, leaving a hole in the valence band, thus creating electron-hole pairs. As shown in Figure 1-5, in the p-n junction barrier region, photo-introduce electron 1 collides with lattice in barrier region and generates an electron 2 and a hole 2. These three carriers (electrons and holes), move in opposite directions under the strong electric field, and will continue to collide and generate the third generation of electron-hole pairs. If the process continues, the carriers will increase

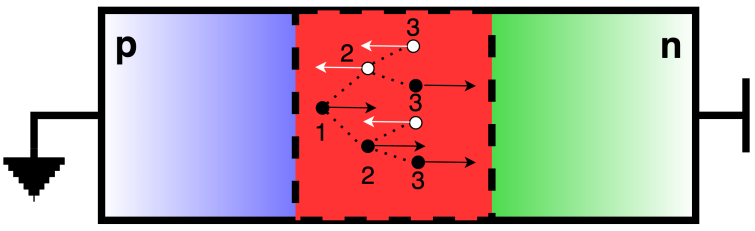

Figure 1-5: The schematic of avalanche breakdown process in p-n junction

in large quantities [43]. This way of multiplying carriers is called the multiplication effect of carriers. Due to the multiplication effect, a large number of carriers are generated. The

reverse current is rapidly increased, resulting in p-n junction breakdown, which is the avalanche breakdown [49].

APDs have a key advantage of superior sensitivity due to their internal gain mechanism. In APDs, the ionization rate is defined as the number of electron-hole pairs generated by a carriers per unit distance travelled [50]. The ionization rate only depends on the local electric field, and the impact ionization rate of electron α and hole β can be expressed as [49]:

$$\alpha = ae^{-b/E} \tag{1-2}$$

$$\beta = ce^{-d/E} \tag{1-3}$$

The a, b, c, d, are ionization coefficients and E is the electric field. Higher electric fields help the carriers to gain the required energy for ionization over a smaller distance, and therefore increase the ionization rate. We assume that every collision between carriers and the lattice in the multiplication region is an ionization collision, and the number of collisions is equal to the number of electron-hole pairs that collide. Therefore, the average total number of electron-hole pairs generated by an initial pair formed at x can be given by [49]:

$$M(x) = 1 + \int_0^x \alpha M(x') \cdot dx' + \int_x^w \beta M(x') \cdot dx' \tag{1-4}$$

Where the w is the thickness of the multiplication layer and $0 < x < w$. The output of APD is the current with the intensity linearly proportional to the incident optical power. Compared with PD, high gain in APD brings high sensitivity and extends the applications into low illuminant environment. The avalanche built-up time and dark current are two parameters that can affect the APD receiver performance and depend on the APD materials and structure [51]–[53]. Typical photodiode materials are Silicon (Si), Germanium (Ga), Gallium Indium Arsenide Phosphide (GaInAsP), Indium Gallium Arsenide (InGaAs) [49], and the mainly structures of APDs are reach-through APD and guard ring APD [54], [55]

Typical applications for APDs are laser rangefinders, long-range fiber-optic telecommunication, and quantum sensing for control algorithms. New applications include positron emission tomography (PET) and particle physics [56]. In the application of OWC,

APDs are implemented into high-speed communication and low optical power communication due to the high SNR performance and the high sensitivity.

1.2.3. Single-photon Avalanche Diode (SPAD)

When a APD is operated into Geiger mode, the sensitivity of APD increases sharply to make APD has single photon detection ability [57]. Due to the reverse bias voltage of SPAD

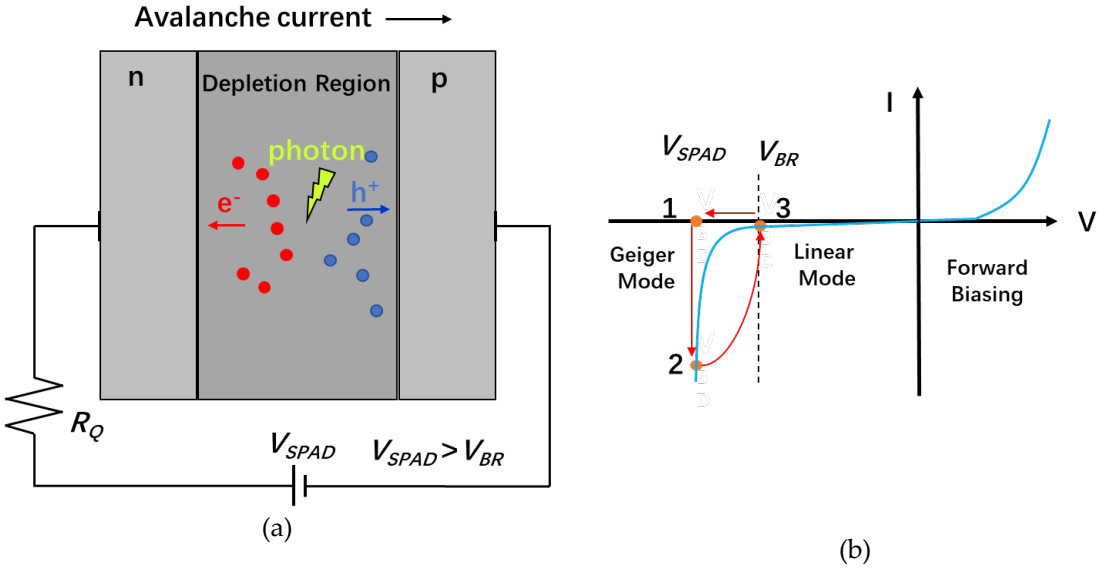

Figure 1-6: Principle of SPAD operation: (a) Avalanche breakdown process in a reverse biased p-n junction; (b) I-V characteristic representation of SPAD operation.

higher than the breakdown voltage, a high electric field across the depletion region is generated [58]. In such a high electric field situation, avalanche can be triggered by even a single carrier (photon or dark noise) [59]. As shown in Figure 1-6, in step 1, self-sustained avalanche breakdown in SPAD brings an infinite gain, causing extensive charges go through the SPAD. In step 2, A drop in the bias voltage on SPAD is leaded due to the resistor R_Q is connected with the SPAD in series. When the bias voltage on the SPAD is lower than the breakdown voltage, the carriers in depletion region cannot accept enough kinetic energy to continue the avalanche, thus bringing a recover on the bias voltage. The dead time is defined as the time of carrier detection period which is highly related with the quench and reset circuit. The SPAD dead time remains from a few nanoseconds to hundreds of microseconds [60].

Other important parameters in SPAD include the dark count rate (DCR), the afterpulsing probability and the photon detection efficiency (PDE). These parameters effect the OWC system performance deeply and will be discussed in Chapter 2.

In the past few decades, SPAD is widely used in the applications of photon-counting, photon-timing and imaging [59], [61] With the development of OWC, SPAD has attracted considerable interests as the receiver in OWC systems [62]. For examples, a SPAD-based receiver achieved 117 m transmission distance and 2 Mbps data rate communication in an underwater OWC application [19]. A 64 × 64 SPAD receiver manufactured in CMOS technology was used in an OWC system for 500 Mb/s data rate transmission with only -46.1 dBm received optical power [63]. The maximum 3.45 Gbit/s data rate with on-off keying (OOK) and 5 Gbps with orthogonal frequency division multiplexing (OFDM) were demonstrated using commercial SPAD arrays [34], [64]. As a receiver in OWC system, SPAD benefits from its extremely high gain (more than 10^6) and very fast photon response speed, causing an excellent performance in low illumination communication. However, the low ambient light tolerance and long dead time restrict the receiver performance in high background illumination and high data rate communication conditions.

1.3. My Contributions

In this study, we devised three SPAD circuits for OWC. Based on the distinct characteristics of these circuits, we built three simulation models to simulate their performance across various optical communication conditions. Subsequently, we employed a standard CMOS process to fabricate SPAD receivers rooted in these three circuits. Additionally, an OWC testing platform was established to validate the functionality and real-world performance of the circuits. The main contributions of this work are the following:

- **A mixed passive-active quench and reset SPAD front-end circuit.** We design a SPAD front-end circuit that accomplishes fast quenching and rapid resetting, achieving a minimal dead time of only 2.6 ns. Additionally, we introduce voltage-

controlled capabilities into the circuit through Schmitt triggers to enable adjustable dead time.

- **Two time-controlled modes circuits.** In order to optimize the performance of the SPAD receiver, two types of time-controlled modes were designed and implemented. Based on the fundamental mixed passive-active quench and reset SPAD front-end circuit, the signal generation circuits and front-end circuits for Clock-driven (CD) mode and time-gated (TG) mode were designed.
- **The SPAD Receivers.** Utilizing the TSMC 65 nm process, two sets of 16-SPAD receivers (CD and TG) were designed and fabricated. Through circuit design, each receiver can be configured to operate in both free-running (FR) mode and time-controlled mode. The chip also incorporates additional control functionalities to ensure chip performance and meet testing requirements.
- **Three SPAD-based OWC models.** We established three sets of OWC communication models to analyze the performance and characteristics of FR mode, CD mode, and TG mode SPAD receivers. We also developed a novel simulation method for analyzing Intersymbol Interference (ISI), which enhances the accuracy of the SPAD-based OWC model.

Publications:

Published:

1. J. Liu, W. Jiang and M. J. Deen, "Time-Gated Circuit for SPAD-based OWC," 2022 IEEE Photonics Conference (IPC), Vancouver, BC, Canada, 2022, pp. 1-2, doi: 10.1109/IPC53466.2022.9975721.
2. J. Liu, W. Jiang, S. Kumar and M. J. Deen, "Time-Controlled SPAD Receivers in Optical Wireless Communication System," in IEEE Photonics Journal, doi: 10.1109/JPHOT.2023.3309881.

1.4. Thesis Organization

In Chapter 1, the historical background, and applications of OWC are reviewed, and the impacts of transmitters, channels, and receivers on the overall performance of OWC are

analysed. Three types of photodetectors are introduced in the order of bias voltage magnitude, explaining their operating principles and respective characteristics, as well as their application scenarios as OWC receivers.

In Chapter 2, several key parameters of SPAD are introduced, and the impact of each parameter on the performance of SPAD receivers is analyzed, as well as the interactions among different parameters. Furthermore, the operating principles and characteristics of active quench and reset (AQR) SPAD circuits and passive quench and reset (PQR) SPAD circuits are explained. Additionally, building upon the AQR SPAD circuit, two types of time-controlled SPAD circuits (clock-driven (CD) and time-gated (TG)) are introduced.

The receiver design Is presented in Chapter 3, where the operational principles of the three front-end circuits are explained and simulated. The hold-off time control circuit based on the Schmitt trigger is introduced, and two signal generation circuits (CD and TG) are shown. The characteristics of these modes are analyzed through circuit simulations. In addition, this chapter includes the photon counter based on D-flip-flop and the data processing circuit based on an adder tree. The final layout of the circuit is also presented.

In Chapter 4, the SPAD-based OWC communication model based on Geiger-mode photodetectors is presented. The photon count probability distribution is derived within a fixed time interval, and the impact of parameters in the OWC model on system performance is simulated. In this chapter, a novel Intersymbol Interference (ISI) simulation model is introduced and integrated into the OWC model, enhancing its accuracy. A receiver model with a 64-SPAD array is applied to the OWC model based on on-off Keying (OOK) modulation, and a receiver with a 16-SPAD array is applied to the OWC model based on pulse position modulation (PPM). The analysis of simulation results is also showcased in this chapter.

Chapter 5 shows the results of receivers testing, where an OWC test platform is established, consisting of an LED transmitter and the proposed SPAD receiver. Some parameters of the SPAD are tested, and the SPAD receiver bit error rate (BER) is computed and analyzed for both on-off keying (OOK) and pulse position modulation (PPM)

modulations, by varying signal power, background power, and data rate. Chapter 6 concludes the content of the thesis and outlines three potential directions for future research.

Chapter 2
Performance Parameters for SPAD

2.1. Key Performance Parameters

2.1.1. Breakdown Voltage

The breakdown voltage is a critical and fundamental parameter in SPAD, it represents the applied bias voltage at which the SPAD transitions from its quiescent state to the active avalanche breakdown state [65]. The breakdown voltage determines the sensitivity of SPAD, and it is essential for optimizing the performance and operating conditions of SPADs. When SPAD is biased beyond the breakdown voltage, the SPAD operates in the Geiger mode, where a single photon incident on the device can trigger a self-sustaining avalanche process, leading to a detectable electrical signal. During breakdown, the SPAD experiences a rapid increase in current due to the generation of electron-hole pairs by impact ionization, resulting in a highly sensitive photon detection capability. The excess voltage of SPAD is the difference between the applied bias voltage and the breakdown voltage, and when the excess is positive, the gain of the SPAD can be very high, leading to a strong avalanche effect.

The structure and materials of SPADs have a significant impact on their breakdown voltage. Research indicates that structural parameters of SPADs, such as the doping concentration and geometric dimensions of the P-N junction, as well as the choice of materials such as Si and Ge, influence the magnitude of the breakdown voltage. For instance, the geometric parameters and doping concentration of the p-n junction allows for tailored control of the SPAD breakdown voltage to achieve customized performance [66]. Moreover, the selection of different materials significantly impacts the SPAD breakdown voltage. Ge, with its smaller energy gap, enables lower breakdown voltages and enhances the sensitivity of the SPAD. In summary, the structural parameters and material choices of

SPADs play a pivotal role in regulating and optimizing the breakdown voltage. In the CMOS SPAD, the breakdown voltage increases with the junction scaling up and highly related with the doping concentration. The temperature coefficient is another important factor to affect the breakdown voltage, as the phonon scattering at high temperature prevents the charge carriers to reach the energy threshold to avalanche [67].

The excess voltage is highly related with the other parameters of SPAD. For example, the DCR and the photon detection probability (PDP) are positively correlated with the excess voltage, however, the DCR and the PDP have opposite effects on the performance of SPAD receiver [68]. In the SPAD-based OWC systems, an accurate breakdown voltage measurement contributes to the setting of excess voltage for optimal the performance of SPAD receivers.

2.1.2. Dark Count Rate

DCR is the rate of the avalanches triggered by non-photons. Dark counts occur because of the thermal excitation, where minority carriers in the bulk region may move into the depletion region by diffusion and trigger avalanches [69]. Due to the presence of impurities associated with SPAD fabrication in the CMOS process, a significant number of forbidden energy levels within the bandgap can trap and later release charges, thereby increasing the overall DCR. Processes that have a notable impact on the total DCR include trap-assisted thermal generation, trap-assisted tunneling generation (TAT), and band-to-band tunneling (BTBT) [70].

Non-uniformity in junction quality and doping concentration can cause variations in local electric fields, affecting the rates of electron-hole pair generation and recombination, thereby influencing DCR. The DCR are affected by the operation temperature, as the free carriers are thermally generated in the depletion region, thus causing the dark counts [71]. At elevated temperatures, the rate of electron-hole pair generation may increase, consequently elevating the likelihood of dark count events. The excess voltage on the SPAD determines the electric field across the SPAD junction. The DCR increases with the increase of the excess voltage due to the higher sensitivity in SPAD causes the higher

probability of avalanches from both noise and photons. In the OWC application, the dark count in SPAD reduces the system performance by decreasing the SNR [70]. Acting as the detected photons from the background, the dark count in the absence of optical signal will disturb the judgments in receiver, thus increasing the possibility of error bits.

The afterpulsing is the secondary avalanche of the SPAD and contributes to the total DCR. The avalanche brings the free carriers that may be trapped by the energy traps [72]. The defects and impurities from the material of SPAD form the energy traps and the trapped carriers may be released at any time due to the lifetimes of traps are finite [73]. During the reset process, the avalanches that caused by the afterpulsing happens when the trapped carriers have not been fully released. As a parameter that is highly related with the lifetime of energy traps, the afterpulsing probability $P_{ap}(t)$ can be expressed as [74]:

$$P_{ap}(t) = \sum_{i} A_i e^{-\frac{t}{\tau_i}} \qquad 2\text{-}1$$

where the A_i is the constant of the i^{th} trap and the τ_i is the de-trap time of the i^{th} trap and t is the hold-off time of SPAD that depends on the SPAD front-end circuit. As the Figure 2-

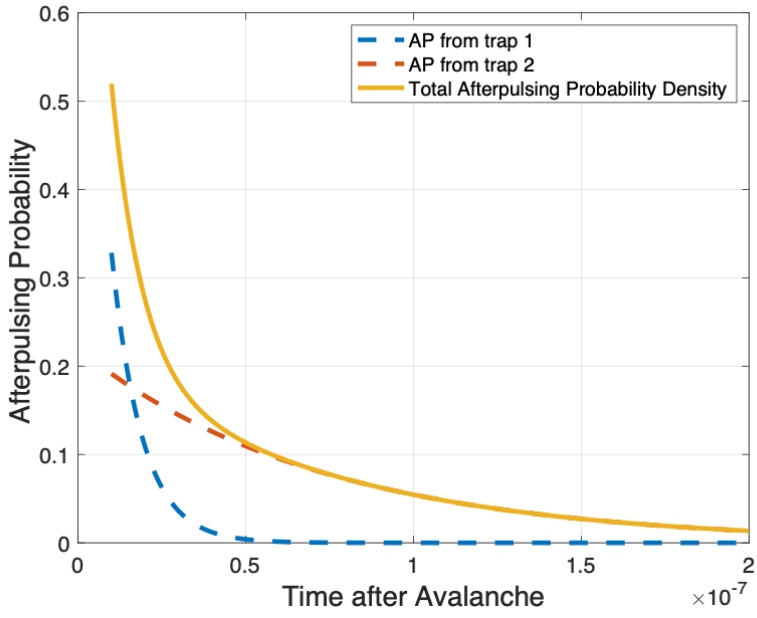

Figure 2-1: The simulations of the afterpulsing probability density with $A_1 = 0.99$, $\tau_1 = 9.06$ ns, $A_2 = 0.22$ and $\tau_2 = 71.63$ ns

1 shown, based on a previous measurement, the A_1 is 0.99, τ_1 is 9.06 ns, A_2 is 0.22 and τ_2 is 71.63 ns [75]. the total afterpulsing probability density is composed of all the traps releasing probabilities and decreases exponentially with the avalanche time.

The design of the SPAD structure plays a significant role in afterpulsing. For instance, the presence of defects or imperfections near the avalanche region can facilitate the trapping and releasing of charge carriers, leading to afterpulsing [73]. In addition, the choice of semiconductor material used to fabricate the SPAD has an impact on afterpulsing. Materials with lower defect densities and efficient carrier trapping mechanisms are preferred to reduce afterpulsing probabilities. For example, the silicon based SPADs are commonly used due to their well-established fabrication processes and relatively low afterpulsing rates. Guard rings are often used in SPAD structures to reduce edge breakdown effects and enhance the overall performance [76]. Properly designed guard rings can help suppress afterpulsing by reducing the chances of carriers reaching the regions prone to trapping.

The impact of afterpulsing on OWC applications is noteworthy. Afterpulsing can introduce timing uncertainties in the detection process, affecting the accuracy of time-of-flight measurements commonly used in OWC systems. The afterpulsing rate can influence distance estimation and positioning accuracy. Additionally, afterpulsing increases the likelihood of false positives, which can lead to higher BER and decreased communication reliability, especially in low-light or high-noise environments.

2.1.3. Dead Time

For each avalanching event, the SPAD needs time for quenching and resetting to complete the full detecting cycle, which is called the dead time [77]. During the dead time, the SPAD cannot respond to other incident photons. The physical properties of the avalanche region, such as its doping concentration and electric field profile, impact the dead time of SPADs. Higher doping concentrations and electric fields can lead to faster charge carrier multiplication and shorter dead times. As a vital parameter in SPAD, the dead time is inversely proportional to the count rate and the dead time processes are different with the SPADs front-end circuits. Effective quenching and rapid resetting mechanisms reduce the

time required for the SPAD to recover from its avalanche state and become ready for the next photon detection. SPADs with active quench and reset (AQR) circuit have a dead time composed of the quench, the hold-off interval, and the reset process [60]. The dead time of AQR SPAD is fixed and the hold-off interval occupies the main part of the total dead time. However, the dead time in passive quench and reset (PQR) circuit is composed of a passive quench and passive reset process and the main part in the dead time is the reset process. The incident photon during the reset process could be detected and trigger a new avalanche, thus extending the dead time of PQR SPAD [78].

When implement the SPAD into OWC applications, the dead time plays a vital role. For AQR SPAD receiver, high optical power brings more detected photons and benefits to OWC system, however, high optical power reduces the count rate in PQR SPAD and decreases the receiver performance [77]. The front-end circuit part will be induced in Section 2.2 and the count rate process in SPAD will be simulated in Section 4.1. In addition, as shown in the Equation 2-1, the afterpulsing rate is a function of the hold-off time. Therefore, in SPAD circuits, a very small dead time may not yield optimal performance in OWC applications. Only by adjusting the dead time to its optimal value can balance the photon count rate and afterpulsing.

2.1.4. Photon Detection Probability

The photon detection probability (PDP) is defined as the ratio of detected photons to the total incident photons and refers to the property of a SPAD that characterizes its probability in detecting incoming photons [79]. The incident photon may undergo losses due to absorption or scattering in the medium through which they propagate. These losses can reduce the number of photons reaching the SPAD. Several factors can influence the PDP, including the device structure, materials, and the operation mode in SPAD [79]. For a SPAD fabricated in standard CMOS technology, the incident photons may be reflected or absorbed by the different layers on the active area of SPAD, thus reducing the PDP of SPAD.

Higher PDP brings better photon detection ability in SPAD. If the noise in SPAD can be restricted under an acceptable level, PDP can be increased by increasing the active area or

rising the excess voltage on SPAD [80]. The OWC Application requires a balance between PDP and noises, thus the bias voltage on SPAD should be careful adjusted to ensure an optimal performance of SPAD receiver.

2.2. SPAD Front-end Circuits

2.2.1. Passive Quench and Reset Circuit

The PQR circuit is commonly used as the front-end circuit of the SPAD due to its simplification. As shown in the Figure 2-2 (a), a large resistor R_Q is connected with the anode of the SPAD and determines the quench and reset processes. Once a photon is detected, a self-sustaining avalanche is triggered in the SPAD, causing a large current pass

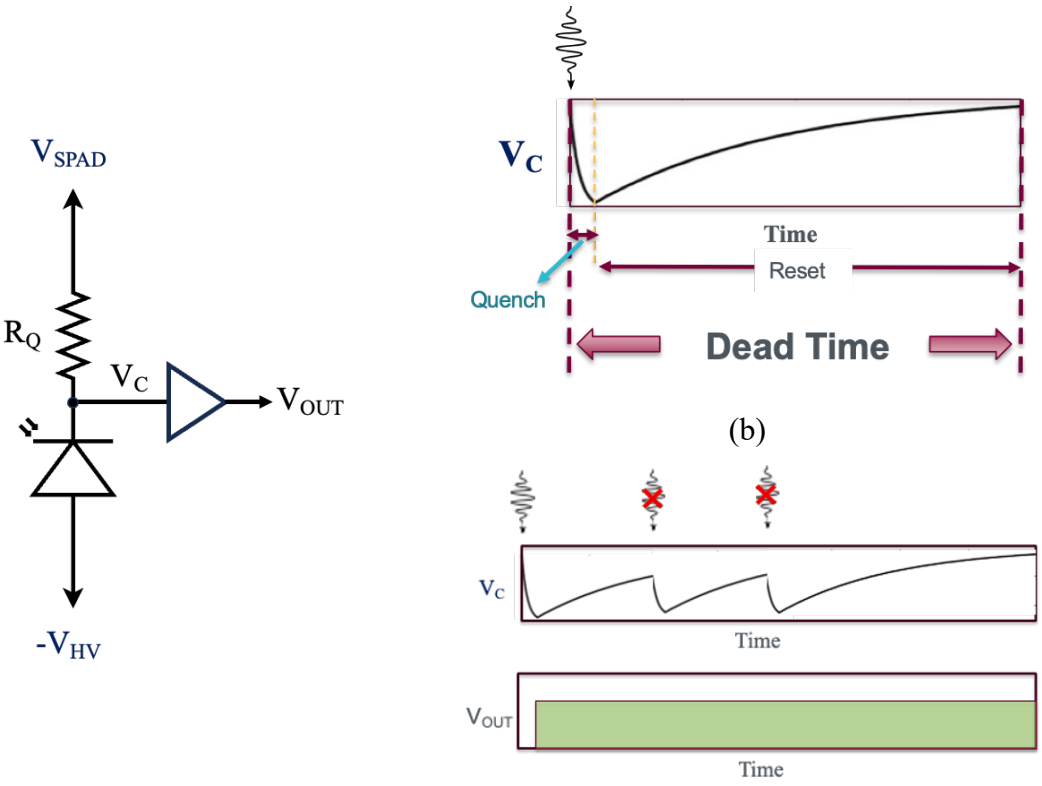

Figure 2-2: (a) The circuit schematic of passive quench and reset (PQR) SPAD circuit. (b) The SPAD cathode voltage variations of quench and reset processes of a PQR SPAD. (c) The SPAD cathode voltage variations if photons incident during the reset process of PQR SPAD.

through the SPAD and R_Q. A voltage drop across the SPAD due to the increased current leading a fast rise of the voltage on R_Q. The bias voltage on the SPAD keeps reduce until it is lower than the breakdown voltage and quenches the avalanche. The reset process of PQR SPAD is rely on the R_Q. The SPAD is recharged to prepare the next detection when the avalanche is ended, and the reset time is affected by the RC time constant of the SPAD.

The resistor R_Q must be large enough to ensure a fully quench in the SPAD, however, a long recharge time due to this large resistor causes a long dead time. Generally, a PQR SPAD has a dead time of hundreds of nanoseconds. As shown in the Figure 2-2 (c), the incident photons or free carriers during the reset process trigger new avalanches and extend the dead time. In the condition of high illuminance, the PQR SPAD suffers from a long dead time due to the high density of incident photons during the reset process. In the operation of PQR SPAD, there is no hold-off time for the trapped carriers to be released, thus, higher afterpulsing probability strongly restricts the performance of PQR SPAD receiver. As a receiver in OWC system, the PQR SPAD benefits from the simple structure and easy fabrication, however, the utilities of the PQR SPAD are not suitable for high optical power or low optical power conditions due to the long dead time and the high afterpulsing rate.

2.2.2. Active Quench and Reset Circuit

The quench and reset processes of SPAD can be actively operated by a AQR circuit. As the configuration shown in the Figure 2-3 (a), when a photon is detected, an avalanche is triggered causes a passive quench process due to the resistor R_Q. The active quench circuit senses the variance of SPAD cathode voltage and quench the SPAD actively. After the SPAD is fully quenched, a hold-off time keeps the bias voltage of SPAD lower than the breakdown voltage to release the trapped carriers. The active reset circuit connects the cathode of SPAD with the power supply (V_{SPAD}) to charge the SPAD after the hold-off time.

The quench circuit and the reset circuit achieve fast quench and reset processes in AQR SPAD. The cathode of SPAD connects with the power supply and the ground straightly

through the AQR circuits. By implementing the AQR circuit, very low dead time is available for the high counting rate applications. In recent years, the dead time of AQR SPAD is as low as a few nanoseconds [81]. As the active quench and reset process is very fast, the dead time of the AQR SPAD depends on the hold-off time. Short hold-off time may increase the afterpulsing probability and long hold-off time reduces the count rate ability of SPAD. Different from the PQR SPAD, the dead time is constant and the incident photons during the hold-off time cannot extend the dead time since the bias voltage is lower than the breakdown voltage during the hold-off time. In the application of OWC, the AQR SPAD receiver benefits from the low and fixed dead time, and low afterpulsing probability. Compared with PQR SPAD, the AQR SPAD receiver has better performance, and it is available to more communication conditions.

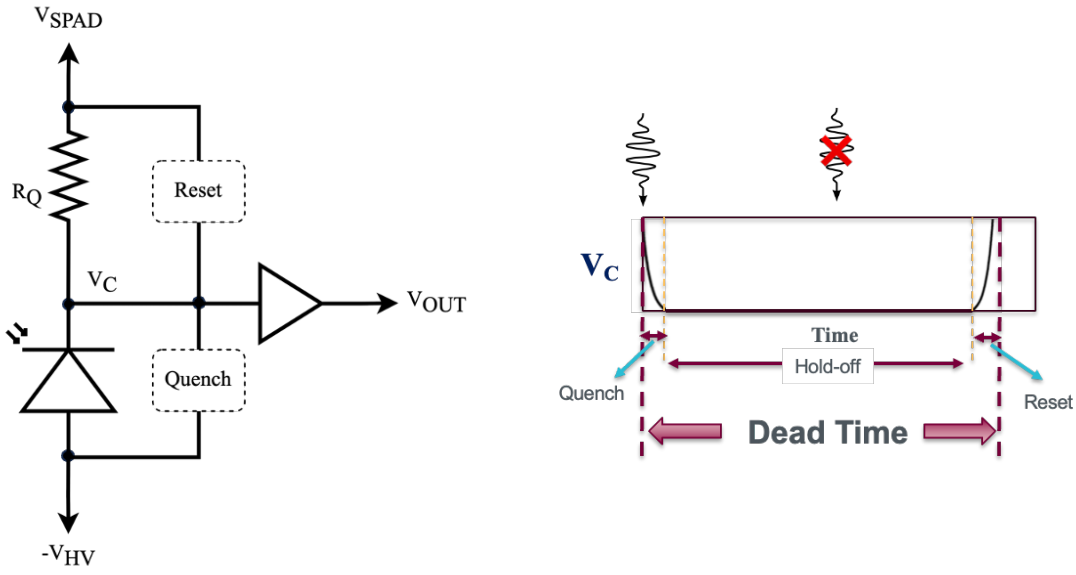

(a) (b)

Figure 2-3: (a)The circuit schematic of the active quench and reset (AQR)SPAD circuit. (b) The cathode voltage of the quench, hold-off and reset processes in AQR SPAD.

2.2.3. Time-gated SPAD Circuit

In some applications, SPAD only needs to be active during the detection window and keeps in inactive state during other time, the time-gated (TG) SPAD is designed for these

conditions [82]. The timing circuit in SPAD introduces a gating signal that determines when the SPAD is sensitive to incoming photons. The TG mode of SPAD operation can be achieved through targeted variations in the biasing voltage, wherein voltage levels are selectively adjusted to exceed or fall below the SPAD breakdown voltage within designated time intervals. As shown in Figure 2-4 (a), the added time-gated circuit controls the reset and quench circuits by generating the gate-on and gate-off signals. During the gate-off interval, the SPAD keeps in hold-off state and no photon can be detected. The gate-on signal actives the reset circuit for detection, the photon detection operation is as normal as an AQR SPAD (Figure 2-4 (b)).

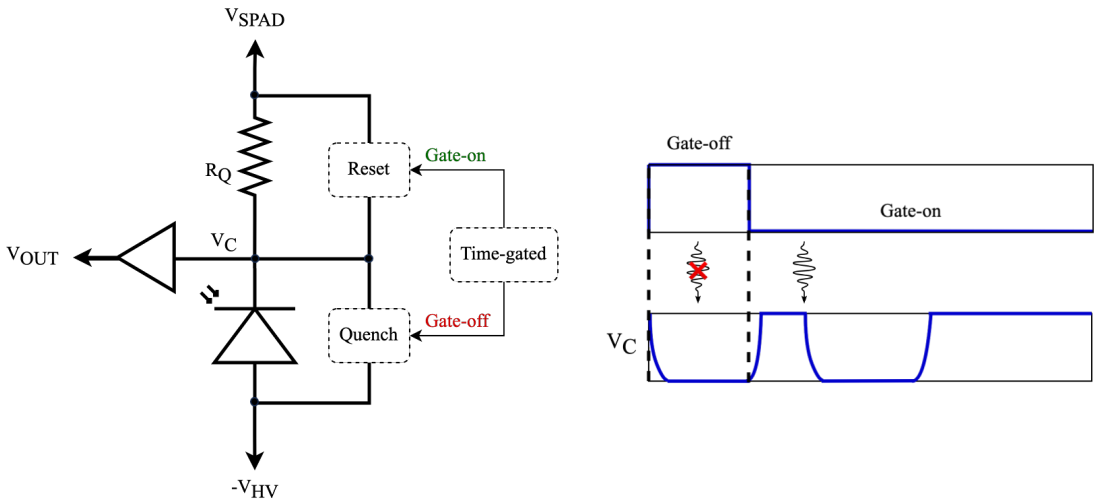

Figure 2-4: (a) The circuit schematic of time-gated (TG) SPAD circuit. (b) The variations of SPAD cathode voltage in TG SPAD circuit.

The TG SPAD is an operation mode for reducing the DCR and afterpulsing [83]. The SPAD is only responsive in gate-on interval to filter the noises and concentrate the photon counts. The TG SPAD has been implemented into the applications in imaging and spectroscopy for more accurate photon detection. As a disadvantage, the photon counting rate of TG SPAD is lower than the free-running SPAD due to the gate-off. This feature makes the TG SPAD may perform worse in the applications of continues detection or random detection. In the OWC system, the background noise is restricted by the TG SPAD,

which makes the TG SPAD perform better in the high background noise communication. However, compared with the FR SPAD receiver, the reduced counting rate in TG SPAD decreases its performance.

2.2.4. Clock-driven SPAD Circuit

As a special time-gated SPAD, A SPAD pixel can be reset or muted periodically by a clock, which is called a clock-driven (CD) SPAD. Figure 2-5 (a) shows the configuration of the CD SPAD that the reset circuit is operated periodically by the clock driven pulse. The hold-off process is stopped and the SPAD is reset forcibly when the driven pulse is triggered (Figure 2-5 (b)). Different from the traditional AQR SPAD, the hold-off time is not fixed but depends on the clock in CD SPAD. In the CD SPAD circuit, the SPAD can be reset by both the active reset circuit and the clock-driven pulse. With the support of CD mode, SPAD pixels can respond to periodic photon events and keep inactive for noise photons. In the previous publications, the CD mode SPAD was used in image sensor and image scanning microscopy applications, showing higher counting efficiency and higher linearity [84], [85].

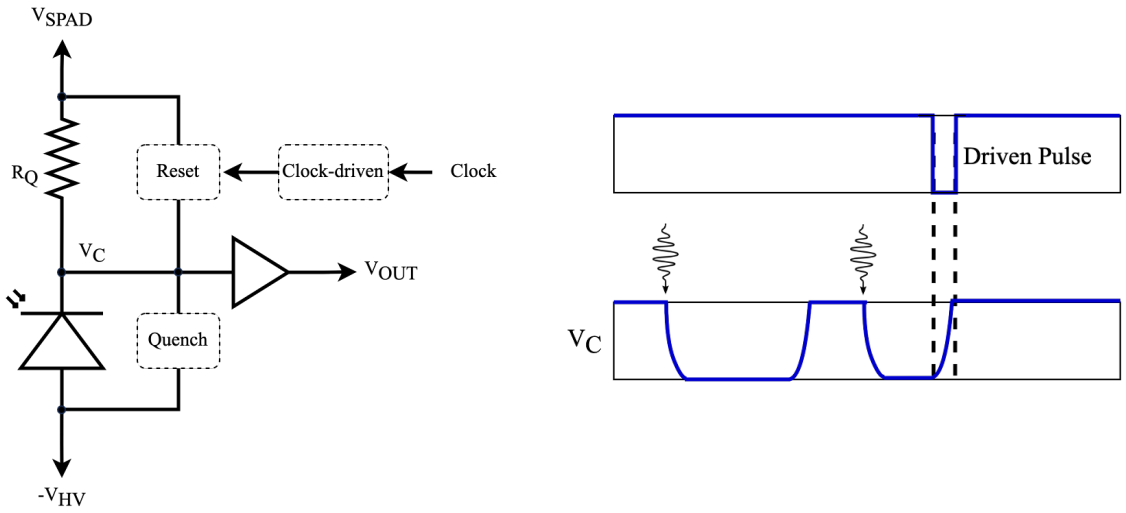

Figure 2-5: (a) The circuit schematic of clock-driven (CD) SPAD circuit. (b) The variations of the SPAD cathode voltage in CD SPAD circuit

The CD SPAD is responsive in the specific time window because of the forcible reset process, and this function causes the average dead time of CD SPAD is shorter than the FR SPAD. Higher counting rate in the CD SPAD increases the performance in low illuminant applications, on the other hand, CD SPAD has a potential of more afterpulsing due to the lower average hold-off time. By synchronizing the clock signal with the desired operation timing, a clock-driven SPAD can be effectively used in various applications that require precise timing, such as time-resolved measurements, fluorescence lifetime imaging, and photon correlation experiments. The clock signal allows for precise control over the detection window, enabling accurate measurement of photon arrival times.

2.3. Conclusion

In this chapter, the key performances of SPAD, that related to the SPAD-based OWC are introduced. Two classic SPAD front-end circuits and two time-controlled SPAD front-end circuits are presented. In OWC applications, SPADs are anticipated to possess high photon detection probability, low dead time, and a minimal dark count rate. However, there exists trade-offs among these factors. For SPAD circuits, the excess voltage and dead time can be adjusted, playing a pivotal role in controlling the response performances. The excess voltage determines the photon detection probability (PDP) of the SPAD, however, higher excess voltage brings higher dark count rate. Low dead time leads high photon count rate but also increases the afterpulsing rate of SPAD. Therefore, it is important to identify the optimal values within these relationships, which are not fixed but continuously adapt to the variations in application scenarios. For instance, in applications with high optical intensity, a high excess voltage can detrimentally affect the SPAD receiver performance. This arises due to the decreased demand for SPAD sensitivity by the communication system in the presence of high optical intensity, and the resultant high dark count rate from the elevated excess voltage can reduce the final performance. Similarly, in low optical intensity applications, properly increasing the excess voltage can enhance SPAD sensitivity, consequently boosting performance. In high data rate applications, a high dead time can impede photon count rate, making a lower dead time more favourable for improved

performance. Conversely, in low-data-rate scenarios, the situation is reversed as the high afterpulsing rate due to low dead time can have a more adverse impact on system performance.

The performance of the SPAD receiIer is significantly determined by the SPAD circuit. Essentially, the passive quench and reset (PQR) circuit only boasts the advantage of simplicity in its structure. Compared to other SPAD circuits mentioned in this chapter, the PQR circuit exhibits a longer and less predictable dead time. Particularly, the dead time of the PQR circuit increases with the incidence of photons, which can adversely affect SPAD applications, particularly those reliant on photon-counting detection like OWC applications. Furthermore, the extended reset time contributes to a higher afterpulsing rate, further compromising the performance of the SPAD receiver. Apart from the PQR circuit, the other three circuit configurations each come with their own merits and limitations, along with specific application scenarios. These will be analysed in Chapters 3 and 4.

Chapter 3
Design of CMOS SPAD Receiver

3.1. The Basic Front-end Circuit

In this chapter, a SPAD front-end circuit is designed in a 65 nm standard CMOS technology, the CD mode and TG mode SPAD circuits are derived from it. These circuits are then used to design CD mode and TG mode receivers for low data rate OWC and high data rate OWC applications, respectively, utilizing two different signal generation circuits. Post-layout transition simulations demonstrate that implementing these two modes (CD mode and TG mode) can significantly reduce the block time in the SPAD receiver compared to the FR mode.

3.1.1. Operation Principle

The schematic of the basic front-end circuit is shown in Figure 3-1. and two post-layout simulation results under two control voltages (V_{CON}) are shown in Figure 3-2. The SPAD model in the simulation comes from our previous work [60]. Initially, the cathode voltage of the SPAD V_C is at 1 V and the anode is connected to $-V_{HV}$ to bias the SPAD above the breakdown. M4 and M5 form an inverter to keep node A at low voltage, causing M3 to be off. The 0.8 ns fixed delay element τ, the second inverter and the controlled delay element are connected in series to keep node B and node C in high voltage. Node D is at 1 V due to the OR gate. Therefore, M2 turns on and M1 was off. In this initial condition, the SPAD is biased above the breakdown voltage, and it is in the photon detecting mode.

When an incident photon is detected, self-sustaining avalanche initiates, M3 in the off-state acts as a large resistance to generate a passive quench process and reduces the voltage of V_C. The inverter made by M4 and M5 senses the declining V_C and reverses the node A to a high voltage level, hence turning M3 on to start an active quench process. The bias

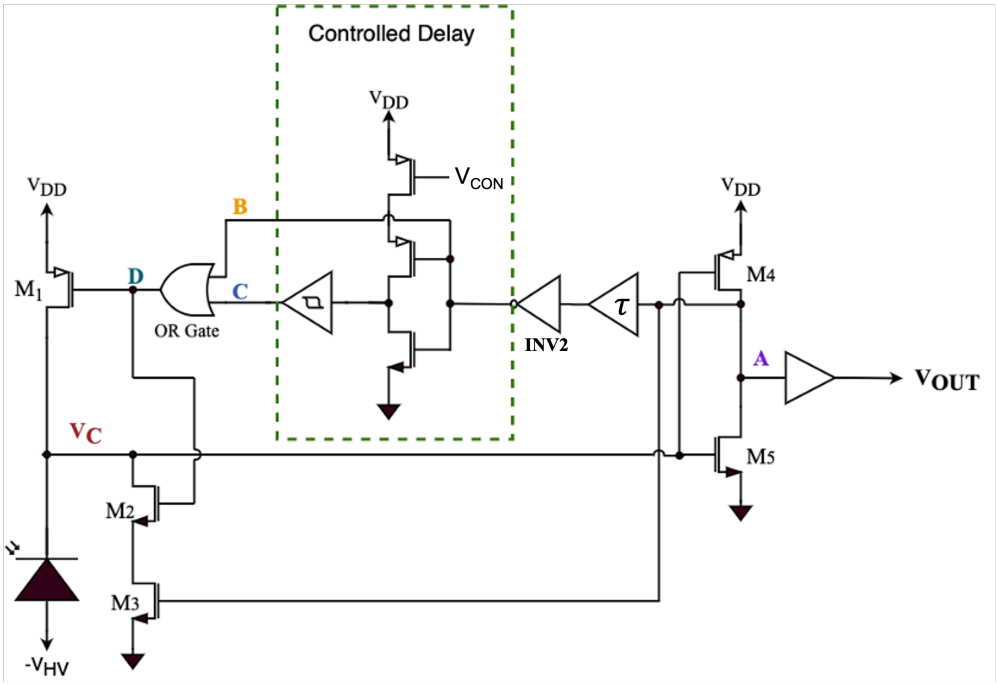

Figure 3-1: The schematic of the basic SPAD front-end circuit

voltage will become below the breakdown voltage when V_C connects to ground through M2 and M3, starting the hold-off process. The rising voltage of node A will be delayed by τ and reversed by the second inverter INV2, causing a change on node B. The falling edge of the voltage in node B is delayed by the controlled delay element and the node C is the output of the delay element. At the moment when both nodes B and C turn to low voltage level, the OR gate will change node D to low voltage level and turn M2 off and M1 on, so the hold-off process will be terminated and the SPAD will be recharged back to its initial state through M1. The inverter made by M4 and M5 senses the high voltage of V_C and then changes the node A to a low voltage, which results in node B turns to high voltage after the time τ and terminates the reset process. Then, the SPAD pixel is ready to detect the next photon. The time τ here is designed to be 0.8 ns, thus having enough time for the reset process and causes the hold-off process. One buffer is connected with node A to generate the output pulse V_{OUT}. The controlled delay element consists of a voltage-controlled inverter and a Schmitt trigger, which only delays the falling edge of node B. This feature ensures that the hold-off time can only be delayed by the controlled delay element and has

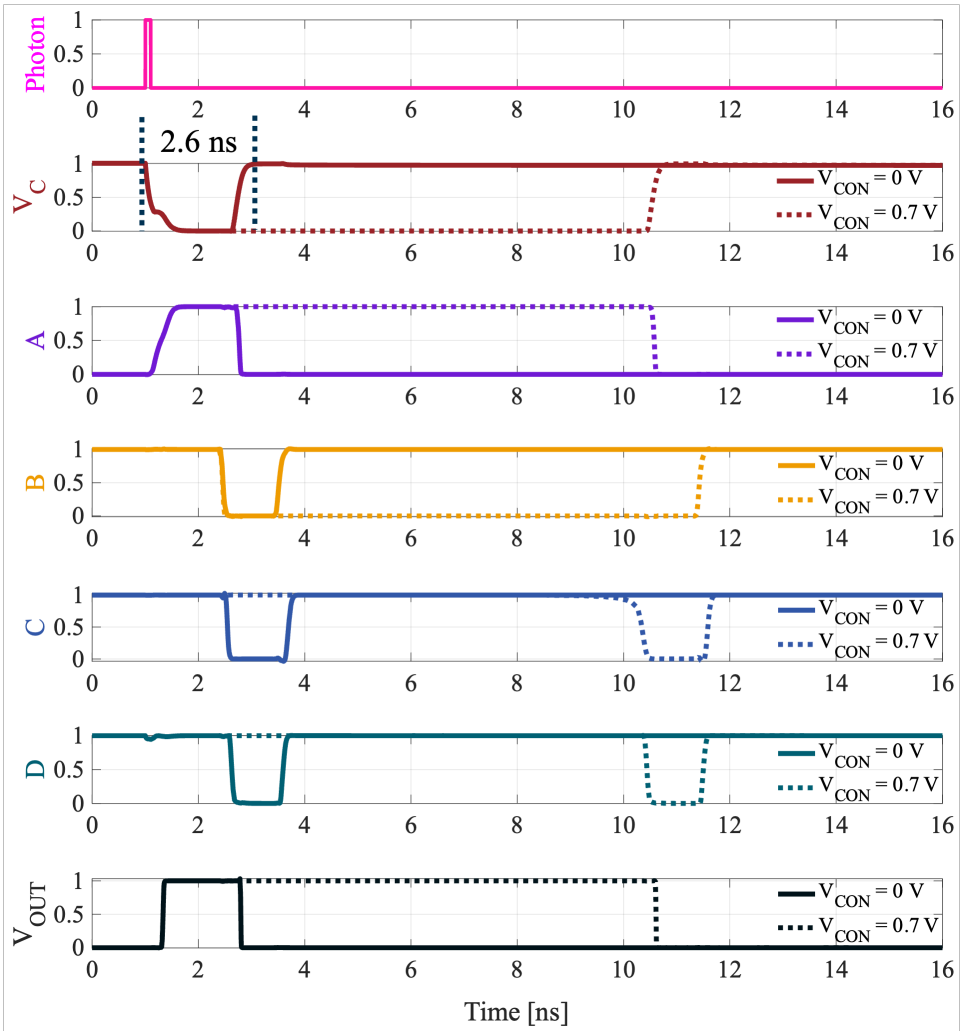

Figure 3-2: The post-layout transient simulation results for the SPAD circuit

no effect on other processes. The delay duration of the controlled delay element increases with the rise of V_{CON}.

As shown in Figure 3-2, the dead time can be observed by the V_C variance, and the shortest achievable dead time of the basic front-end circuit is 2.6 ns when the V_{CON} is 0 V. For comparison, the dead time is 10 ns when V_{CON} is set to be 0.7 V. The quench and the reset times are 0.7 ns and 0.8 ns, respectively, in both V_{CON} conditions. Hold-off time is 1.1 ns when V_{CON} is 0 V, and increases to 8.5 ns when V_{CON} is set to be 0.7 V.

For the OWC application, a short dead time leads to a high photon detection ability, thus increasing performance of a SPAD-based OWC receiver [77]. In contrast, a long dead

time will cause the ISI effect and disturb the photon counting process in an OWC system [86]. In this design, the shortest achievable dead time is 2.6 ns, which is much shorter than some of recently reported values (8-30 ns) [87]–[89]. To achieve a short dead time, we need to reduce the hold-off time. However, too low hold-off time may cause a higher afterpulsing probability [90], [91], which reduces performance of OWC systems. The controlled delay element in our design can be used to adjust the hold-off time to an optimal value to balance the noise effect and photon detection ability.

3.1.2. Hold-off Time Control Circuit

The hold-off time control circuit is a Schmitt trigger with a voltage-controlled inverter. As shown in the Figure 3-3, the PMOS connects with V_{CON} determines the delay time of the inverter and the cascaded Schmitt inverter recovers the delayed signal [92]. With the increase of the V_{CON}, the channel of this PMOS with the gate voltage V_{CON} gets narrow gradually, thus reducing the inverter speed. The sub-graphs A and B in Figure 3-4

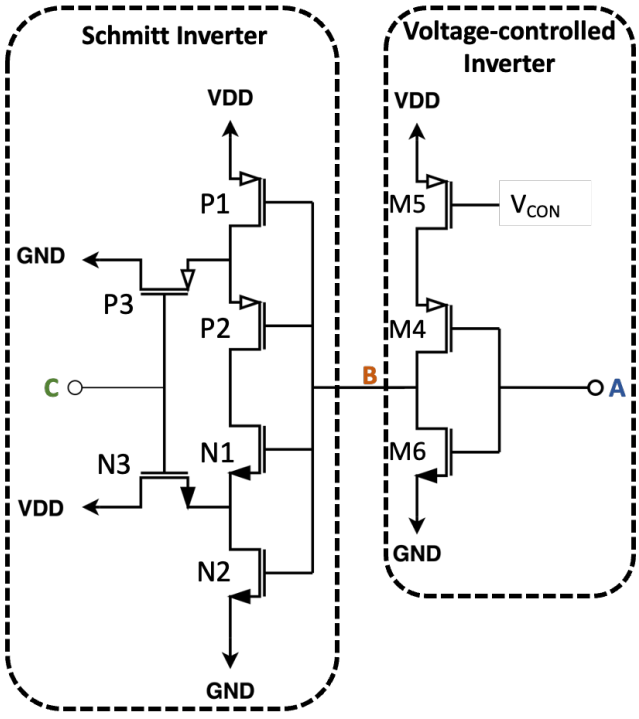

Figure 3-3: The circuit schematic of the Schmitt trigger with voltage-controlled inverter.

demonstrated this process, as the input A is inverted, and the transition time of the fall edge of the input A is controlled by the V_{CON}. The drain voltage of M4 (B) is charged through M5, thus the low to high transition time of B is delayed by the V_{CON}, and the delay time of this inverter equals to the rise time of B. The inverter speed of the rise edge from A is determined by the M6, the high voltage from A switches on the M6 and the rise edge of I is invIrted immediately and not effected by the V_{CON}. To recover the signal, a Schmitt inverter is cascaded. As an inverter acts like a logic gate, the Schmitt inverter has only two statuses of '1' and '0', a threshold is set by the transistors space ratios [93], and the equations are shown as:

$$V^+ = \frac{V_{TN1} + \sqrt{\frac{\beta_{N3}}{\beta_{N1}}} V_{DD}}{1 + \sqrt{\frac{\beta_{N3}}{\beta_{N1}}}} \tag{3-1}$$

$$V^- = \frac{\sqrt{\frac{\beta_{P1}}{\beta_{P3}}} (V_{DD} - V_{TP1})}{1 + \sqrt{\frac{\beta_{P1}}{\beta_{P3}}}} \tag{3-2}$$

where the V_{TN1} and V_{TP1} are the threshold voltages of N1 and P1, the β represents the width and length ratio of transistor. In this design, the threshold V^+ is set to around 600 mV,

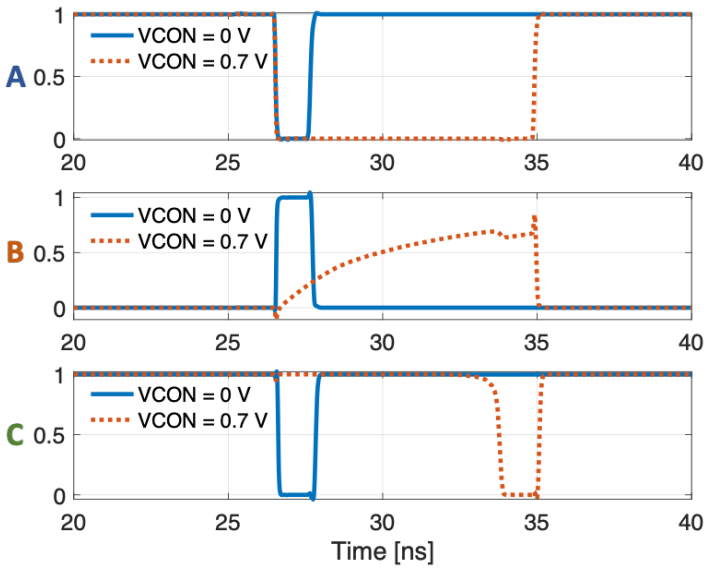

Figure 3-4: The post-layout simulation results of the voltage-controlled hold-off time process.

and as the low to high transition of B is delayed, 7 ns is needed for this transition from 0 V to 600 mV. The circuit that is shown in the Figure 3-3 works for the adjustable hold-off time, the control voltage adjusts the low to high transition time and leading a delay to trigger reverse from the Schmitt inverter. The Figure 3-5 demonstrated the relationship between the control voltage V_{CON} and the dead time.

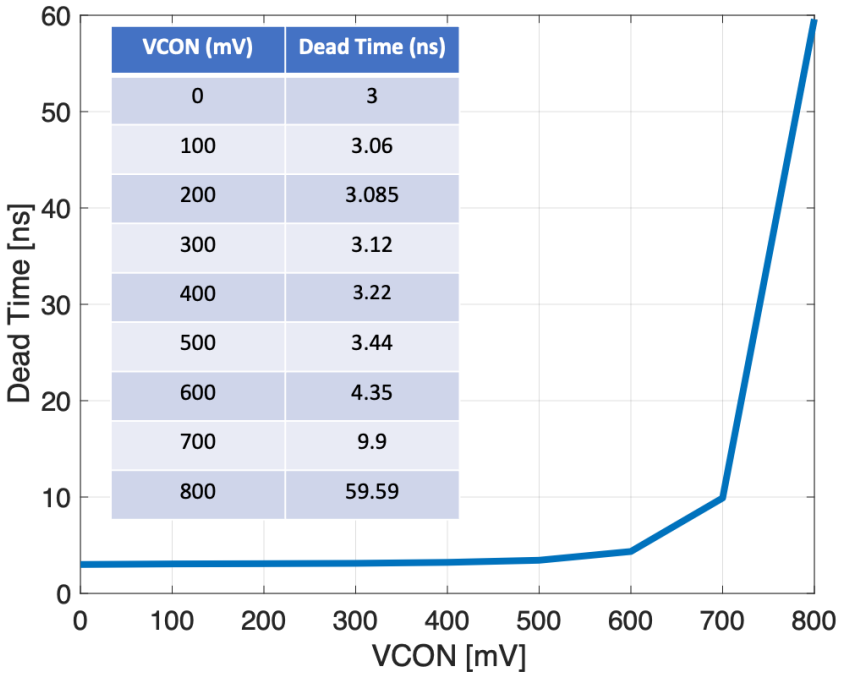

Figure 3-5: The post-layout simulation results of the relationship between the control voltage V_{CON} and the dead time.

3.2. The Clock-driven Mode SPAD Circuit

3.2.1. CD Signal Generation Circuit

SPAD pixels can be reset periodically by a clock, which is called a CD SPAD. Single photon counters exhibit higher counting efficiency and higher linearity in the CD operation mode [94], [95]. In the CD mode SPAD receiver, two reset mechanisms are designed to reset the SPAD by both the CD signal and the AQR circuit. Figure 3-6 shows the schematic of the CD signal generation circuit, the CD signal generation circuit consists of one AND

gate, one inverter and one fixed delay element which has a same delay time with the fixed delay element τ in the basic front-end circuit as shown in Figure 3-1. The post-layout transient simulation result is shown in Figure 3-7, the data signal is delayed by A and inverted by B, both the data signal and B connect into the NAND gate, generating the CD signal. The circuit input (data signal) is designed to have a same frequency of the data rate and can be implemented through the bit synchronization technology [96]. The CD signal can be described as a periodic pulse generated at the beginning (the rising edge of the data signal) of every bit interval as shown in Figure 3-7, the length of the CD signal pulse is determined by the fixed delay element τ to ensure enough reset time for the SPAD pixel.

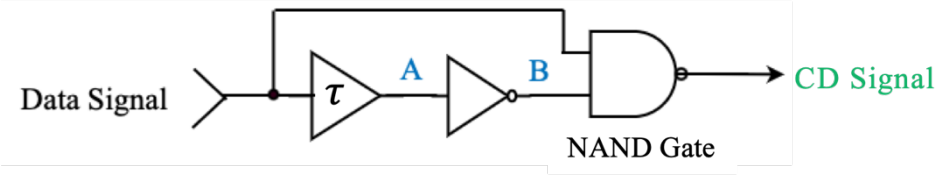

Figure 3-6: Schematic of the clock-driven (CD) signal generation circuit.

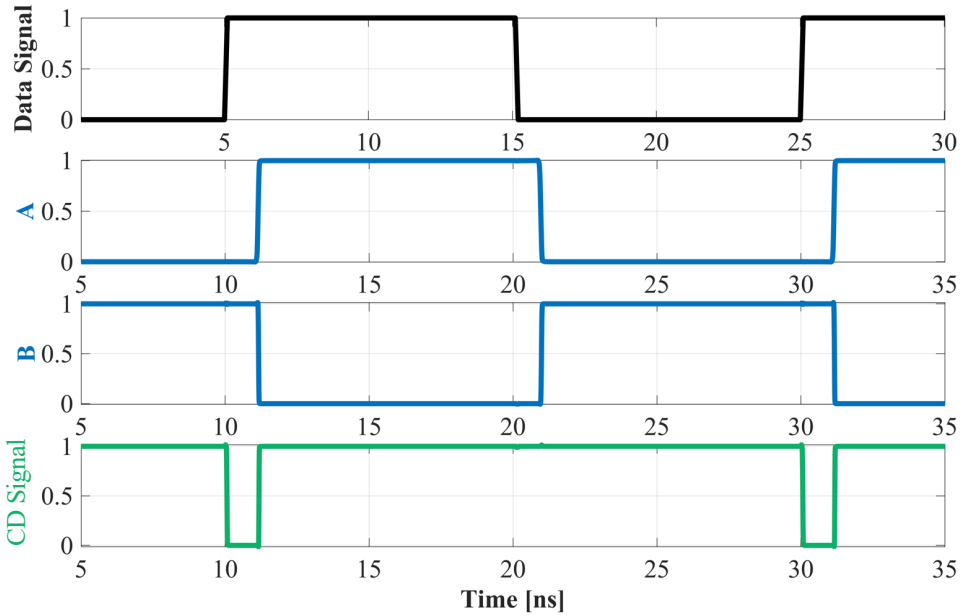

Figure 3-7: The post-layout simulation results of the clock-driven (CD) signal generation circuit

3.2.2. CD SPAD Operation Circuit

In the Figure 3-8, an added transistor M_{S1} connects with M1 in parallel and M_{S2} connects with M2 and M3 in series. As a result, the low voltage level of the CD signal turns M_{S2} off and M_{S1} on, which disconnects the cathode to the ground while connecting the cathode to VDD. That is the CD signal can disable the hold-off process and recharge the SPAD back to initiate, the reset process at the beginning of every bit interval.

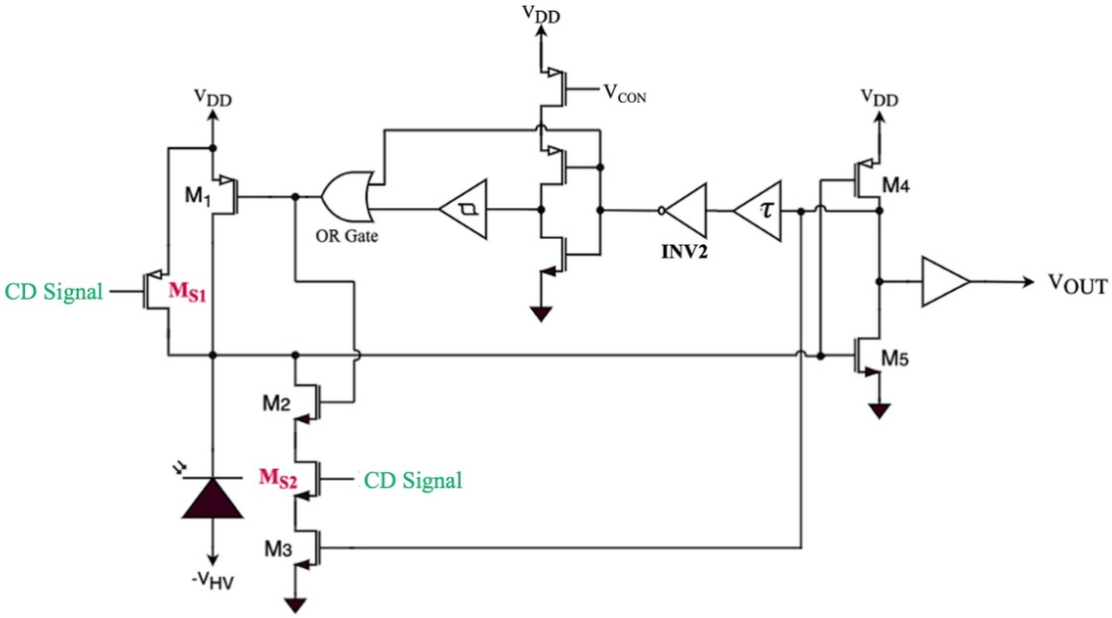

Figure 3-8: Schematic of the front-end circuit in the clock-driven (CD) mode.

The post-layout transient simulation results of the CD-mode SPAD pixel are shown in Figure 3-9, the solid line in the fourth sub graph (iv) is the waveform of V_C under the CD mode, and the dotted line is the waveform of the V_C in the FR mode. V_{CON} is set to 0.7 V to adjust the dead time of the SPAD pixel to be 10 ns to balance the performance of DCR and photon counting ability. The bit interval is set to 20 ns. In CD mode, the dead time that caused by the detected photon or dark carrier in one bit interval will not affect the photon counting ability of the SPAD in the next consecutive bit interval due to the reset process at the beginning of every bit interval. In this mode, the photon counting process in every bit interval is independent, and the dead time is not fixed, but determined by the moment when photons arrive. In the Figure 3-9, FR mode has a fixed dead time. However, in the CD

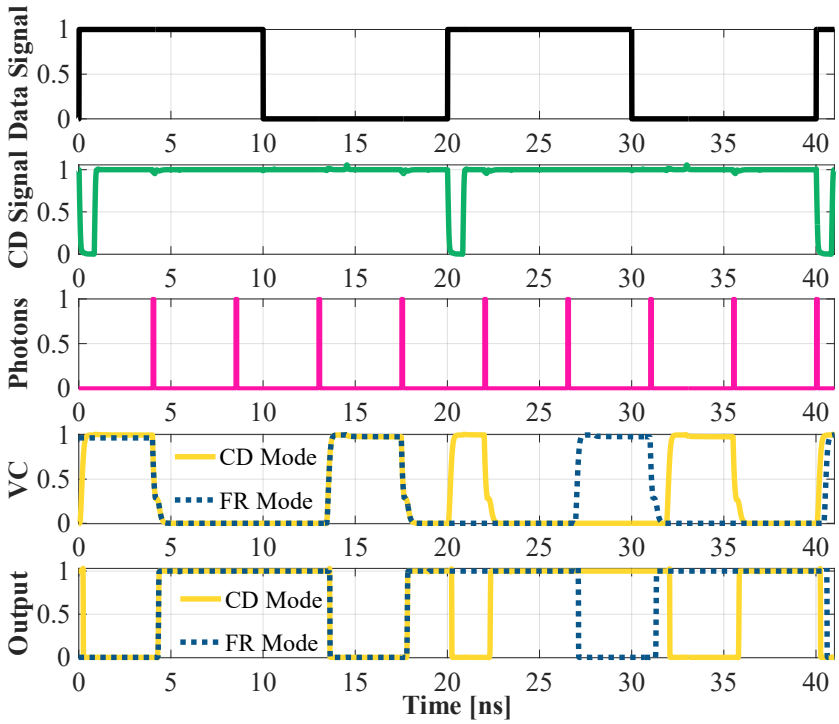

Figure 3-9: Post-layout transient simulation results for the signal generation circuit, the clock-driven (CD) mode front-end SPAD circuit and the free-running (FR) mode front-end circuit.

mode, the dead time caused by the first detected photon is 10 ns and the next dead time in CD mode is only 2.1 ns. As a result, the SPAD pixels have a lower average dead time in the CD mode. It is worth emphasizing that the dead time in CD mode cannot be infinitely short. Although the hold-off time can be set to 0, the quench and reset times (approximately 1.5 ns) need to be preserved to ensure the continuous detection capability of the SPAD. Compared to the FR mode, a SPAD receiver in the CD mode has a higher photon counting ability. For example, a SPAD under the CD mode counted 4 photons during two bits, but FR mode counted only 3 photons under the same photon incident condition as shown in Figure 3-9. Another advantage of using the CD mode is the reduction of ISI effect since no dead time can extend to the next bit interval. As shown in the Figure 3-9, the dead time caused by the incident photon i^{n} the 1st bit extends to the 2nd bit, thus leading to an ISI effect. In contrast, the CD mode resets the SPAD pixels at the beginning of bit interval, thus significantly reducing the ISI effect. This feature improves the performance of SPAD receiver significantly in OWC system. It is worth noting that, in a high data rate condition,

the afterpulsing rate may increase because of the CD-mode operation resets the SPAD pixels at a high frequency, leading to the average hold-off time being low in the high data rate condition. Since a short hold-off time can strongly increase the afterpulsing rate.

3.3. The Time-gated Mode SPAD Circuit

3.3.1. TG Signal Generation Circuit

The time-gated mode SPAD is designed for the high data rate communications, where the bit interval is shorter than the dead time. In this condition, several bit intervals may be blocked by one dead time, thus causing severe impact on photon counting. Figure 3-10

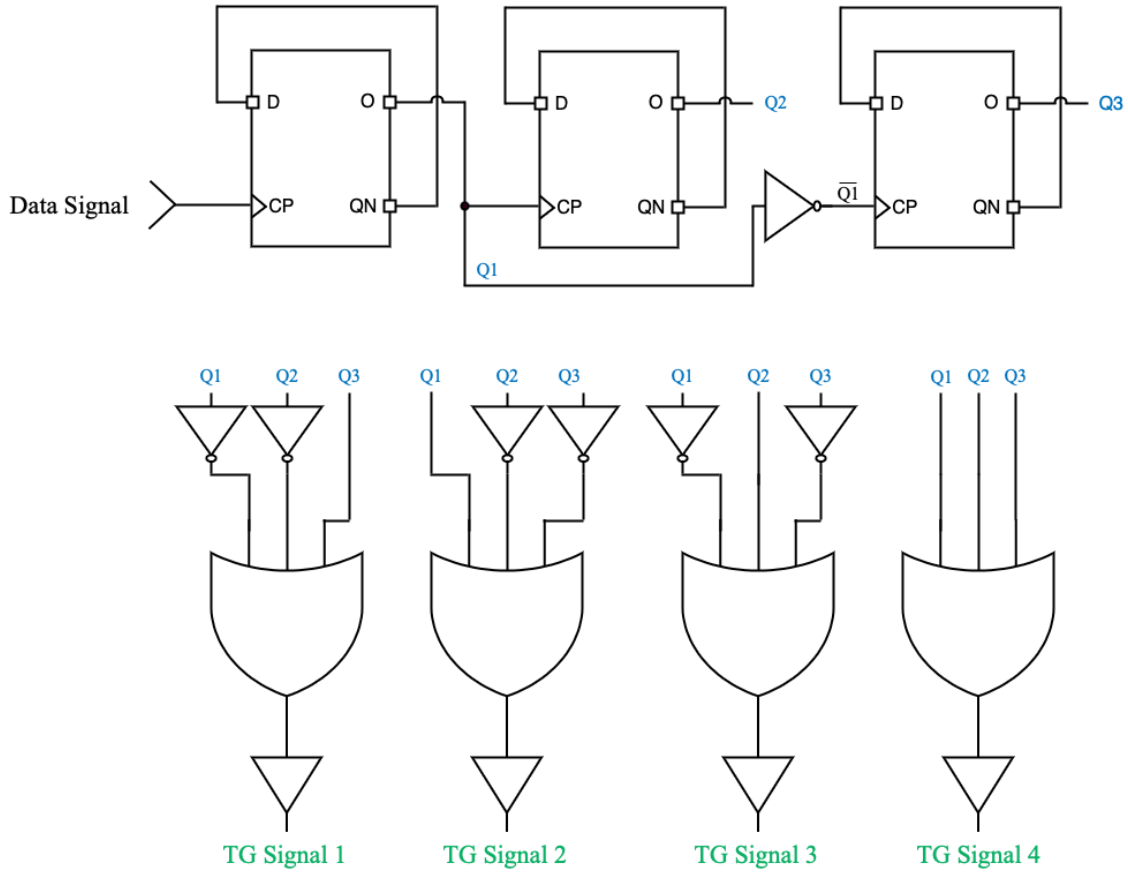

Figure 3-10: The schematic of the time-gated (TG) generation circuit.

shows the schematics of the TG signal generation circuit. As shown in Figure 3-10, the TG signal generation circuit is made of three D flip-flops, four 3-inputs OR gates, several

inverters and buffers. The outputs of three D flip-flops, Q1, Q2 and Q3, consist of four logical patterns corresponding to four signal outputs through the combination of high and low voltages. The TG signal generation circuit generates four TG signals and divides a full SPAD array into four sub-SPAD arrays. In our design, the full SPAD array is set to be 16 SPAD pixels and every sub-SPAD array has 4 SPAD pixels.

In this TG mode, 4 TG signals continuously operate four sub-SPAD arrays and one TG signal only operates one specific sub-SPAD array. Figure 3-11 (a) shows the 4 TG signals generated in sequence and form a cycle, the length of gate-on intervals from TG signals

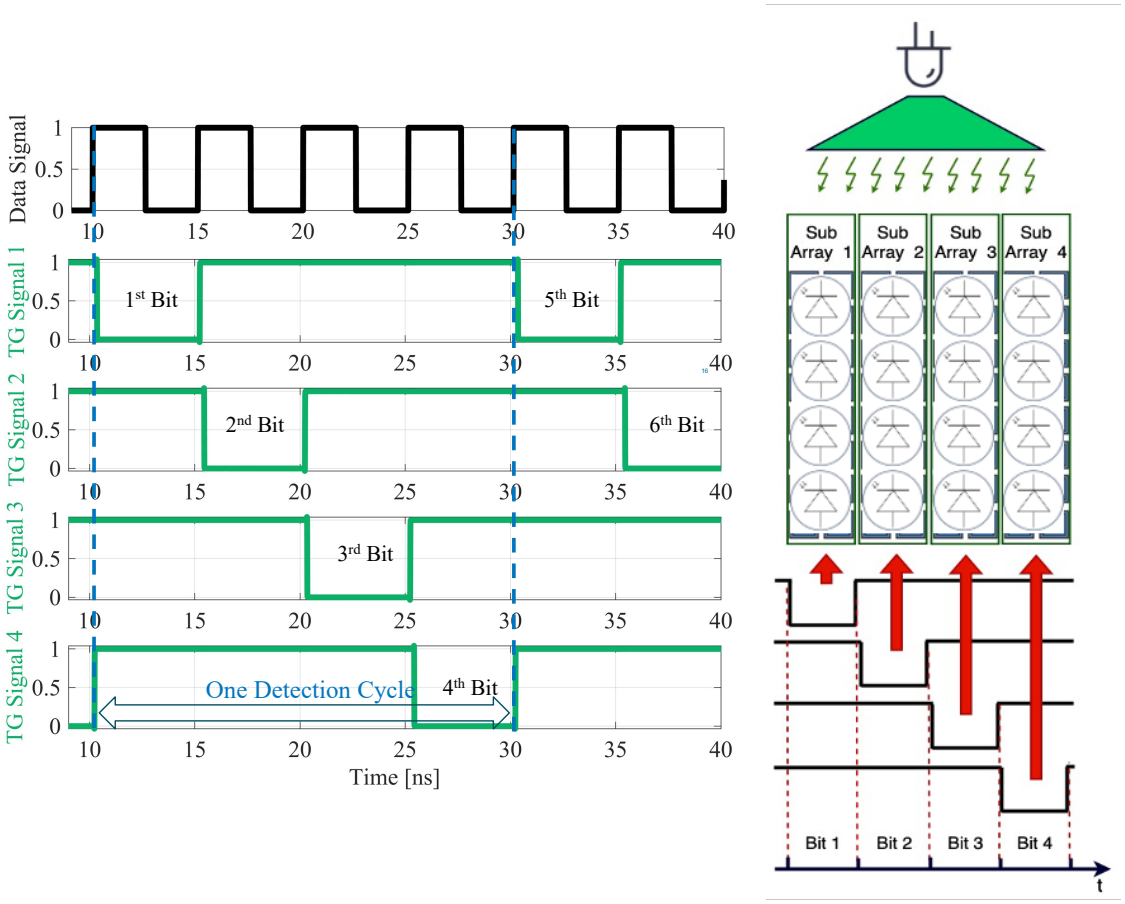

(a) (b)

Figure 3-11: (a) The Post-layout transient simulation results for the time-gated (TG) signal generation circuit. (b) The diagram of the TG mode operation principle/

(low voltage level) is as same as the bit interval. As shown in the Figure 3-11 (b), One detection cycle contains four sub-SPAD arrays being enabled cyclically by four TG signals.

Therefore, one sub-SPAD array only detect one bit in one detection cycle and 4 bits can be detected in one detection cycle in total. In the optical communication system based on photon counting, the ability of photon detection and the time range when the photon is detected are very important. When the dead time covers several consecutive bit intervals, the information in these bit intervals will be missed. Therefore, we propose a time-gated circuit to reduce the interference of dead time on signal photon detection.

3.3.2. TG SPAD Operation Circuit

The schematic of the TG mode front-end circuit is shown in Figure 3-12, in contrast to the CD mode, M_{S1} connects with M1 in series and M_{S2} connects with M2 and M3 in parallel. The SPAD pixels stay in hold-off during the high voltage of TG signal since M_{S1} turns off and M_{S2} turns on. Under this condition, the cathode of SPAD connects to ground through M_{S2}. The low voltage of TG signal enables the SPAD pixels to the active detection condition because the M_{S2} is turned off and the M_{S1} is turned on thus recharging the cathode

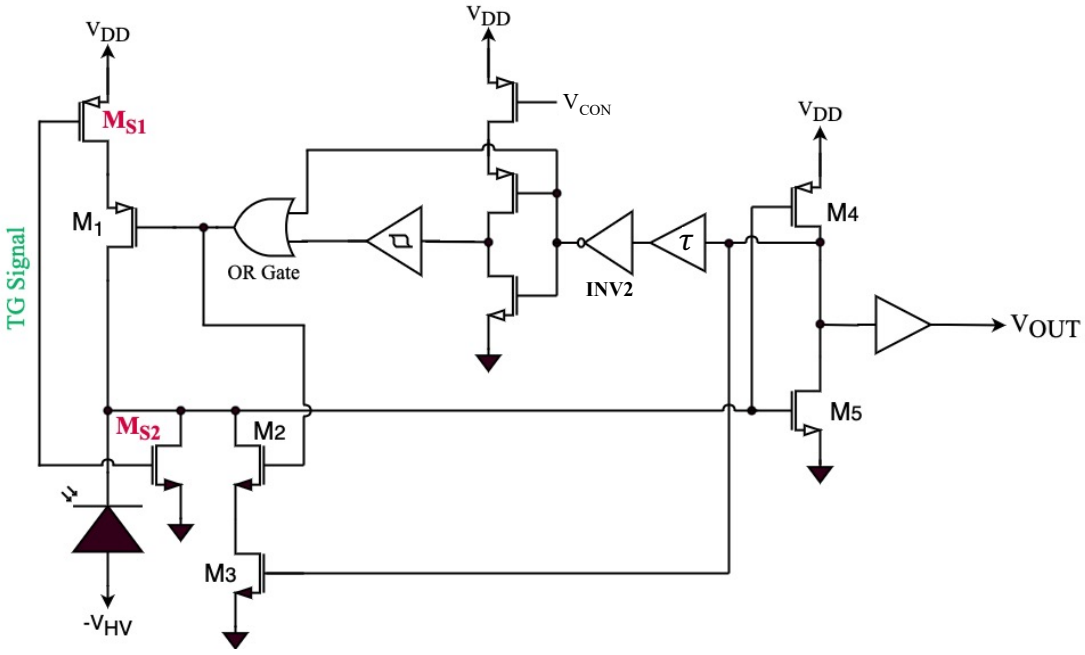

Figure 3-12: Schematic of the front-end circuit in the time-gated (TG) mode.

of the SPAD. As a result, the TG signal enables every sub-SPAD array to be turned on by the gate-on signal and turned off by the gate-off signal.

In the TG mode, every sub-SPAD array is independent and there is always a sub-SPAD array at the gate-on interval due to the cyclic enablement function. When the dead time is less than 4 times of the bit interval, there is no ISI effect in the TG mode because the dead time in one sub-SPAD array cannot cause any effect on other sub-SPAD arrays. However, if the dead time is above 4 times of the bit duration, the dead time in one sub-SPAD array may extend to the next detection cycle and cause ISI effect in this sub-SPAD array.

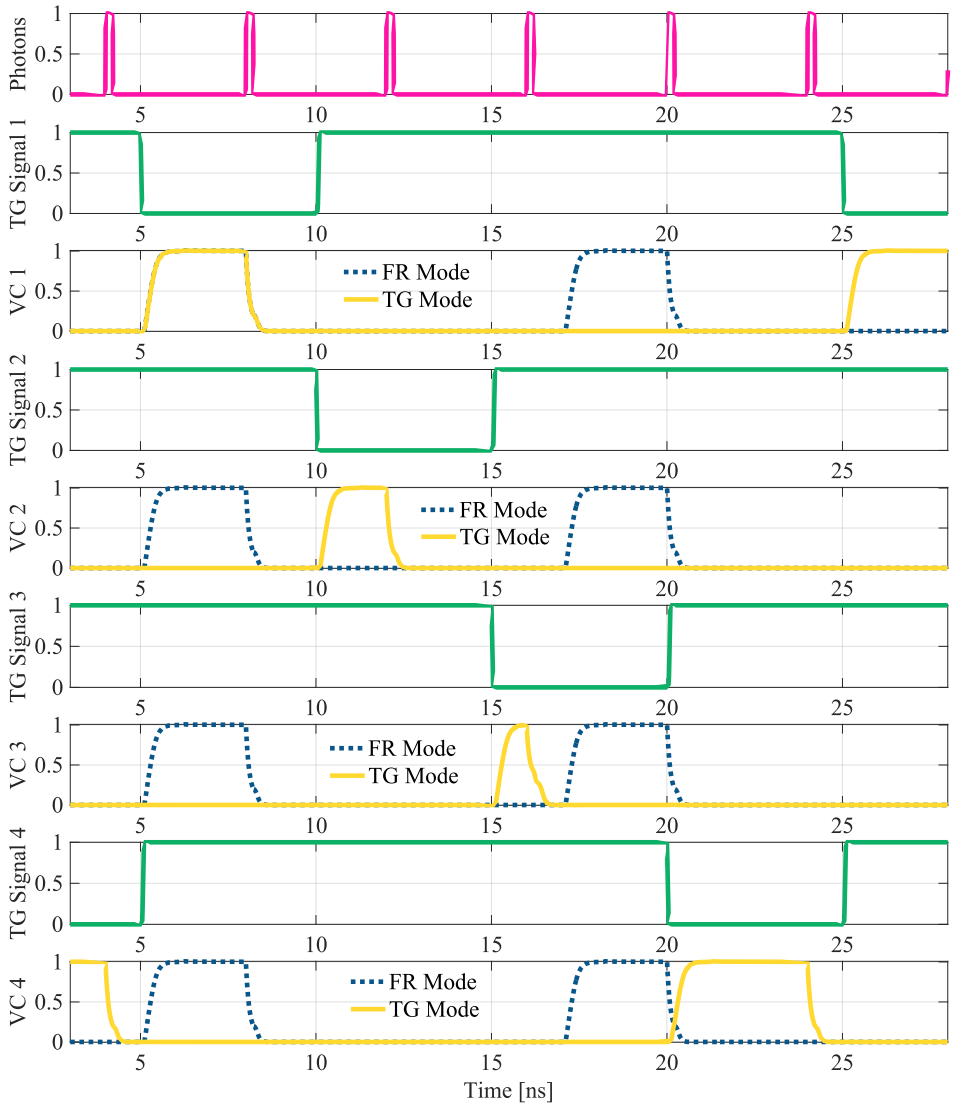

Figure 3-13: Post-layout transient simulation results for the time-gated (TG) mode SPAD front-end circuit and free-running (FR) mode SPAD front-end circuit.

In the simulation of the TG mode front-end circuit, the dead time is set to be 10 ns and bit interval is set to be 5 ns for high data rate communication. Under these conditions, every SPAD pixel can detect at most one photon in one bit interval. The post-layout transient simulation is shown in Figure 3-13, where the four SPAD pixels operate as four sub-SPAD arrays enabled cyclically by four TG circuits. Compared with the FR mode, the TG mode receiver detects 4 photons over the 4-bit intervals 4 bits, and the FR mode receiver can detect up to 8 photons but cannot detect any photon in the second and third bits due to the ISI effect. In contrast, the TG mode receiver detects one photon in every bit interval with no ISI effect. Also, compared with the FR mode, the equivalent detection time of TG mode is extended since the dead time in one channel does not affect the other channels. While the photon counting rate may reduce in TG mode, it significantly improves the detection interval consistency in optical wireless communication and has a potential to performs better than the traditional FR mode when ISI effect is very serious.

In some past research on SPAD-based OWC, the time-gated mode was primarily applied to PQR SPADs to control the extension of the dead time. In the application described in [84], the SPAD is forced off through gate-off, resulting in a significant reduction in the photon counting capability due to the prolonged dead time under high-intensity light conditions. Our research focuses on AQR SPADs with the aim of reducing the ISI effect in high-speed communication environments by utilizing the gate-off operation to enable partitioned detection across the entire SPAD array. This approach helps to minimize the block time and effectively mitigate the impact of ISI on the SPAD performance.

3.4. The 4×4 SPAD Receivers

In this project, the whole SPAD receiver is designed based on these proposed SPAD circuits. To fulfil the role of an OWC receiver, data processing and layout design are also of paramount importance. This work primarily focuses on the photon counter and data processing circuits tailored for SPAD arrays, while also addressing the overall chip layout design.

3.4.1. Photon Counter

As a photon count receiver for the OWC application, the output of single SPAD needs to be carefully processed in order to decode an accurate OWC signal. As shown in the Figure 3-14, a full SPAD pixel is composed of the time-controlled signal from the signal generator, the SPAD with front-end circuit, and the photon counter. The photon counter counts the output pulses from the front-end circuit and the number of the counted photons is represented by a 4-bit outputs. In this photon counter design, 4 D-type flip flops (DFF) are used and connected in series, the outputs are the O terminals of the 4 DFFs. As a DFF refreshes its own state under the action of rising edge of the input. When the first rising edge of the SPAD output comes, the first DFF is edge trigged and the O terminal turns to high voltage. The second SPAD output triggers the first DFF and turn the O terminal to low voltage, causing first QN terminal turns to high voltage and triggers the second DFF. The third and the fourth DFFs are operated in the same condition. The reset terminals of 4 DFFs are connected with the CD signal (In TG mode SPAD receiver, the reset terminals of photon counter also connect with the CD signal) for starting a new counting period at the beginning of the detection interval.

As shown in the Figure 3-15, the 4 outputs are composed to a 4-bit binary number and

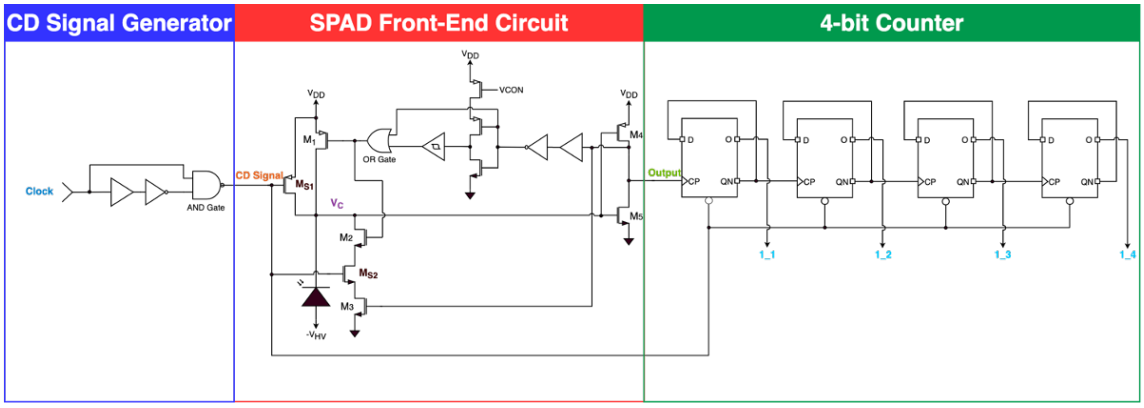

Figure 3-14: The schematic of the components in a SPAD pixel of a SPAD array.

16 photons can be detected in one detection interval at most. Overall, for a SPAD pixel circuit, the time-controlled signal generation circuit operates the SPAD front-end circuit, causing an output from the SPAD circuit with the detection of each photon. Within a bit

interval, the outputs of SPAD circuits are recorded by the photon counter and the values are transmitted to the subsequent signal processing circuitry.

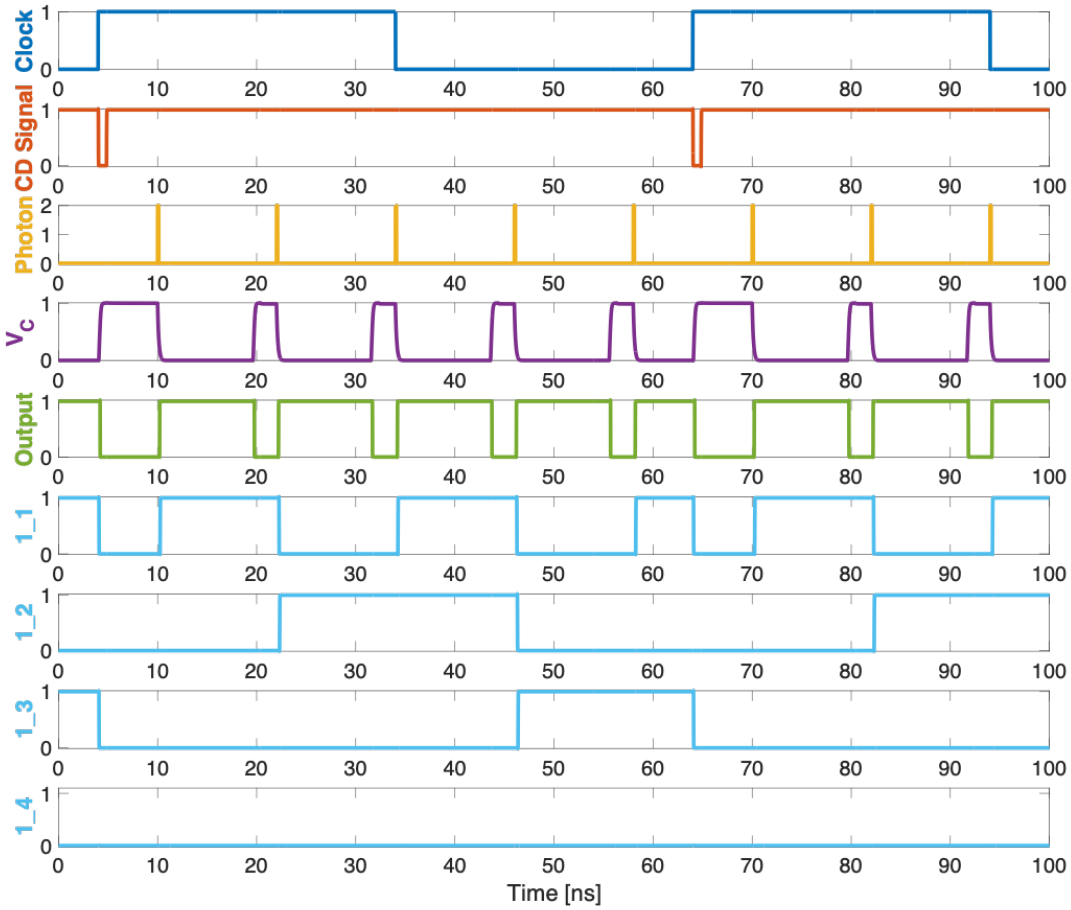

Figure 3-15: The post-layout transient simulation results for the clock-driven (CD) SPAD circuit with photon counter.

3.4.2. Data Processing Circuit

The decode processes of one SPAD array receiver include that collect the outputs of every single SPAD pixel. In this design, the data processing circuit adds the outputs of 16 SPAD pixels together simultaneously. The random incident characteristic of photons leads to a random counting process of every SPAD pixel. Thus, the data processing circuit needs to have the functions of processing all SPAD outputs at same time and changes immediately with the random incident photons.

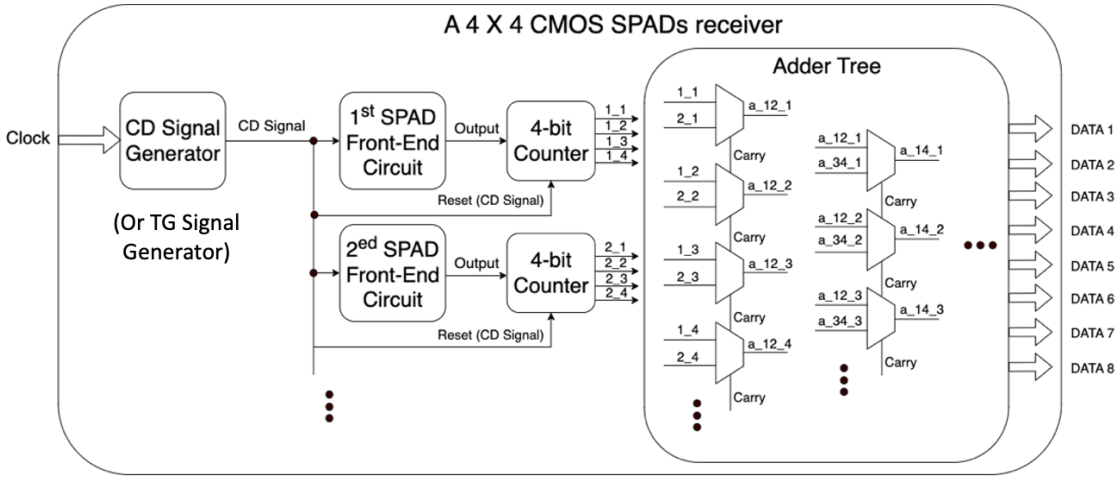

Figure 3-16: The schematic of a 4 × 4 COMS SPADs receiver.

The adder tree is implemented as the data processing circuit with an 8-bit output (data 1 to data 8). The full adders are cascaded and composed to a ripple carry adder. The adder tree is an efficient circuit structure used for performing addition operations, composed of multiple cascaded ripple carry adders that handle multi-digit number addition. In each level, the ripple carry adder takes inputs from the previous and current levels, computes sum and carry values, and passes the carry to the next level. This cascading arrangement enables each adder to simultaneously calculate the sum of multi-digit numbers, enhancing the speed of addition operations. By connecting multiple adders in series, the adder tree can execute multi-digit additions within a single bit interval. The 64 inputs (16 × 4) for this adder tree can be processed by 4-stage adder tree and the carryout of one stage is fed directly to the carry-in of the next stage. In the first stage, 8 4-bit parallel adders for the all the 4-bit outputs from SPAD pixels.

3.4.3. Layout

The layout of the 4 × 4 SPAD receiver (CD SPAD array) is shown in the Figure 3-17, and the TG SPAD array is designed by replacing the CD signal circuit to TG signal circuit. The full chip design is shown in the Figure 3-18. Concerning about the circuit drive capability, 4 CD signal circuits in this layout are placed to operate 16 SPAD pixels. In this

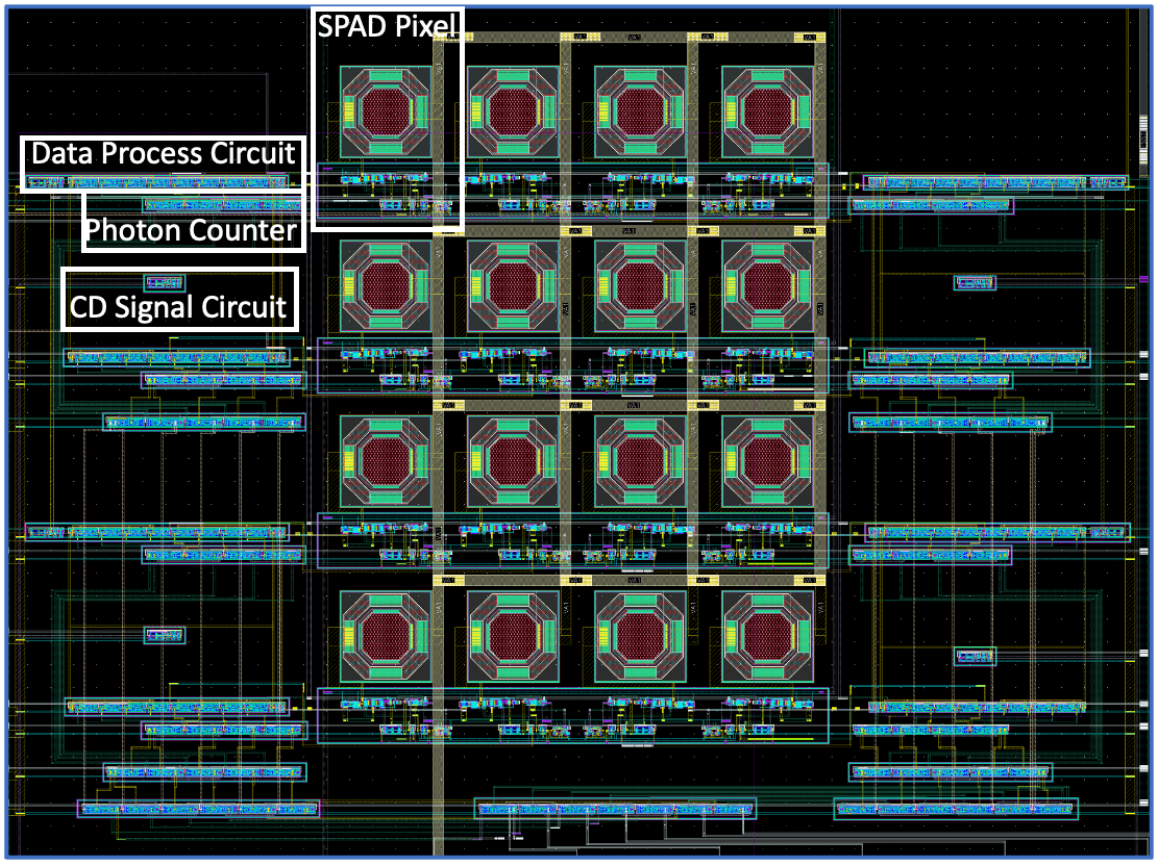

Figure 3-17: The layout design of the 4 ×4 SPAD receiver

chip, 37 pins in total are placed for the inputs, outputs and circuit control. The outputs of the first, the second, the ninth and the tenth SPAD pixels in CD SPAD array are connected

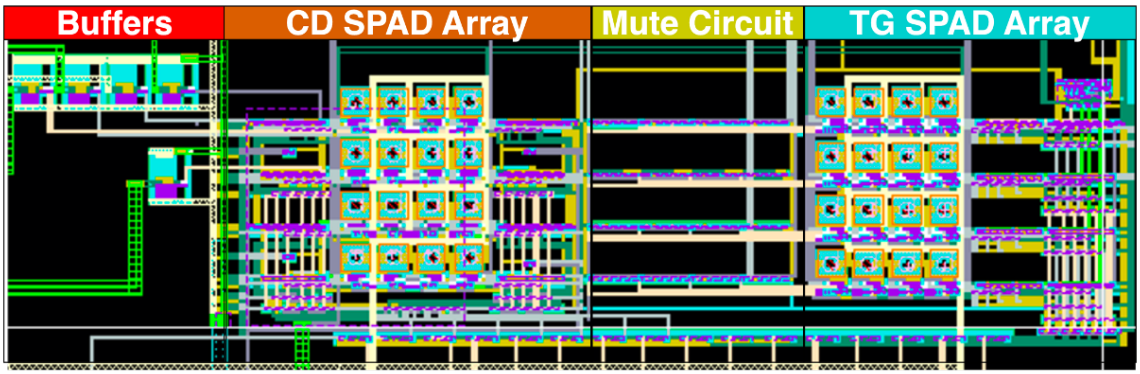

Figure 3-18: The layout design of the full chip with 2 time-controlled receivers.

to the pins straightly for measuring the SPAD performances. The mute circuit is designed for avoiding the effect from the hot pixel. In the mute circuit, every single SPAD pixel in proposed two SPAD arrays can be muted by digital input.

3.5. Conclusions

In this chapter, the circuit functions and chip design are demonstrated. The basic free-running (FR) mode is designed based on a mixed passive-active quench and reset circuit, the FR circuit has a feature of very fast dead time and adjustable hold-off time. Based on this FR circuit, the clock-driven (CD) SPAD circuit and time-gated (TG) SPAD circuit are derived for time-controlled functions. To achieve CD detection mode and TG detection mode, the CD and TG signal generation circuits with a basic clock input are designed to provide the time-controlled signals to the front-end circuits. In the CD mode, a forcible reset mechanism is added to the SPAD front-end circuit, and the interval of dead time that extends to the next bit interval is removed. In TG mode, the SPAD-array is divided to 4 sub-SPAD arrays and realise a continue detection mode, leading the dead time in one bit interval cannot affects the next bit interval. Both the CD mode and the TG mode reduce the ISI effect, and the CD mode is designed for low data rate communication and the TG mode is designed for high data rate communication.

For recording the detected photons from the proposed SPAD front-end circuit, the 4-bit photon counter is designed for every single SPAD pixel to record the outputs from SPAD pixel. An adder tree is connected to every 4-bit photon counter and add the outputs in one bit interval of all the 4-bit photon counters to calculate the final number of detected photons from the whole SPAD array. As an OWC receiver, in the design discussed in this chapter, the SPAD is employed for photon detection. The SPAD front-end circuit is responsible for quenching and resetting the SPAD, generating an output for each detected photon. The time-controlled signal generation circuit regulates the SPAD front-end circuit to define the active time interval of the SPAD. Within a bit interval, the outputs of each SPAD are recorded by a photon counter. The values of all photon counters in an SPAD array are aggregated by an adder tree, resulting in an 8-bit binary representation as the

output. To facilitate later detection and ensure stable circuit operation, buffer and mute circuits are also designed and presented in the central layout.

Chapter 4
Performance Analysis for SPAD Receivers in OWC System

4.1. Photon Detection Process in SPAD Receiver

4.1.1. Photon Counting Process

The photon arrival process can be described by the Poisson distribution [97]. The k photons can be detected with the probability of $P(k)$ in a specific time interval T, that is [97]:

$$P(k) = \frac{(LT)^k e^{-LT}}{k!} \quad 4\text{-}1$$

where the L is the average photon arrival rate, LT is the average number of arrived photons during the time interval T. For a photon detection device, photons arrival randomly, causing a random detection number of photons and expands the uncertainty in OWC system. The PDE is the quantum efficiency of SPAD. In order to consider the PDE in the photon counting process of SPAD and associate the optical power with the optical system. The average photon arrival rate L can be written as [98]:

$$L = \frac{PDE \times P_R}{hf_0} \quad 4\text{-}2$$

P_R is the received optical power in SPAD, h is the Plank constant, and f_0 is the frequency of incident photons.

As introduced in Chapter 2.1.3, the photon count of SPAD receiver is restricted by the dead time, that is an undetectable period of a SPAD after a photon is detected. This characteristic limit the effective photon count rate and it is different in AQR and PQR SPAD. For a AQR SPAD, the dead time is fixed, and the maximum count rate would be

Adapted from: J. Liu, W. Jiang, S. Kumar and M. J. Deen, "Time-Controlled SPAD Receivers in Optical Wireless Communication System," in IEEE Photonics Journal, vol. 15, no. 5, pp. 1-13, Oct. 2023, Art no. 7304113, doi: 10.1109/JPHOT.2023.3309881.

$1/T_d$. However, the effective photon count rate of PQR is always lower than the saturation count rate ($1/T_d$) due to the dead time of PQR SPAD is not fixed but extended by the incident photons during the dead time. As a typical Geiger-Muller (GM) detector with two different dead time types, SPAD with AQR and PQR can be modeled as the paralyzable device and nonparalyzable device, respectively [99]. The effective count rates L_e of SPAD receivers can be given by [97]:

$$PQR: L_e = \frac{L}{1 + LT_d} \quad 4\text{-}3$$

$$AQR: L_e = Le^{-LT_d} \quad 4\text{-}4$$

Note that, for these equations, we ignored the PDE of SPAD and only consider the dead time effect. Figure 4-1 shows the effective count rates comparisons between PQR and AQR, the dead time for SPAD is given from 50 ns to 150 ns. As shown, AQR and PQR SPADs follow the rise trend in low photon rate values due to the count rates do not reach the saturation photon count rate and the effective dead times for both AQR SPAD and PQR SPAD are same. For these higher photon rate values, the effective count rates of PQR

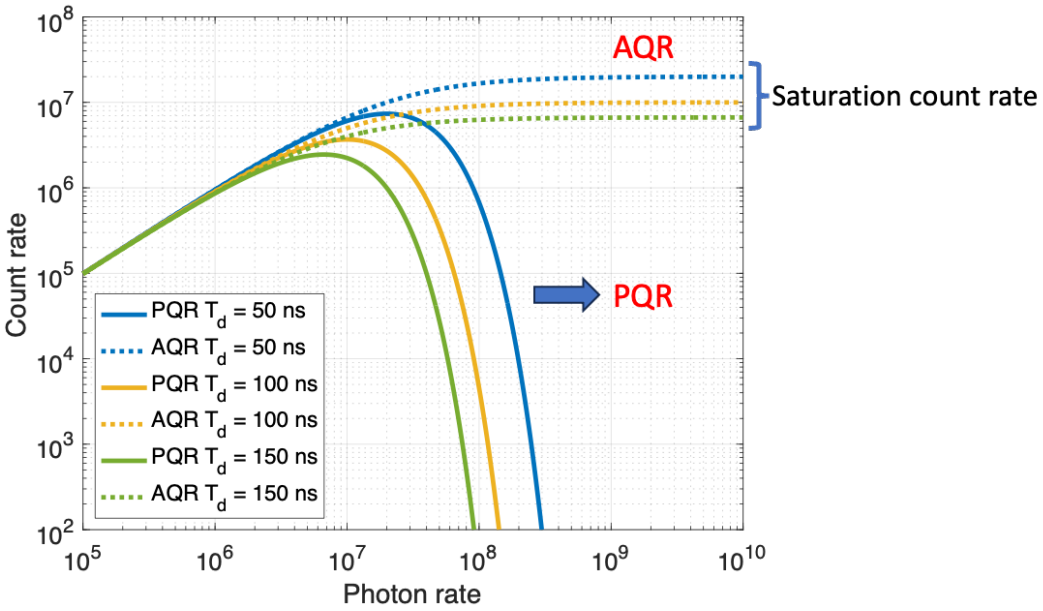

Figure 4-1: The relationship between the count rate and the photon rate comparisons of the active quench and reset (AQR) circuit and the passive quench and reset (PQR) circuit with different dead times.

decreases very fast after getting the peak values, that is because in the high photon rate conditions, the photons incident during the dead time that can extend the dead time, thus causing the less photons can be detected. For AQR, if the given photon rate is high, the effective count rate keeps constant due to the dead time is constant. Lower dead time brings lower effective count rate in both AQR and PQR SPADs.

4.1.2. Photon Count Probability Distribution

With the effective photon count rate of SPAD is derived and the photon arrival process is considered, the photon count statistics of SPAD in a time interval can be analysed. The photon count probability distribution demonstrates all the number's probabilities of the photons that SPAD can detect in a time interval. This probability distribution with its mean and variance values are highly related with the performance of SPAD receiver and can be expressed as [100] [101]:

$$p_K(k) = \begin{cases} \sum_{i=0}^{k} \psi\,(i, \lambda_k) - \sum_{i=0}^{k-1} \psi\,(i, \lambda_{k-1}) & k < k_{max} \\ 1 - \sum_{i=0}^{k-1} \psi\,(i, \lambda_{k-1}) & k = k_{max} \\ 0 & k > k_{max} \end{cases} \quad 4\text{-}5$$

$$k_{max} = \left\lfloor \frac{T_s}{T_d} \right\rfloor + 1 \quad 4\text{-}6$$

$$L = \frac{PDE \times P_O}{N h f_0} \quad 4\text{-}7$$

where the function $\psi(i, \lambda)$ is defined as $\psi(i, \lambda) = \lambda^i e^{-\lambda}/i!$, and $\lambda_k = L(T_S - kT_d)$; k is the number of detected photons, k_{max} is the maximum value of k , T_S is the detection time interval and P_O is the received optical power, N is the number of SPAD pixels in a SPAD array and f_0 is the light frequency. For the consistency of the simulation results, we refer to our previous research [82] and set N to be 64, T_d to be 10 ns, PDE to be 38%, and f_0 to be 7.138×10^{14} Hz (wavelength = 420 nm) in all the following simulations (Figure 4-6 to Figure 4-13). The mean and variance of the photon counting probability distribution for the Equation 4-5 are [101]:

$$\mu_k = k_{max} - \sum_{k=0}^{k_{max}-1} \sum_{i=0}^{k} \psi(i, \lambda_{k-1}) \tag{4-8}$$

$$\sigma_k^2 = \sum_{k=0}^{k_{max}-1} \sum_{i=0}^{k} (2k_{max} - 2k - 1)\psi(i, \lambda_{k-1}) - \sum_{k=0}^{k_{max}-1} \sum_{i=0}^{k} \psi(i, \lambda_{k-1}) \tag{4-9}$$

ISI Effect Simulation

As mentioned in the Section II.B and II.C, the dead time of SPAD may cause ISI effect in the FR mode, thus degrading the receiver performance. Figure 4-2 demonstrates the block time generation process, where T_b is the block time. The last detected photon in the first bit causes the dead time, but this dead time may extend to the second bit and cause an inactive interval. This is the process how the block time is generated [102]. Due to the existence of the block time, the effective photon detection time of every bit will be reduced to T_S-T_b, thus resulting in a reduced photon counting in an OWC system.

For a SPAD receiver, the arrival time of the incident photon is random and follows the Poisson arrival process [101]. As a result, the block time of every SPAD pixel in each bit of the OWC system is different even under the same condition. To solve this problem, Monte Carlo simulation is introduced to obtain the numerical analysis of the block time. The block time in one bit interval is mainly determined by the detected time of the last detected photon in the previous bit interval. For example, in Figure 4-2, the last detected

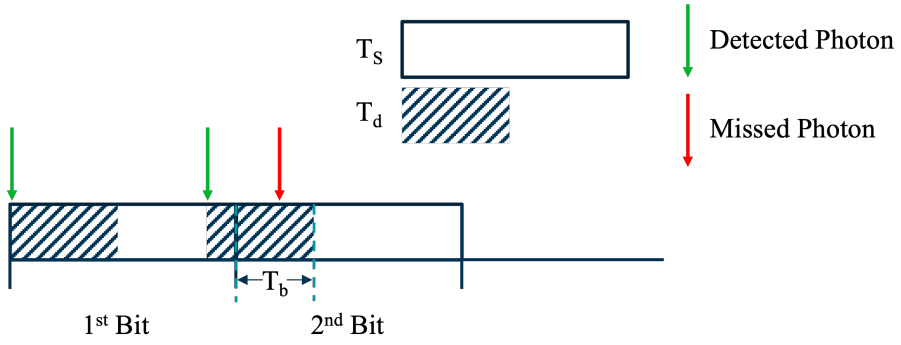

Figure 4-2: The diagram of block time generation process.

photon in the 1st bit leads to the block time T_b in the 2nd bit. Therefore, the focus of Monte Carlo simulation is to analyze the detected time of the last detected photon in the first bit interval.

As the value of photons detected, k in the first bit can be used to analyze the possible time of the last detected photon in the first bit and the photon counting distribution can be used as the probability distribution to calculate the block time (T_b) of the second bit, which can be expressed as:

$$T_b = \max\{T_d - rand(0,1) \times [T_s - (k-1)T_d], 0\} \quad 4\text{-}10$$

Although the probability of the total number of detected photons k can be calculated, the detection time of each photon is still random. The term $(k-1)T_d$ represents a time when the last photon could not be incident, that is, the last photon is not incident during [0, $(k-1)T_d$], and $[T_s - (k-1)T_d]$ is the available time for the last photon. The term *rand(0,1)* is used to the randomly generated available time when the last photon can be incident, and the term $rand(0,1) \times [T_s - (k-1)]T_d$ represents the detected time of the last detected photon in the first bit interval. $T_d - rand(0,1) \times [T_s - (k-1)T_d]$ is the full dead time minus the dead time that is in the current bit interval, that is, the block time for the next bit interval. The average block time can be calculated after 10^6 times simulations to ensure the accuracy. The results are shown in Figure 4-4, the dead time ratio is defined as T_d/T_s, which is a parameter to show the dead time effect in a OWC system. The effective detection time ratio is defined as $(T_s - T_b)/T_s$, serves as a parameter to quantify the impact of ISI, with a lower effective detection time ratio indicating a more pronounced ISI effect.

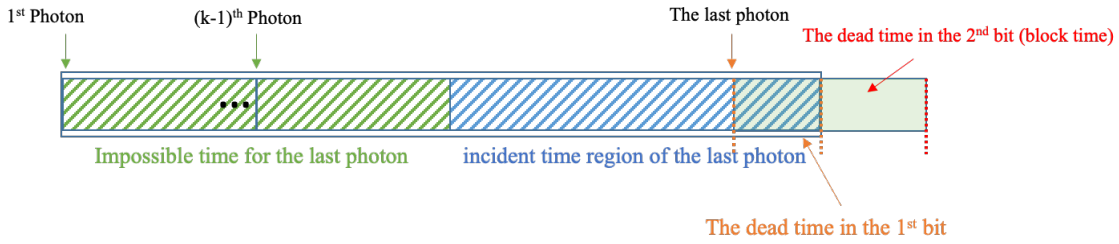

Figure 4-3: The diagram to describe the simulation process of intersymbol interference (ISI) effect.

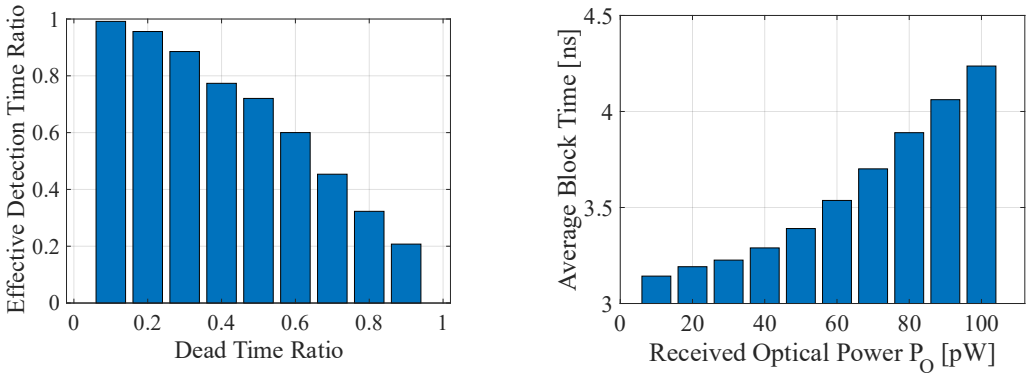

Figure 4-4: (a). The average block time ratio of the variant dead time ratio when P_O = 60 pW, and (b), the average block time of the variant received optical power when T_b = 10 ns and T_S = 20 ns.

In Figure 4-4 (a), a negative correlation is observed between the dead time ratio and the effective detection time ratio, suggesting that the dead time significantly influences the block time. For example, when the dead time ratio is large it can lead to a serious ISI effect in the OWC system. The block time increases with the increase of the received optical power as shown in Figure 4-4 (b). This is because that a higher chance for photon to arrival at the end of first interval will result in a higher probability of extending the dead time to the second bit interval.

The FR mode SPAD receiver suffers from the short effective detection interval because the block time occupies a faction of total bit interval. For a SPAD array, every SPAD pixel is an independent photon counter. As a result, the block time is different for different SPAD pixels. Based on the Equation 4-8 and Equation 4-9, the mean and variance of photon counting probability distribution in a free-running SPAD array can be written as:

$$\mu_{kf} = \sum_{j=1}^{N}\left[k_{maxj} - \sum_{k=0}^{k_{maxj}-1}\sum_{i=0}^{k}\psi(i,\lambda_{(k-1)j})\right] \tag{4-11}$$

$$\sigma_{kf}^2 = \sum_{j=1}^{N}\left[\sum_{k=0}^{k_{maxj}-1}\sum_{i=0}^{k}(2k_{maxj}-2k-1)\psi(i,\lambda_{(k-1)j}) - \sum_{k=0}^{k_{maxj}-1}\sum_{i=0}^{k}\psi(i,\lambda_{(k-1)j})\right] \tag{4-12}$$

$$k_{maxj} = \lfloor (T_s - T_{bj})/T_d \rfloor + 1 \quad 4\text{-}13$$

$$\lambda_{kj} = L(T_s - T_{bj} - kT_d) \quad 4\text{-}14$$

where k_{maxj} is the maximum number of the counted photons for the j^{th} SPAD pixel and T_{bj} is the block time of the j^{th} SPAD pixel, the $\square_{kf}$ and σ_{kf}^2 are the summation of all the counting means and counting variances from the single SPAD pixel in a SPAD array.

4.2. SPAD Receivers for On-Off Keying Modulation

4.2.1. Concept of OOK Modulation

On–off keying (OOK) denotes the simplest form of amplitude-shift keying (ASK) modulation that represents digital data as the presence or absence of a carrier wave [103], and it is also one of the most popular modulations implemented in OWC. In OOK modulation, the source transmits a large amplitude carrier when data '1' is sent, and it sends a small amplitude carrier for bit '0'. In a specific duration with a data of '1' or '0', signal in receivers can be represented by the electric signals that higher or lower than a threshold.

As shown in Figure 4-5, in SPAD-based OOK modulation communication, the number of detected photons during a bit interval is the electric signal that can be used to represent

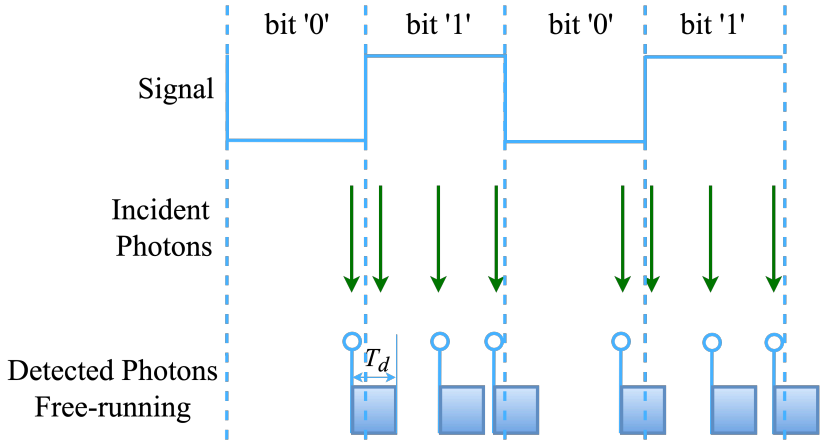

Figure 4-5: The diagram to demonstrate the principle of the SPAD-based on-off keying (OOK) modulation.

data by comparing with a specific number. Transmitters under SPAD-based OOK modulation generate signal optical pulse in bit ‘1’ and keep close in bit ‘0’, thus causing SPAD receivers triggered by signal optical light and background noise in bit ‘1’ and only triggered by background noise in bit ‘0’. Error bits happened when counted photons in bit ‘1’ lower than the threshold number and count more photons than threshold number in bit ‘0’ [97].

In SPAD-based OWC, OOK modulation serves as a significant modulation scheme, exhibiting distinct advantages and drawbacks [104]. From a standpoint of advantages, OOK modulation is characterized by its simplicity and compatibility, rendering it suitable for SPAD receivers and straightforward to implement. Its high sensitivity at low light levels enables reliable data transmission, making it well-suited for applications requiring moderate data rates. However, on the flip side, OOK modulation is susceptible to the influence of background noise, particularly in environments with strong noise or optical interference, which could lead to performance degradation [86]. In comparison with alternative modulation techniques such as phase modulation and frequency modulation (such as phase-shift keying (PSK) modulation or quadrature amplitude modulation (QAM)), OOK mod’lation's primary advantage lies in its simplicity and compatibility with SPAD receivers. However, phase modulation can achieve higher spectral efficiency at certain signal-to-noise ratios, making it suitable for high-rate applications. Conversely, frequency modulation may find greater applicability in certain scenarios. Therefore, the selection of a modulation scheme necessitates a comprehensive assessment of the pros and cons of different approaches, accounting for specific application requirements like data rate, distance, and noise environment.

In conclusion, OOK modulation plays a pivotal role in SPAD-based OWC, leveraging its simplicity, compatibility, and suitability for low-light conditions. Nevertheless, in real-world applications, a trade-off must be made considering its susceptibility to background noise and lower spectral efficiency, in order to fulfill specific transmission needs.

4.2.2. OWC Model for OOK Modulation

BER Evaluation

In this research, OOK modulation is used for the simulations of SPAD-based communication system. As the single photon detector, a SPAD receiver judges the signal through the detected photon number. The number of detected photons in a bit interval is compared with a certain threshold. If the detected number of photons is greater than the threshold, the decision device decides '1' is sent; otherwise, it is decided that '0' is sent. The optimal threshold is a specific threshold value to achieve the lowest BER. It can be expressed as Equation 4-14 [105], and the BER of OOK communication with optimum threshold can be expressed as [77]:

$$y_{th} = \frac{\frac{\mu_0}{\sigma_0^2} - \frac{\mu_1}{\sigma_1^2} + \sqrt{(\frac{\mu_0}{\sigma_0^2} - \frac{\mu_1}{\sigma_1^2})^2 - (\frac{1}{\sigma_0^2} - \frac{1}{\sigma_1^2})[\left(\frac{\mu_0^2}{\sigma_0^2} - \frac{\mu_1^2}{\sigma_1^2}\right) + 2\ln(\frac{\sigma_0}{\sigma_1})]}}{\frac{1}{\sigma_0^2} - \frac{1}{\sigma_1^2}} \quad 4\text{-}14$$

$$BER = \frac{1}{2}\sum_{y=\lfloor y_{th} \rfloor + 1}^{\infty} p_y^0(y) + \frac{1}{2}\sum_{y=0}^{y_{th}} p_y^1(y) \quad 4\text{-}15$$

where the □j, and σ_j^2 are the mean and variance of the photon counting distribution of bit *j*, *j* = 0, 1, respectively. $p_y^0(y)$and $p_y^1(y)$ denotes the photon counting probabilities of bit 0 and bit 1, respectively. Because of the different photon detected rate (L) for bit '1' and bit '0', their photon condition rates differ. for bit '1', the SPAD receiver receives light from the transmitter and background noise. However, for bit '0', the receiver receives only the background noise. The BER given at Equation 4-15 can be approximated as [86]:

$$BER \cong Q(\sqrt{SNR}) \quad 4\text{-}16$$

$$SNR = \left(\frac{\mu_1 - \mu_0}{\sigma_1 + \sigma_0}\right)^2 \quad 4\text{-}17$$

Q(x) is the Q-function, which is $Q(x) = {}^{1}/_{\sqrt{2\pi}} \int_x^{\infty} \exp(-\alpha^2/2)\, d\alpha$. Since all noise in this model is integrated into background power (P_b), signal-to-noise ratio (SNR) can be represented by Equation 4-17. Signal power is defined by the mean of the photon counting

distributions of bit '1' and bit '0', noise power comes from the variance of '1' counting distribution and '0' counting distribution. The average photon detection rate of bit '1' and bit '0' can be written as [106]:

$$L_1 = \frac{PDE \times (P_R + P_b)}{Nhf_0} \quad 4\text{-}18$$

$$L_0 = \frac{PDE \times P_b}{Nhf_0} \quad 4\text{-}19$$

where P_R is the received signal power and P_b is the received background power. N, PDE, h and f_0 are defined in Section III.

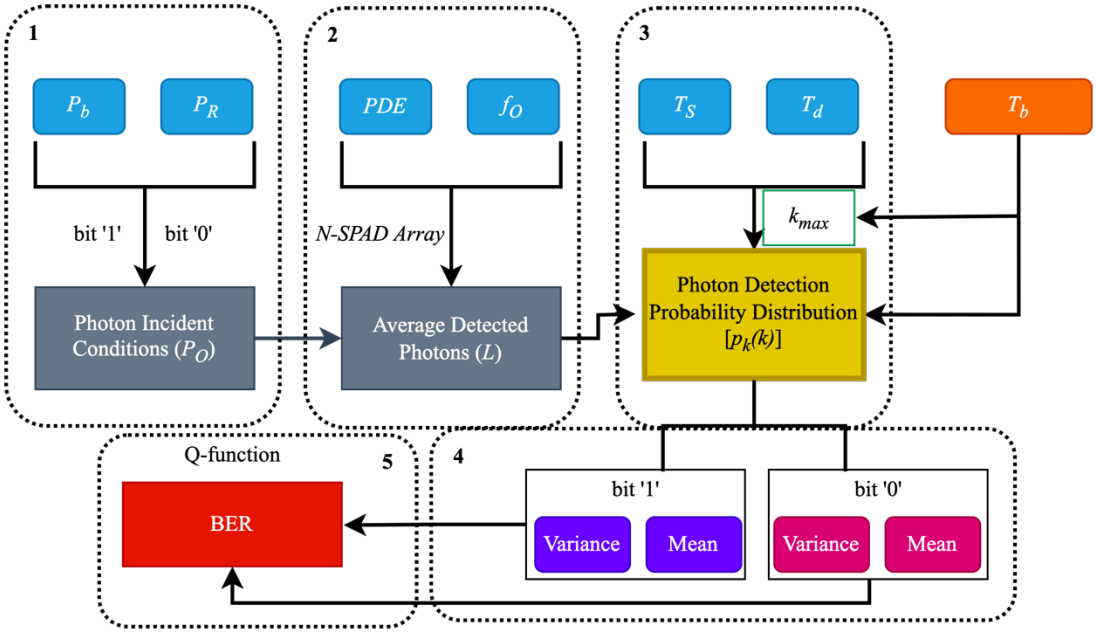

Figure 4-6: The schematic of the SPAD-based OWC model with the on-off keying (OOK) modulation.

4.2.3. Clock-driven Mode SPAD Receiver for OOK Modulation

As introduced in Section II.B, the CD mode SPAD receiver can reset SPAD from the hold-off status. Therefore, no dead time can extend to the next bit interval. That is, the effective detection times of every bit interval are equal. The photon counting probability distribution of every bit interval in CD mode follows (1a), which has no ISI effect. Compared to the FR-mode SPAD receiver, the SPAD operated in CD mode has the

advantage of no ISI effect brings longer effective detection time. Therefore, the CD-mode SPAD has a higher photon detection ability than the FR mode.

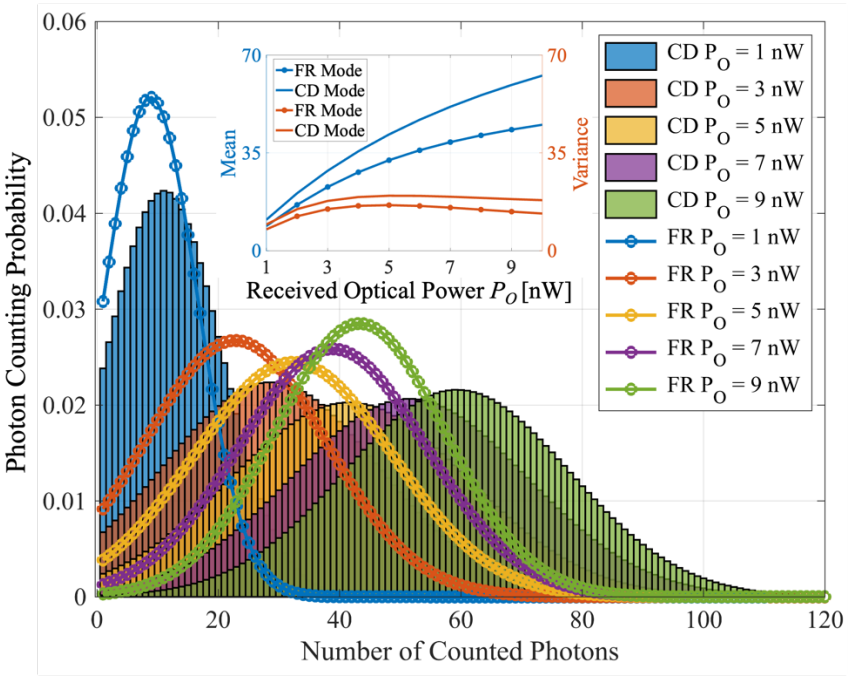

Figure 4-7: Photon counting probability distribution variances of the clock-driven (CD) mode and the free-running (FR) mode with the increased optical power (64-SPAD array with 10 ns dead time and 15 ns bit interval).

The photon counting probability distributions based on unmodulated signals can be observed in Figure 4-7 and Figure 4-8. In Figure 4-7, with the increase of the received optical power (P_O), the number of detected photons increases, leading to the photon counting probability distributions of the CD and FR modes moving to the right, which represents higher mean values. In the high optical power condition (P_O = 9 nW), a significant gap exists between the CD mode and the FR mode due to the higher average values of counted photons in the CD mode. The mean value of the photon counting distribution increase with the increase of P_O. In Figure 4-7, when P_O is 1 nW, the variance value of the CD mode distribution is 9.42, while that of the FR mode is 7.66. However, when P_O is 9 nW, the variance value of the CD distribution is 18.48, while that of the FR mode is 14. In the case of $T_S > T_d$, the gap in variance values of the two modes is not changed too much with the increase of P_O, because the block time is not long compared to the entire bit interval.

Figure 4-8 shows the photon counting probability distributions variance with different bit intervals (T_S). The increased T_S values lead to a smaller dead time ratio. In addition, the difference between the CD mode distribution and the FR mode distribution in large bit interval (T_S = *50* ns) is small because the block time is short enough thus the ISI effect can be ignored in the FR mode. The inserted figure in Figure 4-11 shows an approaching trend of two mean values with the increase of the bit interval, which indicates that the ISI effect on the FR receiver gets smaller with the increase of the bit interval. In the case of a short T_S (T_S = 20 ns), a gap in variance between CD and FR distributions can be observed (24.49

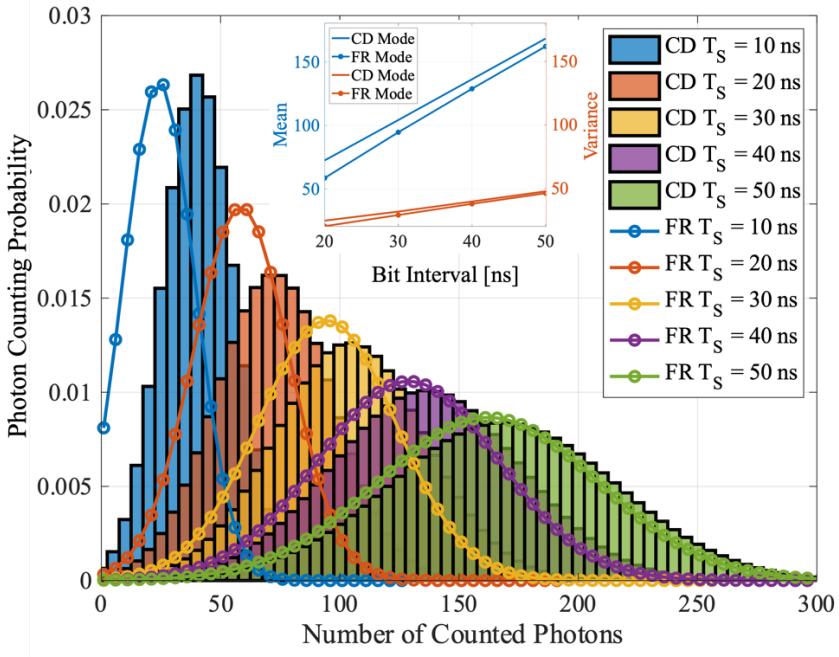

Figure 4-8: Photon counting probability distribution variances of the clock-driven (CD) mode and the free-running (FR) mode with the increased bit interval (TS) when PO = 8 nW (64-SPAD array with 10 ns dead time).

for the CD mode and 20.11 for the FR mode). The reason for this gap is because in the CD mode, the receiver has a longer effective detection time, resulting in a larger variance value. On the contrary, when T_S = 50 ns, the distributions of the two modes are highly coincident, which means that the gap in the variance value almost disappears. This is because the very long T_S causes the proportion of block time in the entire bit interval become very small, making the ISI effect negligible.

The probability distribItions in Figure 4-7 and Figure 4-8 demonstrate that the CD-mode SPAD receiver has a higher photon counting ability than the FR mode, especially under high optical power or low bit interval conditions. This is because that the CD mode is not affected by the block time under these two conditions. These features make the CD mode to have better performance than the traditional FR mode in OWC system.

For this section, we present the numerical results of the BER in different modes, which are simulated and compared. BER comparisons of the CD mode and the FR mode using different variables are illustrated in Figure 4-9 and Figure 4-10. The simulations are performed with T_s set to be 15 ns to ensure the low data rate condition ($T_s > T_d$). As shown in Figure 4-9 for three different background powers (P_b), and SNR simulation under same condition is inserted in this figure. As the P_R increases, both the CD mode and the FR mode follow a rising trend in the BER performance even the increased P_R leads to an increased block time in the FR mode receiver. That is because the SNR improvement from the increased signal power compensates for the performance decline from the block time, thus increasing the system performance. CD mode always achieves lower BER than the FR mode under the same P_R condition due to the higher photon counting rate that caused by longer effective detection time. This reason can be observed in Figure 4-9, that is, compared to the FR mode, the distribution of the CD mode will always have a higher mean value. The ISI effect can be observed through the BER gap between the CD mode and the FR mode. The BER gap is expanded with the incremental P_R value caused by the increasing block time in FR mode and can be observed in Figure 4-4 (b). In addition, the background power will affect BER's variance to P_R increases. For example, when P_b = 1 nW, as the received signal, P_R decreases from 1 ns to 6 ns, the BER decreases by a factor of 10^6 (10^{-1} to10^{-7}), while when P_b = 4 nW, the BER drops only by a factor of 10^2. This is because background noise will increase the variance value of distributions in bit 1 and bit 0, thereby reducing the SNR. Another problem caused by background noise is the contribution to

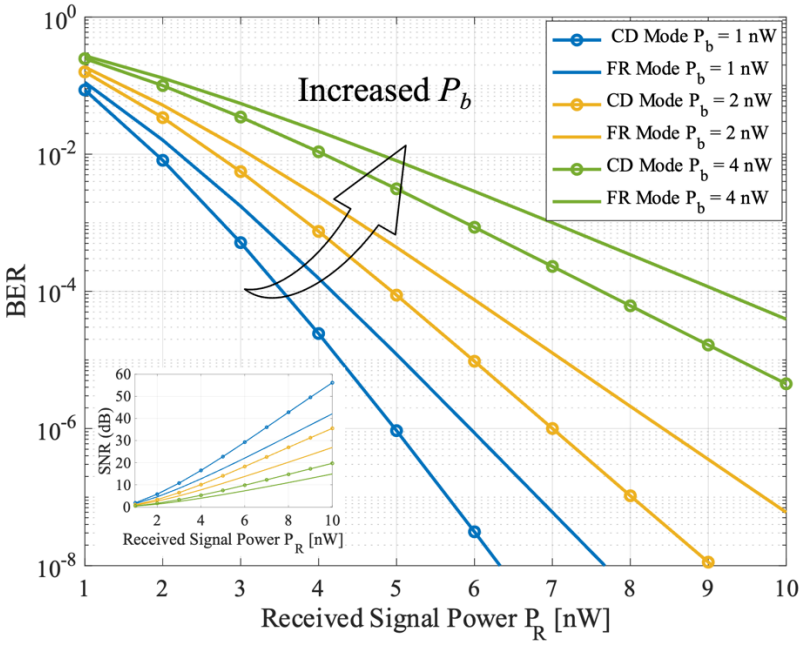

Figure 4-9: BER comparisons of the clock-driven (CD) mode and free-running (FR) mode under variant received signal power and background power with TS = 15 ns (64-SPAD array with 10 ns dead time).

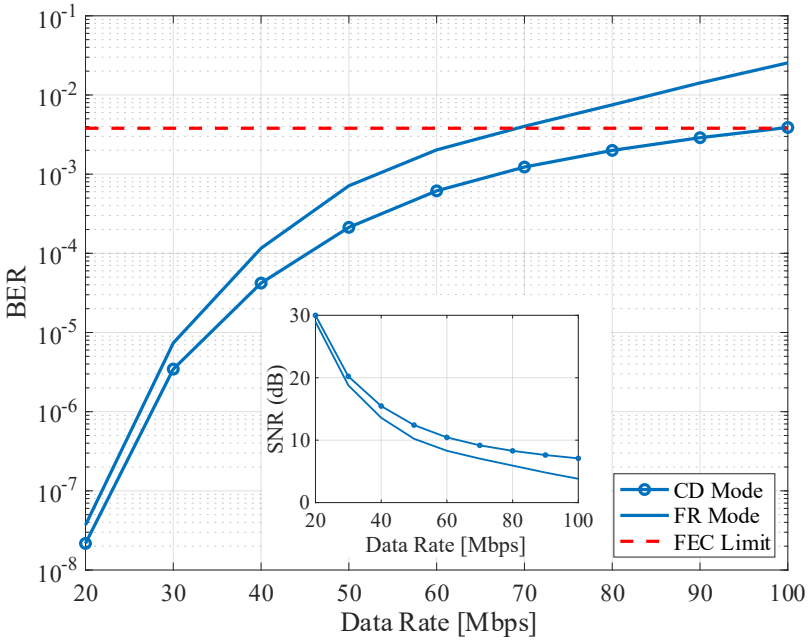

Figure 4-10: BER comparisons of the clock-driven (CD) mode and free-running (FR) mode under variant data rate with PR = 5 nW and Pb = 3 nW (64-SPAD array with 10 ns dead time).

block time, and since the CD mode does not have block time, it has a better tolerance to

background noise.

Figure 4-10 illustrates the BER variance with the increased data rate, and SNR simulation is inserted in this figure. In OOK modulation, the data rate (bps) can be calculated as $\frac{1}{T_S}$. Therefore, the BER increases with the data rate in both the CD mode and the FR mode due to the decreased T_S. As the data rate increases, the symbol interval decreases and the BER increases since the effective detective time decrease. According to Equation: 4-16 and Equation: 4-17, both BER and SNR are strongly affected by the mean values. Under low background power condition, $(\mu_1 - \mu_0)^2 \cong \mu_1$, and as T_S decreases, μ_1 reduces leading to a performance degradation of the OWC system. The lower performance of the FR mode results from the lower effective detection time due to the ISI effect. The increasing performance gap between the CD mode and the FR mode is because that the ISI effect on the BER performance becomes more and more obvious with the increase of the data rate. This is as shown in Figure 4-4 (a). The higher data rate corresponds to a higher dead time ratio, which will also decrease the effective detection time ratio due to the block time. As a result, at the forward error correction (FEC) limit of 3.8×10^{-3}, the maximum available data rate for the FR mode in this condition is 70 Mbps and the maximum available data rate for the CD mode is 100 Mbps.

4.2.4. Time-gated Mode SPAD Receiver for OOK Modulation

The TG signal operates four sub-SPAD arrays for the high data rate condition, in which the dead time is longer than the bit interval. In this condition, the block time for one single SPAD pixel is able to cover several entire bit intervals and the FR mode is no longer accurately described by Equation 4-11 to Equation 4-14.

Instead, the photon counting process can be modeled as a Bernoulli process with two states for each SPAD pixel [107]. State 1 for blocking, which indicates that no incident photon can be detected and state 0 for detection, where at most one incident photon can be possibly detected [108]. The Markov chain can be used to model the photon counting process. The mean μ_k' and variance $\sigma_k'^2$ of the photon counting probability distribution for the FR mode in high data rate condition can be expressed as [107], [108]:

$$\mu_k' = N\frac{LT_S}{1+mLT_S} \quad 4\text{-}20$$

$$\sigma_k'^{\,2} = N\frac{LT_S + (m-1)L^2{T_S}^2}{(1+mLT_s)^2} \quad 4\text{-}21$$

$$m = \frac{T_d}{T_S} \quad 4\text{-}22$$

where N is the number of SPAD pixels in a SPAD array, L is the average photon detection rate (photons/s). As introduced in Section II.C, the TG mode SPAD receiver effectively alleviates the ISI effect through continuous detection by cyclically enabling the TG window of each sub-array. However, this approach reduces the effective number of SPAD pixels available for photon detection and decreases the received optical power to 25% (only 25% SPAD pixels are available for one sub-SPAD array). In the receiver design of Figure 3-12, a 64-SPAD array receiver operated in TG mode is equivalent to a 16-SPAD array receiver without the ISI effect. Consequently, the mean and variance of photon counting probability distribution of the FR mode in the high data rate condition can be expressed by Equation 4-20 and Equation 4-21, respectively. The mean and variance of photon counting probability distribution of the TG mode can be calculated by Equation 4-11 and Equation 4-12, respectively, by replacing the total SPAD number with the effective SPAD number and reducing the received optical power and background power by 75%.

The comparisons of the TG mode and the FR mode under different optical power conditions are shown in Figure 4-11, and the bit interval is shorter than the dead time. Unlike the CD mode, which achieves higher mean values of photon counting distribution by leveraging its high photon detection ability, the TG mode relies on the less effective detectable SPAD pixels, resulting in a low photon detection ability. Consequently, the photon counting distributions of the TG mode have lower mean values than the FR mode due to the less effective detection pixels. When optical power (P_O) is 1 nW, the mean value of photon counting probability distribution of TG mode is 1, which is lower than that of FR mode (3.5). However, the TG mode offers a solution to the issue of uneven effective

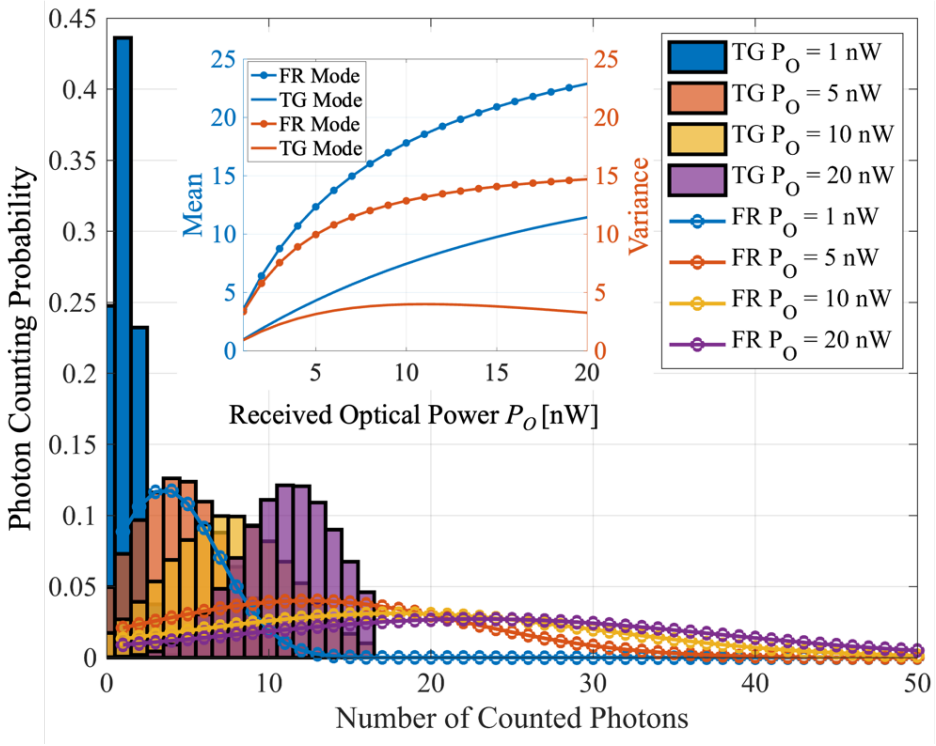

Figure 4-9: Photon counting probability distribution of the time-gated (TG) mode and the free-running (FR) mode under variant optical power (64-SPAD array with 10 ns dead time and 5 ns bit interval).

detection time caused by the ISI effect in high data rate communication. This can be observed and compared by the variance distributions. As shown in the inserted figure in Figure 4-11, the increased gap of the variances comparison with the increased received optical power shows that the condition of uneven detection time caused by ISI effect becomes more serious in the FR mode. Thus, the TG mode exhibits better performance in high optical power conditions. The stronger P_O expands the number range of photon detection of the SPAD. Moreover, due to the ISI effect, the effective detection time of the SPAD also changes greatly. These two factors lead to the trend of the variance of FR mode distribution increasing with the increase of P_O. In contrast, when the ISI effect is eliminated, the variance of TG mode distribution first rises and then falls with the increase of P_O. Specifically, when P_O ranges from 1 nW to 10 nW, the variance value of TG mode increases, because increased P_O expands the range of photon detection number of TG SPAD. However, when P_O is greater than 10 nW, the detected photon number keeps approaching the photon detection limit of TG SPAD, thus decreasing variance value.

Effects from the bit interval are shown in Figure 4-12. The advantages of the TG mode are mainly evident in the short bit interval situations. For example, when T_S = 2.5 ns, the

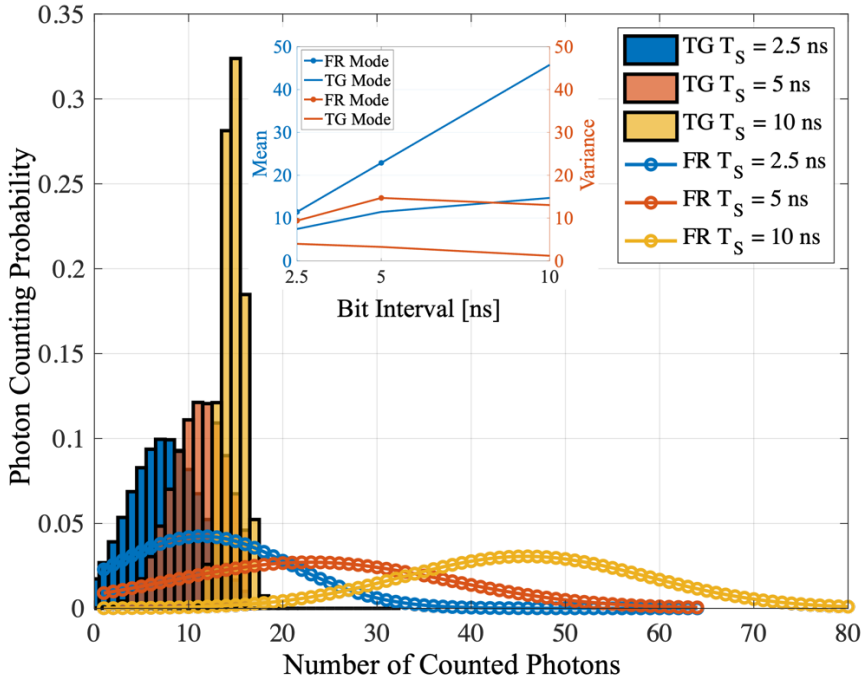

Figure 4-10: Photon counting probability distribution of the time-gated (TG) mode and the free-running (FR) mode under variant bit intervals when PO = 20 nW (64-SPAD array with10 ns dead time).

TG mode distribution has a lower variance value and similar mean value when compared to the FR mode. However, when the bit interval is relatively longer (for example, T_S = 10 ns), the FR mode distribution has a higher variance value than the TG mode distribution. Moreover, the mean value of the FR mode distribution (46.56) is much higher than that of the TG mode distribution (17.21) when the bit interval is 10 ns. In such cases, the advantages of the TG mode are no longer apparent, and the FR mode is expected to perform better in the OWC system.

A trade-off needs to be considered in the application of the TG mode. Similar to the CD mode, the TG mode SPAD receiver can efficiently reduce the ISI effect. However, less effective detection pixels due to the cyclic enabling detection mode cause a low photon counting ability. The TG mode is designed for high data rate condition with the feature of the high detection interval consistency. High optical power condition can increase the number of detected photons and alleviate the drawback caused by less effective detection

pixels in the TG mode. As a result, TG mode receiver has a potential in the OWC application for the conditions of high data rate and high optical power.

When implementing the TG mode for the BER evaluation, we need the high optical power condition and high data rate condition to demonstrate the advantages of the TG mode. In Figure 4-13, the T_S is set to be 5 ns, which is shorter than the T_d (10 ns). Since there is no ISI effect, BER variation trend of the TG model is similar to Figure 4-9. For the FR mode, the average effective photon detection time per bit interval is very small due to very severe ISI effects, which is even more pronounced at high P_R condition. In this case, the improvement in system performance caused by the increase in signal power will not be significantly greater than the decrease in system performance caused by the ISI effect, so the improvement in BER of the FR mode saturates as the received signal power increases (see Figure 4-13). From the perspective of Monte Carlo simulation and Equation 4-16 and Equation 4-17, since the block time is random, the effective detection time of each bit for FR mode is constantly changing (ranging from 0 to T_S), which will lead to a large variance of photon count distribution of bit 1 and bit 0. In other words, compared with TG mode,

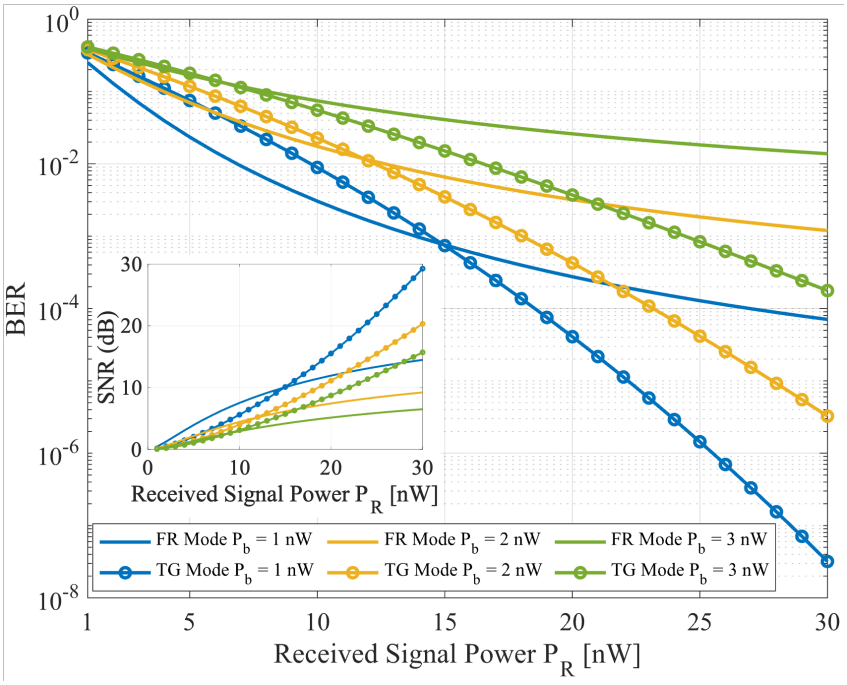

Figure 4-11: BER variation comparisons of the time-gated (TG) mode and the free-running (FR) mode under variant received signal power with T_S = 5 ns (64-SPAD array with 10 ns dead time).

the $(\sigma_1 + \sigma_0)$ value of FR mode is much greater, which will seriously affect the performance of SNR and BER. The TG mode operated in this condition can only achieve better performance than the FR mode in high signal power communication. For example, under the condition of P_b = 1 nW, as shown in Figure 4-13, the FR mode has lower BER when P_R is lower than 15 nW, while the TG mode perform better when P_R is higher than 15 nW. This is because that the ISI effect is not so obvious when the received optical power is low. Therefore, the FR mode receiver has more effective detection pixels to achieve better photon detection ability. On the contrary, the FR mode suffers from the severer ISI effect in the high optical power condition. The advantage of no ISI effect in TG mode contributes to better performance. The background noise has a negative impact on performance. In the FR mode receiver, the background power causes ISI effect. Under high background power condition, the TG mode shows its advantage. As shown in Figure 4-13, TG mode in low background power (P_b = 1 nW) requires higher received signal power (P_R > 15 nW) to perform better than the FR mode. However, only 5 nW P_R is needed by the TG mode to outperform the FR mode in high background power condition (P_b = 3 nW).

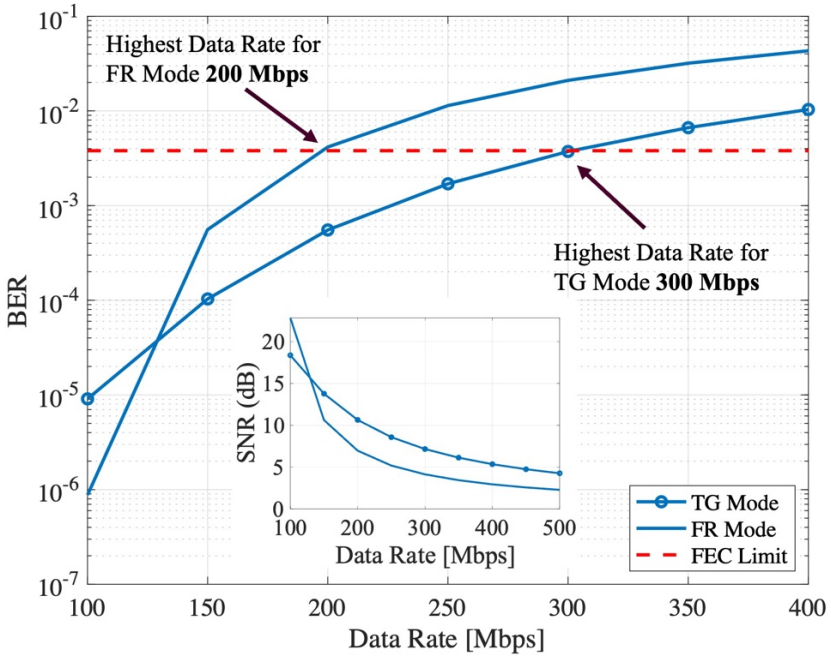

Figure 4-12: BER variation comparisons of the time-gated (TG) mode and the free-running (FR) mode under increased date rate with PR = 20 nW and Pb = 2 nW (64-SPAD array with 10 ns dead time).

This is mainly because the FR mode is more sensitive to background noise as the background noise will not only increase the variance value of the photon count distributions, but also cause serious ISI effect in FR mode. This shows that the TG mode has a stronger tolerance for the background noise power than the FR mode.

The analysis on BER versus data rate Is shown in Figure 4-14 with inserted SNR simulation. In a relative low data rate condition such as 100 Mbps, the FR mode has a lower BER due to the weaker ISI effect since the bit interval T_S is longer, and the FR mode benefits from more effective detection SPAD pixels. The FR mode receiver in this condition has a high mean value in the photon distribution, despite a large variance in the photon count distribution. This is due to the large number of effective SPAD pixels, which enhances the photon detection capability. This conclusion can be obtained from SNR simulation. At a lower data rate, the FR mode receiver has a higher SNR. The ISI effect in the FR mode becomes obvious with the high data rate under a relatively high optical power condition. Therefore, due to the ISI effect, the originally high photon count distribution mean value of FR mode rapidly decreases with the increase of data rate. This led to a rapid decline in both SNR and BER performance. In TG mode, the variance value of photon count distribution is always low because there is no block time, so the performance of SNR and BER will exceed that of FR mode in high data rate condition. In low data rate conditions, the TG mode exhibits inferior performance compared to the FR mode. This is because the TG mode has fewer effective pixels than the FR mode, and the ISI in FR mode is not significant at low data rate conditions. Consequently, in low data rate conditions, TG mode fails to demonstrate its advantages. As shown in Figure 4-14, the FR mode has a higher BER than the TG mode when the data rate is higher than 135 Mbps.

4.3. SPAD Receivers for Pulse-Position Modulation

4.3.1. Concept of PPM Modulation

Pulse Position Modulation (PPM) is a digital communication technique used to transmit digital signals as a sequence of pulses. In PPM, each binary digit (0 or 1) is mapped to one or multiple pulses, and their positions and durations represent the data information [109]. The position of each pulse within discrete time intervals conveys the digital information, while the amplitude of the pulses is typically kept constant. Based on this method, PPM has given a rise of other modulation schemes such as multi-pulse position modulation (MPPM) and differential pulse position modulation (DPPM). MPPM modulation is a method of mapping n-bit binary bit groups to PPM symbols consisting of M information slots according to certain rules [110]. In each MPPM symbol, multiple information slots out of the M slots transmit signal light pulses. DPPM is a modulation method that improves on the single pulse PPM modulation. In DPPM modulation, the high-

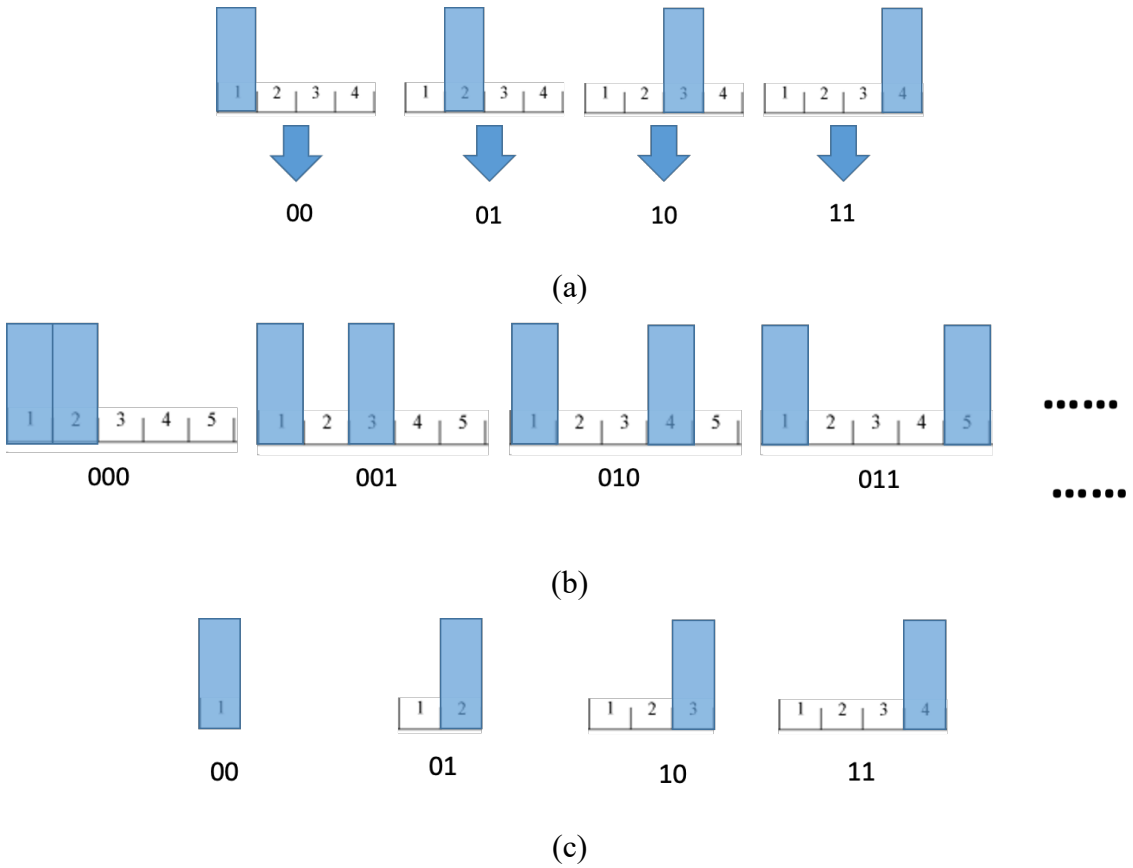

Figure 4-13: The principle diagrams of the (a) basic 4-ary pulse-position modulation (PPM), (b) the multi-pulse position modulation (MPPM) and the (c) differential pulse position modulation (DPPM).

level signals in a code group of the PPM modulation signal are all removed to reduce the required bandwidth [111]. The Figure 4-15 demonstrates the definition of three PPM modulations.

PPM modulation is widely used in optical fiber communication, indoor navigation and other OWC applications [112], [113]. PPM modulation has a strong resistance to optical distortion and dispersion in OWC due to it maps digital information into pulse positions and durations, while the pulse amplitude remains constant. This characteristic enhances the ability of PPM to withstand interference by transmission media. Furthermore, PPM offers simplicity and efficiency in its modulation scheme, making it suitable for high-speed data transmission applications. PPM modulation showcases a unique advantage in its efficient utilization of optical power, allowing multiple bits to be conveyed within a single pulse. This attribute enhances the data rate capacity and spectral efficiency of SPAD-based OWC systems. Additionally, PPM exhibits enhanced resilience to background noise and ambient light, attributes that bolster its performance in challenging environments. On the other hand, PPM suffers from some drawbacks such as low sensitivity and low bandwidth utilization.

In SPAD-based OWC systems, PPM outperforms OOK in scenarios demanding higher data rates and efficient bandwidth usage. However, OOK holds an advantage in low-light conditions, providing a reliable means of communication when signal strength is limited. The choice between PPM and OOK modulation for SPAD-based OWC hinges on specific application requirements, such as data rate, distance, and environmental factors.

4.3.2. OWC Model for PPM Modulation

In SPAD-based OWC application, the PPM modulation distinguishes signal by the counted photons number of SPAD receiver. In this research, the OWC model is established by the basic PPM modulation as shown in the Figure 4-15, the numbers of counted photons in 4 slots are compared and the slot with the maximum counted photons is regarded as the signal pulse. As two digital modulations, the OOK and PPM represent signal information

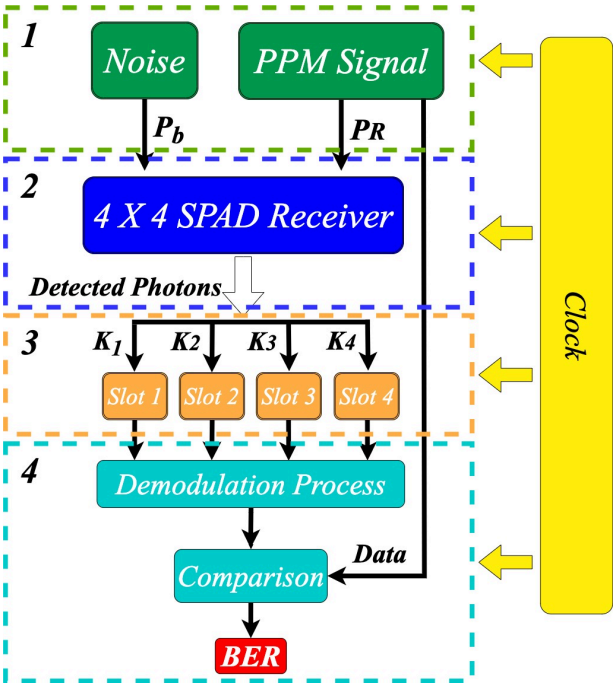

Figure 4-14: The schematic of the SPAD-based OWC model with the basic pulse-position modulation.

by mapping the bits '1' and '0' into different pulse forms. The equations to describe OOK modulation process can be implemented into the PPM modulations.

The Figure 4-15 and the related Table 4-1 show the OWC model processes for PPM modulation. In step 1, the SPAD receiver accepts optical power and background power in pulsed slots and only accepts background power in non-pulsed slots. The photon detection probability distribution in the second step is the same as the analysis in OOK modulation. This is because the 'slot' in PPM modulation and the 'interval' in OOK modulation both have the fixed duration and the SPAD receiver has a response under fixed optical power (the optical power does not change in one slot or one bit interval). In this step, the T_S represents the slot time, and the other parameters keep same to the model for OOK modulation. Unlike the OOK model where we use SNR to estimate the BER, in the PPM model, we obtain the BER in a more intuitive way. We utilize the photon detection probability distribution obtained in step 2, and randomly generate a value k based on this distribution, which represents the number of photons detected by the SPAD receiver in this slot. As basic 4-ary PPM modulation, the 4 k values are compared in step 4 and the

Table 4-1: The summary of equations in the SPAD-based OWC model

Step	Equations	Description
1	Pulsed slot '$P_O = P_b + P_R$' Non-pulsed '$P_O = P_b$'	Photon incident condition
2	$p_K(k) = \begin{cases} \sum_{i=0}^{k} \psi(i,\lambda_k) - \sum_{i=0}^{k-1} \psi(i,\lambda_{k-1}) & k < k_{max} \\ 1 - \sum_{i=0}^{k-1} \psi(i,\lambda_{k-1}) & k = k_{max} \\ 0 & k > k_{max} \end{cases}$ $L = \frac{PDE \times P_O}{Nhf_0}$ $k_{max} = \left\lfloor \frac{T_s - T_b}{T_d} \right\rfloor + 1$ $\psi(i,\lambda) = \lambda^i e^{-\lambda}/i!$ $\lambda_k = L(T_S - T_b - kT_d)$ $T_b = \max\{T_d - (0,1) \times [T_s - (k-1)T_d],\ 0\}$	The analysis of photon detection probability distribution (ISI effect is included)
3	$k = Rand[P_k(k)]$	A random number of detected photons based on the probability distribution in step 2.
4	$k_1 = max\{k_1, k_2, k_3, k_4\}$ $Data = 00;$ $k_2 = max\{k_1, k_2, k_3, k_4\}$ $Data = 01;$ $k_3 = max\{k_1, k_2, k_3, k_4\}$ $Data = 10;$ $k_4 = max\{k_1, k_2, k_3, k_4\}$ $Data = 11;$	Numbers of detected photons in four slots are compared to demodulate the PPM data

corresponding binary data is obtained. The BER can be calculated by comparing the obtained data and original data.

In PPM modulation, a pulsed slot corresponds to two bits. Compared to OOK modulation, that maps the digital information to the presence or absence of pulses, the

SPAD receiver receives lower optical power in PPM-based OWC system. This characteristic leads a lower ISI effect and increase the potential of SPAD receiver in PPM-based system to achieve better performance.

4.3.3. Clock-driven Mode SPAD Receiver for PPM Modulation

In this section, the CD mode and FR mode SPAD receivers are compared based on the OWC model in Section 4.3.2. The SPAD receiver in this model is set to 16 for keeping consistent with our designed SPAD receiver, and 10^6 binary bits are simulated for accurate BER values. The Figure 4-17 and Figure 4-18 demonstrate the BER variances with the increasing received signal powers under different background powers and the BER performances under different data rates, respectively. Similar to the OOK modulation, we can summarize four observations from Figure 4-17. Firstly, the BER of both CD mode and FR mode decreases with an increase in signal power P_R and increases with an increase in background power P_b, which is consistent with the basic principles of optical receivers. Secondly, CD mode outperforms FR mode under any optical power condition, as CD mode

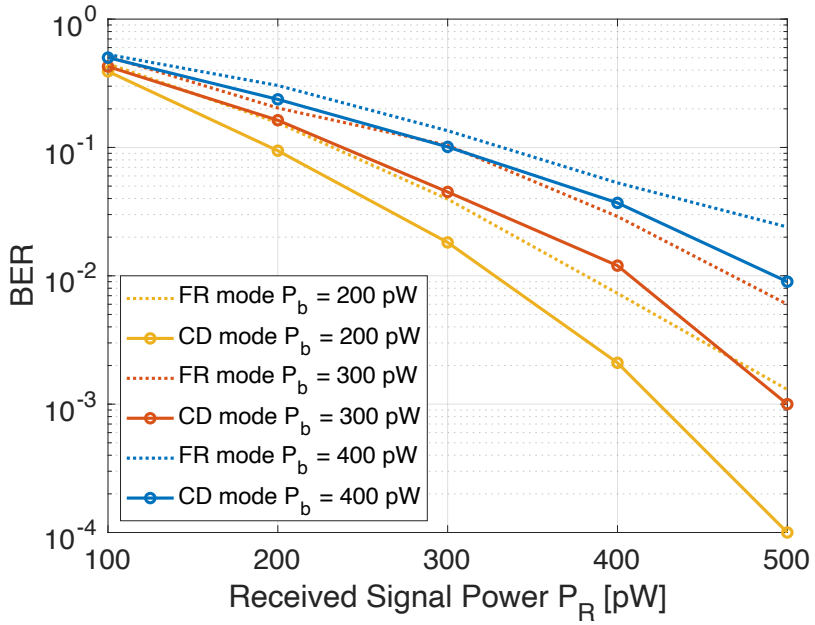

Figure 4-15: BER comparisons of the clock-driven (CD) mode and free-running (FR) mode under variant received signal power and background power with TS = 25 ns (16-SPAD array with 10 ns dead time).

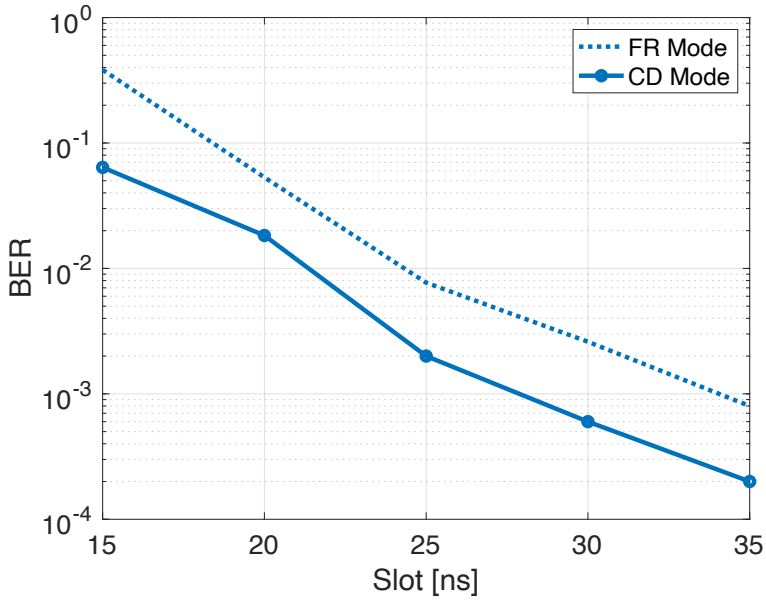

Figure 4-16: BER comparisons of the clock-driven (CD) mode and free-running (FR) mode under variant data rate with PR = 400 pW and Pb = 200 pW (16-SPAD array with 10 ns dead time).

effectively reduces the ISI effect. Thirdly, as P_R increases, the BER gap between CD mode and FR mode becomes larger, as the ISI effect has a greater impact on FR mode but not on CD mode under high optical power. Fourthly, the performance gap between CD mode and FR mode decreases with an increase in P_b, as under high P_b conditions, error bits primarily originate from background noise interference rather than a reduction in effective photon detection time due to the ISI effect. In Figure 4-18, as the slot time T_S increases, both FR and CD modes exhibit a decreasing trend in BER, as their effective photon detection time increases. The better performance of CD mode is attributed to its suppression of the ISI effect. Moreover, the BER difference between FR and CD modes does not show a significant variation with the change in T_S. This can be explained by the fact that the ISI effect does not affect PPM modulation as severely as it does for OOK modulation, and the reasons for this are explained in Section 4.3.2.

4.4. Conclusions

Based on the three SPAD circuit configurations proposed in Chapter 3 (FR, CD, TG), this chapter establishes an OWC model based on Geiger-mode photon counters to simulate the performance of these SPAD circuits in OWC applications. An OWC model with a receiver consisting of a 64-SPAD array is constructed, and a comparison is made between the FR SPAD mode, CD SPAD mode, and TG mode under OOK modulation. Furthermore, an OWC model with a receiver consisting of a 16-SPAD array is also developed to compare the performance of FR SPAD mode and CD SPAD mode under PPM modulation.

In the OWC models based on OOK and PPM modulation, the ISI effect is taken into account, and Monte Carlo simulations are employed to analyze the relationship between the optical intensity, SPAD circuit dead time, communication data rate, and ISI effect in the OWC system. The results indicate a direct proportionality between optical intensity and the block time that responsible for causing ISI effect. Moreover, there is a positive correlation between the ratio of dead time to the bit interval and the ratio of block time to the bit interval.

In this chapter, we also analyzed the photon counting probability distribution of different SPAD circuits. This analysis explores the photon detection scenarios of SPAD receivers under specific time and optical conditions. The mean and variance values of the distribution can be employed to indicate the performance of the SPAD receiver. In comparison to the FR mode, the photon counting probability distribution of CD mode exhibits a smaller mean value, signifying enhanced photon detection capability. On the other hand, the TG mode demonstrates a lower variance value, affirming the stability of its detection capability under high data rate and optical power conditions. These observations collectively provide evidence of the superior performance exhibited by the time-controlled modes.

In this chapter, BER comparisons of the performance of SPAD receivers based on the two OWC models are presented, with a summary of the outcomes provided in Table 4-2. The FR mode has a simpler circuit structure as no signal generation circuit is required. However, a notable disadvantage of FR mode is the high ISI effect that occurs in high

optical power and high data rate conditions, as indicated by the results of the communication model used in this paper. CD mode receiver demonstrates high photon counting ability and effective suppression of background noise. However, the variable dead time in CD mode introduces uncertainty in afterpulsing impact, resulting in a higher noise level in high data rate communication and potentially affecting system performance. The TG mode offers high effective detection time and low afterpulsing probability even under high data rate conditions. However, the TG receiver may suffer from low photon counting ability in low optical power conditions due to fewer effective SPAD pixels. Hence, high data rate and high optical power are necessary conditions to fully exploit the advantages of the TG mode.

Table 4-2: THE COMPARISONS OF THREE RECEIVER MODES

	FR mode	CD mode	TG mode
Advantages	1. Simple circuit structure.	1. High photon counting ability. 2. Effective suppression of background noise.	1. High effective detection time 2. low AP impact. 3. Effective suppression of background noise.
Disadvantages	1. High ISI effect in high optical power condition and high data rate condition.	1. Hight potential AP impact.	1. Low photon counting ability.
Application Scenarios	High data rate and low optical power condition	Low data rate condition.	High data rate and high optical power condition.

Chapter 5

Measurement Results of SPAD Receivers

In this chapter, the chip measurement results are presented for the SPAD circuits proposed in chapter 3, and the characteristics of FR mode, the CD mode and the TG mode in Chapter 4 are verified. The designed SPAD receiver is fabricated in the TSMC 65 nm process, and the printed circuit board (PCB) is manufactured for chip test.

5.1. Fabricated Chip and Printed Circuit Board

For measuring the chip functions and modes of operation, a chip with total area of 2 mm × 1 mm was bonded to a 68-pin PGA package and fixed in a PCB. As shown in the Figure 5-1, 37 pins are reserved for this chip, 8 pins for the outputs of CD SPAD array and 8 pins for the outputs of TG SPAD array, 4 pins are connected with the outputs of 4 SPAD pixels for measuring the performance of single SPAD pixels, and other pins are used to connect the power supplies and digital control the modes of the SPAD receivers. In the PCB design, the SubMiniature version A (SMA) connectors, the switches, the head connectors, the jumpers, and the power connectors are designed as the I/O pins to build connection between chip and outside power, clocks, and experimental devices (power supplies, signal generators, oscilloscope).

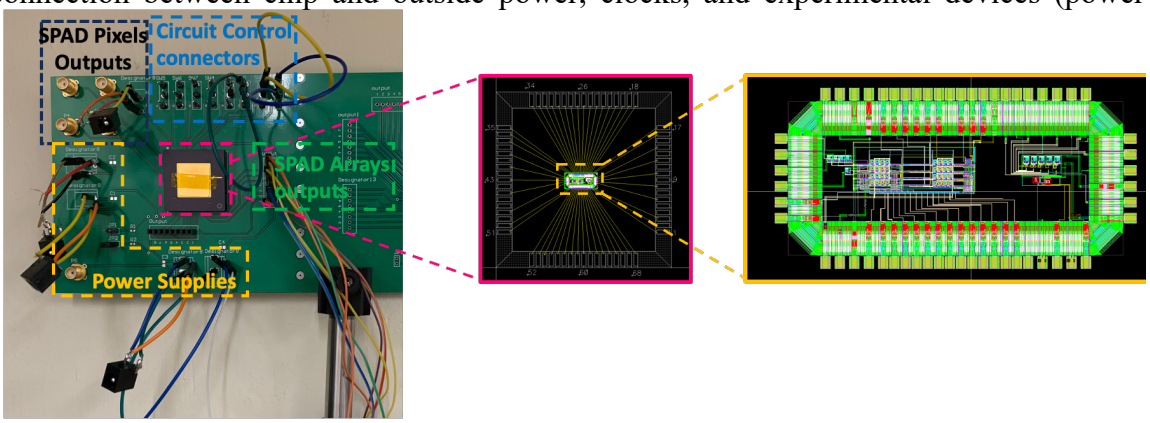

Figure 5-1: Diagram of the experimental setup of the OWC test platform.

5.2. SPAD Performance Parameters Measurement

5.2.1. Dark Count Rate

As a basic parameter in SPAD that deeply impacts the performance of SPAD receiver in OWC application, the DCR is measured by the setup shown in the Figure 5-2. The bias voltage and the SPAD circuits are supplied by an Agilent E3646A DC power supply, the

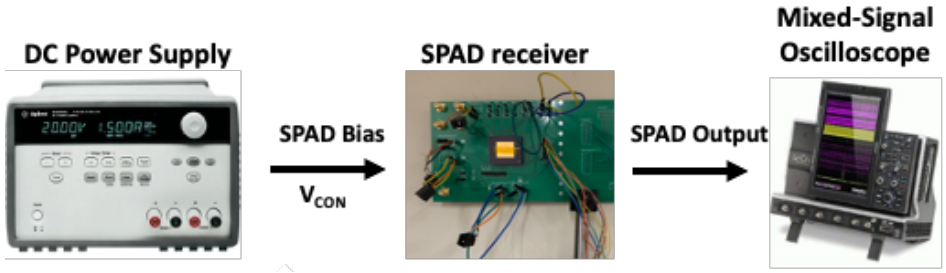

Figure 5-2: Diagram of the experimental setup for the dark count rate (DCR) measurement.

output of SPAD pixel is measured by the LeCroy Waverunner 625Zi mixed-signal oscilloscope. The SPAD receiver is covered by a sheet metal and measured in the dark room to ensure the results are accurate. The SPAD was configured in the basic FR mode, with the control voltage V_{CON} set to be 0 V to achieve the lowest dead time. The DCR values were obtained by averaging the time interval between two dark counts. Each DCR value was calculated from at least 10^5 dark count measurements to ensure its accuracy.

Figure 5-3 shows the DCR results variation with the increased bias voltages. Based on our previous measurement, the breakdown voltage of SPAD is 9.85 V in room temperature, and the DCR keeps increase from 5.9×10^3 in 10.15 V V_{bias} to 5.8×10^4 in 10.55 V V_{bias} and shows an increase with the increase of bias voltage. This is because, high electric field across the SPAD junction increase the likelihood of avalanches from noise source and increases the probability of avalanche triggered by non-photon carriers. Compared with

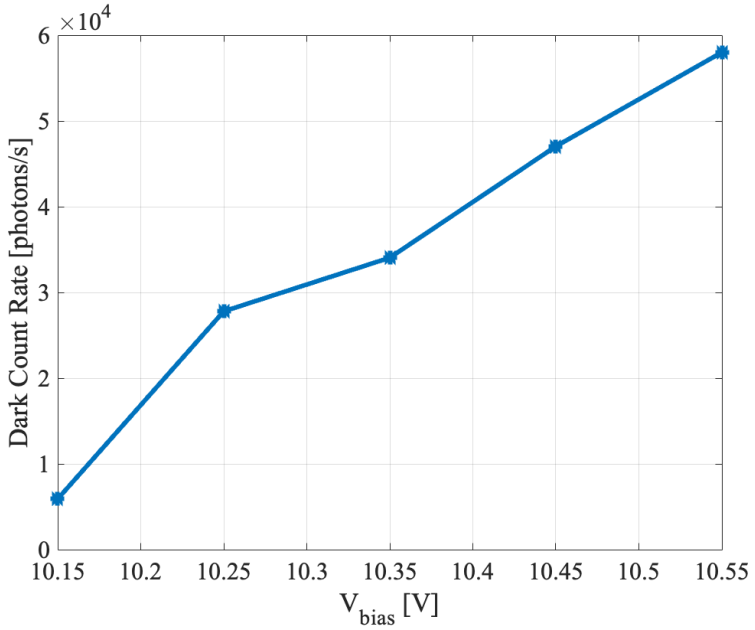

Figure 5-3: The dark count rate (DCR) of proposed SPAD receiver under different bias voltages.

other published SPADs research, the SPAD we designed has a low level of DCR, as shown in the Table 5-1.

Table 5-1: Dark count rate (DCR) comparison of our work and other SPAD circuits

Ref.	Tech. (nm)	VER/VBR (V/V)	DCR (cps)
[114]	180 nm CMOS	0.5/10.2	6×10^4
[88]	180 nm CMOS	2 / 9.98	6.6×10^5
[115]	180 nm CMOS	2.5 / 10	2×10^5
[116]	90 nm CMOS	0.13 / 10.4	1.6×10^4
[117]	65 nm CMOS	1.5 / 9.9	1.1×10^6
This Work	**65 nm CMOS**	**0.3 / 9.85**	$\mathbf{5.9 \times 10^3}$

5.2.2. Adjustable Dead Time Measurement

The dead time of SPAD significantly affects its photon count rate. As described in the Chapter 3.1.2, In our proposed SPAD circuit, the hold-off time of SPAD is controlled by the V_{CON}, the hold-off time increases with the increase of the control voltage through the hold-off time control circuit. This variation can be observed by measuring the output of the

SPAD pixel. It is because, in the proposed front-end circuit, the hold-off time determines the dead time, and the output pulse of SPAD pixel is designed to be consistent with the dead time pulse. The setup of the output measurement is shown in Figure 5-5 and the V_{CON} is set from 0.2 V to 1 V as shown in the Figure 5-4 and Figure 5-6. In Figure 5-4 (a), we measured the waveforms of the SPAD outputs and inserted a complete waveform of SPAD output at 0.2 V control voltage in the top left corner of the image. To reduce device interference, we selectively captured the first appearing positive pulse and integrated the waveforms of outputs at different control voltages into the same figure. It is evident that as the control voltage increases, both the pulse amplitude and width continuously increase, which represents the normal functions from hold-off time control circuit and the output stage in the SPAD front-end circuit. We estimated the duration of the output, by measuring the 50% pulse width of the pulses and the results with the increase of V_{CON} is presented in the Figure 5-4 (b). With the increase of V_{CON}, the pulse width of SPAD output follows in a increase trend. When V_{CON} = 0.2 V, the width of the pulse is approximately 5 ns, whereas when V_{CON} = 1 V, the width of the pulse is approximately 13 ns. With the increase of V_{CON}, the waveform curve of the SPAD output changes. This is because the SPAD output is designed as a square wave. At lower V_{CON} values, due to the presence of parasitic

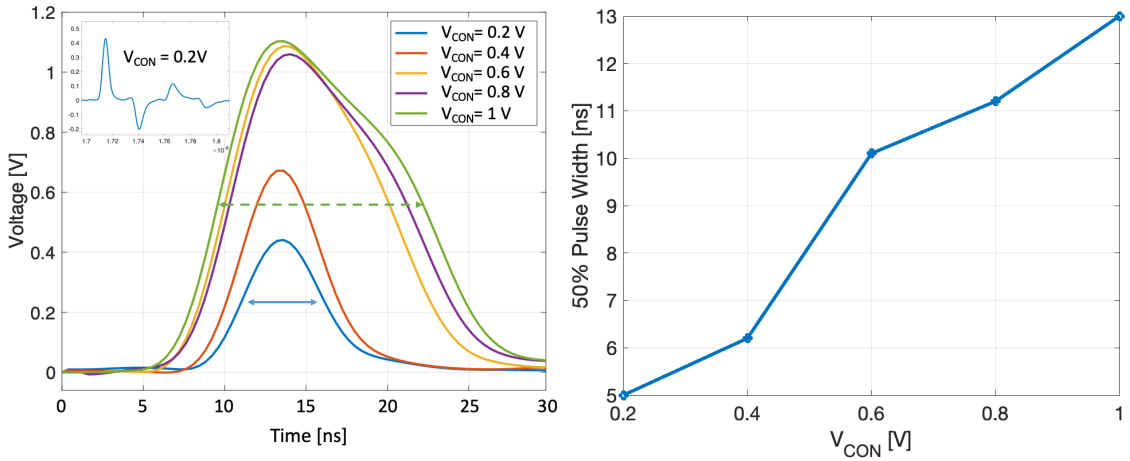

Figure 5-4: (a): The SPAD output waveforms obtained from the oscilloscope; (b): The 50% pulse widths of SPAD outputs with the increase of control voltage (V_{CON}).

capacitance, shorter pulses cannot be fully recorded by the oscilloscope. The increase in pulse width caused by the increasing V_{CON} results in the output waveform exhibiting square wave characteristics on the oscilloscope.

According to the Equation 4-4, the effective photon count rate of a AQR SPAD is proportional to the dead time under a same saturation irradiance condition. As a result, by

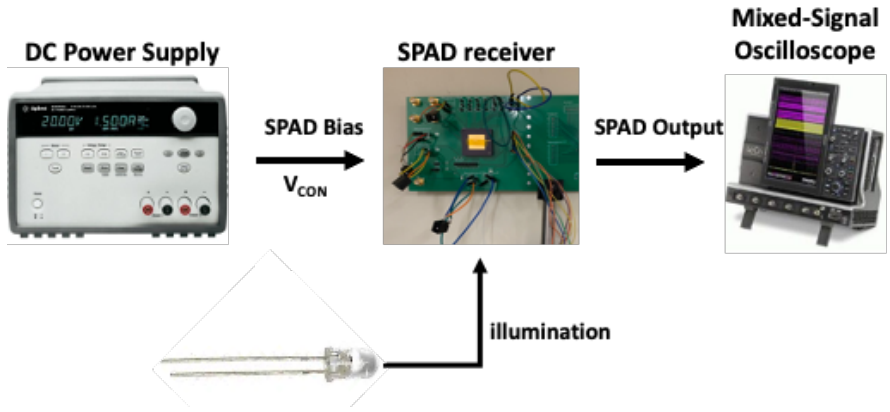

Figure 5-5: Experimental setup for the photon count rate measurement.

adjusting the control voltage, the photon count rate can be measured to demonstrate the effect of dead time. As shown in the setup of Figure 5-5 a LED with 430 nm is added to supply a stable illumination on the SPAD receiver and the photon count rates of a single SPAD pixel under different control voltages are shown in the Figure 5-6 (a). At the same irradiance, the photon counting rate of the SPAD decreases with the increase of the control voltage. This is because, at the same detection time, the higher control voltage leads to an increased dead time, reducing the effective detection time of the SPAD. Compared to a shorter dead time, a longer dead time results in a longer inactive time, reducing the probability of photon detection. Figure 5-6 (b) is a timing diagram illustrating the relationship between detection time and SPAD outputs. From this figure, it can be observed that within a 60 ns detection time, the SPAD outputs under low V_{CON} detected 8 outputs, while the SPAD outputs under high V_{CON} detected three outputs. Consequently, the photon count rate also varies accordingly.

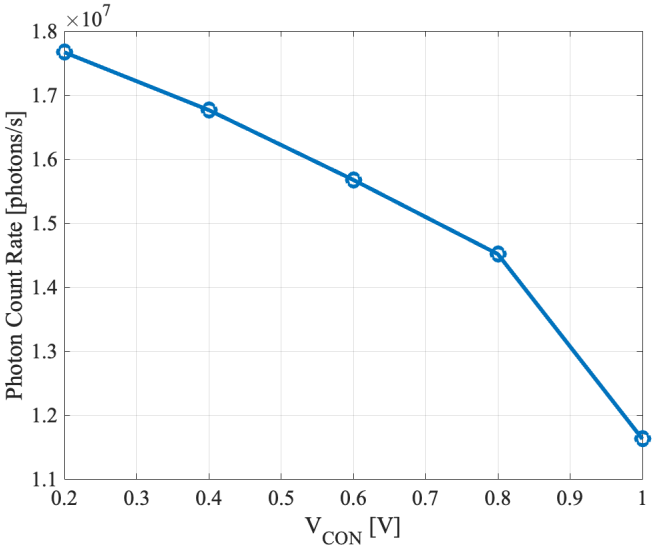

(a)

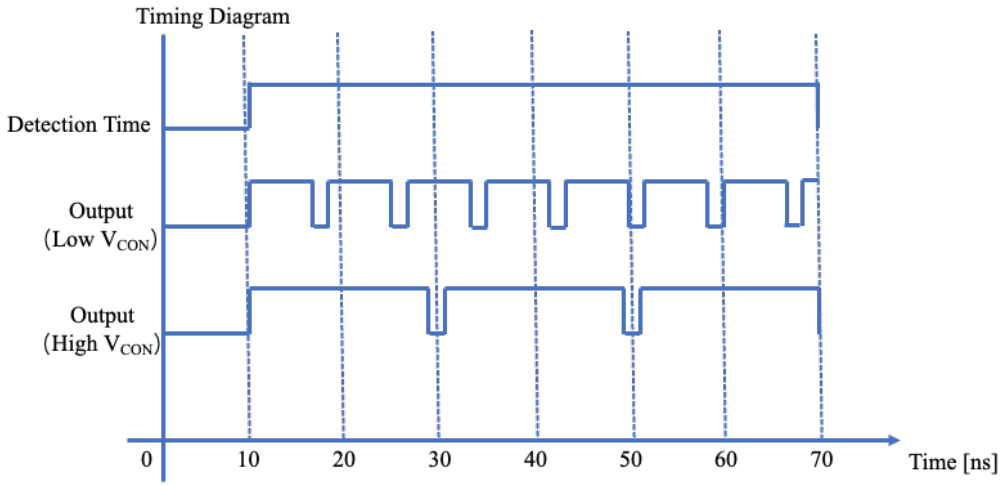

(b)

Figure 5-6: (a): The photon count rate of designed SPAD receiver under different V_{CON}; (b): The timing diagram of the detection time and SPAD outputs.

5.3. The SPAD Receiver Test

5.3.1. The OWC Platform

To evaluate the functionality of the chip and the performance characteristics of the SPAD receiver in different modes, we constructed an OWC platform based on OOK modulation techniques. As shown in Figure 5-7 (a), a function generator (HEWLETT PACKARD 3325B) generates the clock signal, with the frequency set to match the data rate of the OWC system. A Verilog code is programmed into an FPGA evaluation board (Xilinx Spartan VI) to implement signal modulation. The FPGA generates pseudo-random modulation signals at the clock frequency using internally generated pseudo-random numbers. These signals are then sent to an oscilloscope (Lecroy Waverunner 625 Zi) and

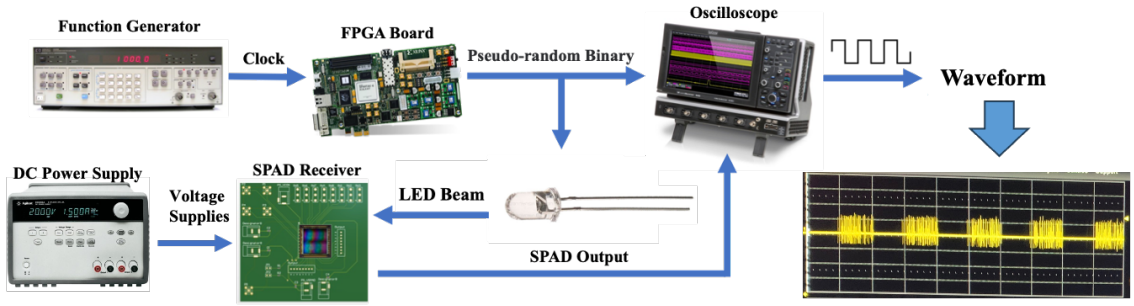

(a)

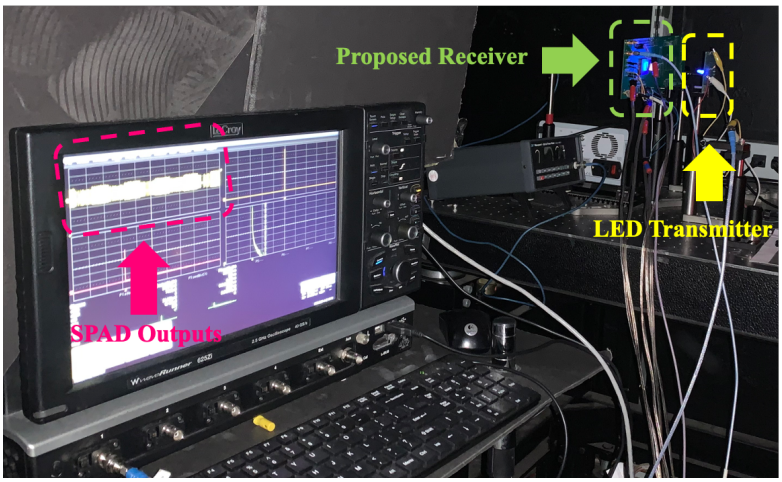

(b)

Figure 5-7: (a) Experimental setup of the OWC platform for the SPAD pixel test and SPAD receiver test. (b) A figure of the proposed OWC platform.

used to drive an LED. Under the control of the pseudo-random signal, the modulated optical signal is continuously transmitted from the LED to the SPAD receiver and detected by the receiver. The SPAD receiver is connected with a DC voltage source (Agilent E3646A), and the outputs of the SPAD pixel or SPAD array are connected to the oscilloscope to be recorded. The waveforms displayed on the oscilloscope allow us to assess the functionality of the chip and the characteristics of different modes. Through this OWC platform, we are able to evaluate the performance and characteristics of the SPAD receiver under different modulation modes, providing valuable insights into the overall functionality and efficiency of the chip. Regarding this platform, the transmitter system is composed of the function generator, the FPGA and the LED, the receiver terminal is the power supply and the SPAD receiver, and the oscilloscope acts as a monitor to record the information from transmitter and receiver systems for further analysis.

The Figure 5-7 (b) is an example to show the setup of chip test measurement, and the screen on the oscilloscope displays the output from one SPAD pixel under a modulated optical signal from the LED transmitter.

5.3.2. The SPAD Receiver Performance

In Section 5.2.2, we experimentally measured the SPAD output pulses to verify the functionality of the voltage-controlled delay in the SPAD front-end circuit. In Section 5.3.1, we proposed a OWC test platform specifically designed to assess the performance of the SPAD receiver. In this subsection, we integrated the SPAD receiver with the OWC test platform to conduct reliability tests on both the SPAD and the receiver.

Figure 5-8 presents a screenshot of an oscilloscope, where the upper part displays the output of the SPAD pixel, and the lower part originates from the FPGA, representing a random OOK signal. Each bit interval in the OOK signal has been labeled to indicate the corresponding bit type (1 or 0). This OOK signal is employed to control the LED, and when the signal is at a high level, the LED is activated, illuminating the SPAD receiver. The photons emitted by the LED are absorbed by the SPAD pixels, resulting in output signals that are shown on the oscilloscope. More photons are detected in signal 1 intervals due to

the signal light from LED. However, few photons can be detected during bit 0 due to the dark counts which is framed in red in Figure 5-8.

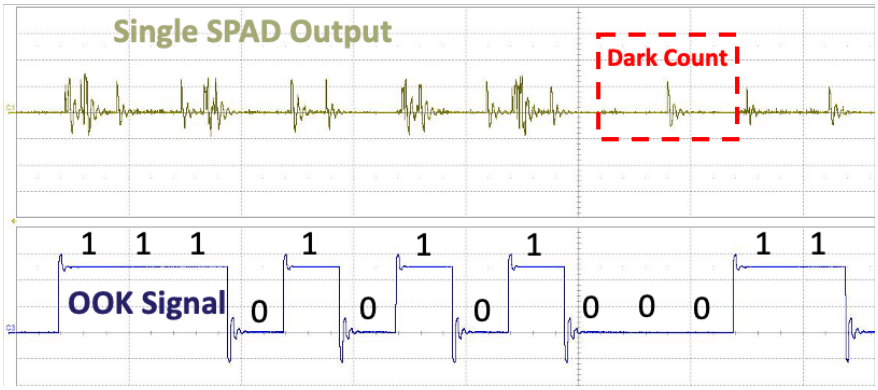

Figure 5-8: The waveforms of SPAD output and the OOK signal obtained from the oscilloscope.

Figure 5-8 illustrates the response of the SPAD as a receiver to the optical signal in the SPAD-based OWC system. Under high optical intensity, the SPAD has a greater likelihood of detecting photons. However, this does not imply that the SPAD under high irradiance will detect more photons than the one under low irradiance within a fixed time interval. This is because photon detection in the SPAD follows a Poisson distribution. In practical optical communication systems, background light causes the SPAD to detect photons even in the absence of signal light (i.e., in bit 0 conditions). When the SPAD detects more photons in bit 0 than in bit 1, errors can occur. Therefore, higher background light intensity leads to the detection of more error bits in the SPAD-based OWC system. Moreover, dark counts also degrade the performance of the SPAD receiver, especially when the signal light is weak. Dark counts reduce the SPAD ability to distinguish between bit 1 and bit 0, thus increasing the BER.

5.3.3. The Experimental Setup

Based on the OWC platform shown as Figure 5-9, a LED pixel is added as the source of the background light. The background light LED (wavelength = 430 nm) is operated by a stable bias voltage and different background optical power could be implemented by adjusting the bias voltage and could be measured by the optical power meter (as shown in the Figure 5-11). The waveforms of signals and outputs from SPAD array are processed in

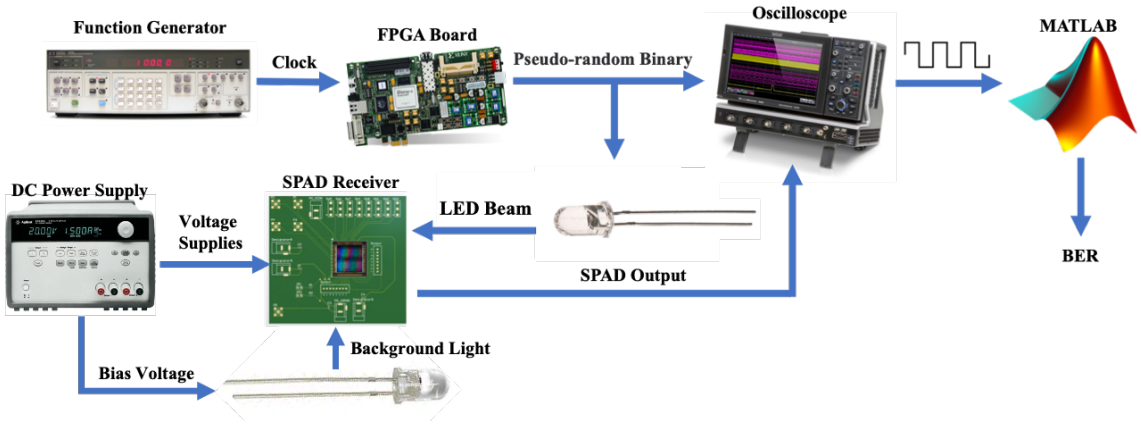

Figure 5-9: The experimental setup for the bit error rate (BER) measurement.

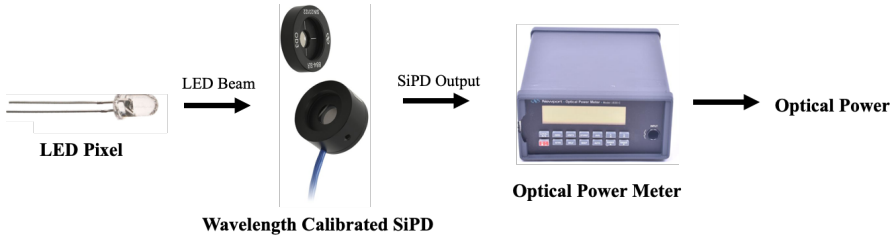

Figure 5-10: The experimental setup for the optical power measurement.

MATLAB for calculating the BER. For the OOK modulation, the clock waveforms are also recorded by the oscilloscope and input into MATLAB. The clock signal acts as the reference signal to regulate the bit interval, and the OOK signal determines the type of this bit interval (bit '1' or bit '0'). The 8-bit output from SPAD array is transferred to hexadecimal number and corresponded to the bit interval. The bit intervals, bit types and the outputs from waveforms are recorded and digitized in MATLAB, and the threshold for OOK modulation is set from 0 to the maximum value of the receiver output. By recording the error bits and correct bits under different thresholds, the threshold is chosen under the condition of minimum error bit and the BER is calculated based on the value of minimum error bit.

Figure 5-10 shows the setup to measure the signal optical powers and background optical powers, the LED illuminates a Newport 818-SL wavelength calibrated silicon photodetector coupled to a Newport 1830-C optical power meter. The two types of optical

powers can be adjusted by adjusting the LED bias voltage and the position to SPAD receiver.

By implementing the OWC platform, Figure 5-11 validates the outputs of the single SPAD pixel and SPAD array with the generation of the OOK signal. Subgraph a shows the clock waveform captured by the oscilloscope, generated by the waveform generator. Subgraph b displays the OOK signal, with each clock period generating one OOK bit. Subgraph c represents the output of the 8-bit SPAD array, and subgraph d depicts the output of an individual SPAD. We can observe that as the OOK signal changes, the output of both the individual SPAD and the SPAD array also changes. When the OOK signal sends bit '1,' the SPAD receives photons from the transmitter, resulting in an output. During the bit '0' interval, when the LED is turned off, the SPAD's output decreases.

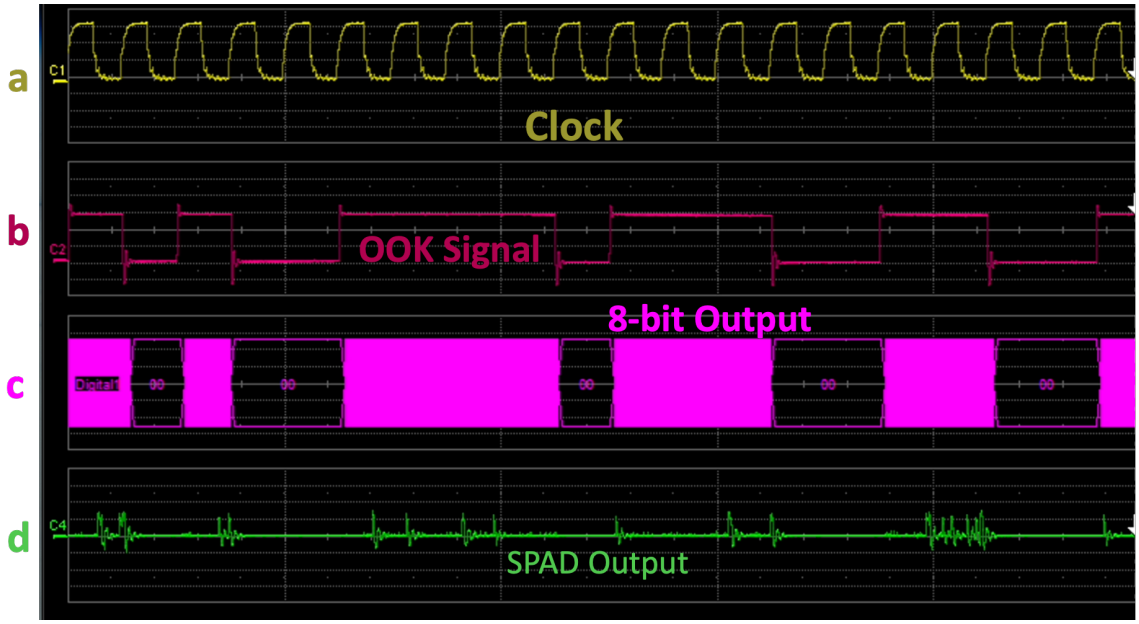

Figure 5-11: The waveforms of the output from SPAD array and the On-Off Keying (OOK) signal obtained from the oscilloscope.

5.4. The BER Measurement

In this part, we measured the BER performance of FR, CD, and TG modes SPAD receivers under increased signal power and increased data rate. The BER performance of FR mode is shown in the Figure 5-12. To better explain the results, the simulation results

run in the same conditions are added to compare with the experimental results. In the simulations and experiments of Figure 5-12, the data rate is set to 2 Mbps and the V_{CON} is set to 0.7 V for 10 ns dead time, the signal powers range from 4 □W to 20 □W with the background power is 1 □W, The incident optical power and incident background power for simulation are calculated by the ratio of active area of SPAD array ($16 \times 25\ \mu m^2$) and the photo detector active area (100.29 mm^2). From Figure 5-12 (a), it can be observed that at the same background power level, with the increasing signal power, the FR mode receiver exhibit a decreasing trend in BER, which is align with the simulation results. This is attributed to the higher signal power allowing the SPAD receiver to detect more photons during the '1' bit duration, resulting in a greater differentiation in the detected photon counts between '1' and '0' bits. As shown in the Equation 4-1 and Equation 4-2, higher received optical power causes a higher photon arrival rate, leading the SPAD has higher probability to detect more photons.

In the Figure 5-12 (b), the experimental results and the simulation results of FR SPAD receiver are compared with increased data rate. In this figure, the signal power is 20 □W and the background power is set to 1 □W. The trend observed in both the experimental and simulation results regarding the BER changing with data rate is consistent, that the increased BER is leaded by the increased data rate. This is explained by the Equation 4-1, the lower detection time for SPAD leads an increased likelihood of detecting less photons and causing a lower performance.

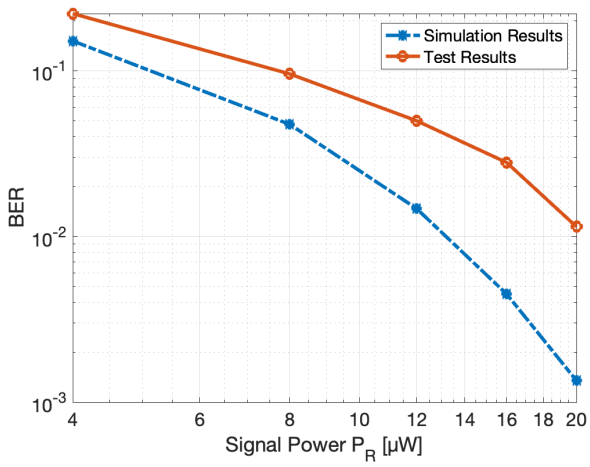

(a)

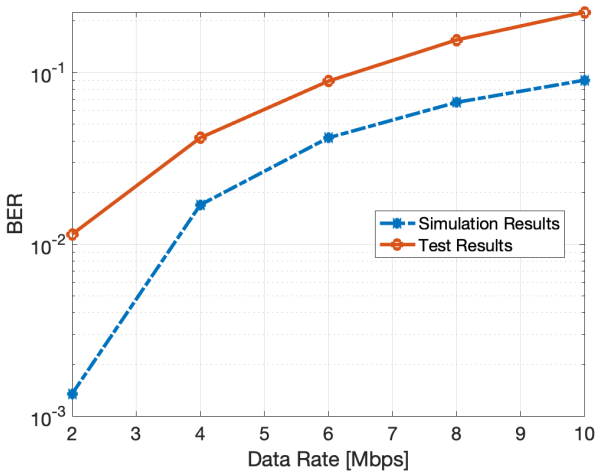

(b)

Figure 5-9: (a) Experimental BER comparisons of free-running (FR) mode under variant signal power and background power with the data rate = 2 Mbps (16-SPAD array with 0.7 V V_{CON} and on-off keying (OOK) modulation); (b) The experimental and simulation BER comparisons of the FR mode under variant data rate with signal power = 20 □W and background power = 1 □W (16-SPAD array with 0.7 V V_{CON} and OOK modulation).

In Figure 5-13, the BER measurement results of CD mode are presented. The communication conditions are consistent with the FR mode BER measurement. We can observe that the experimental results show that the CD mode and the FR mode follow a very close variation trend. The BER results are very similar for both modes. For example, by comparing the experimental results presented in 5-12 (a) with 5-13 (a), when the signal power is 20 μW, the BER of CD is 0.009, while the BER of FR is 0.011. In addition, the simulation results of CD and FR mode show a similar result. This is because, in our experimental setup, the optical powers received by the SPAD receiver are quite low, and the data rate is set to be very low. As a result, the two major factors contributing to block time, optical power, and bit time interval, are extremely limited. As shown in Figure 4-4, ISI effects become prominent only under conditions of high optical power and a high dead time ratio. Therefore, the characteristics of CD mode in reducing ISI effects are not particularly evident at this point, which leads to the similar BER performance between CD mode and FR mode.

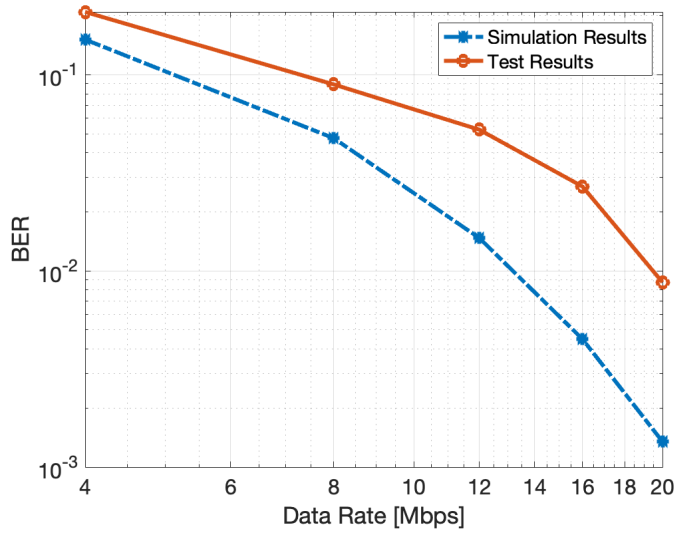

(a)

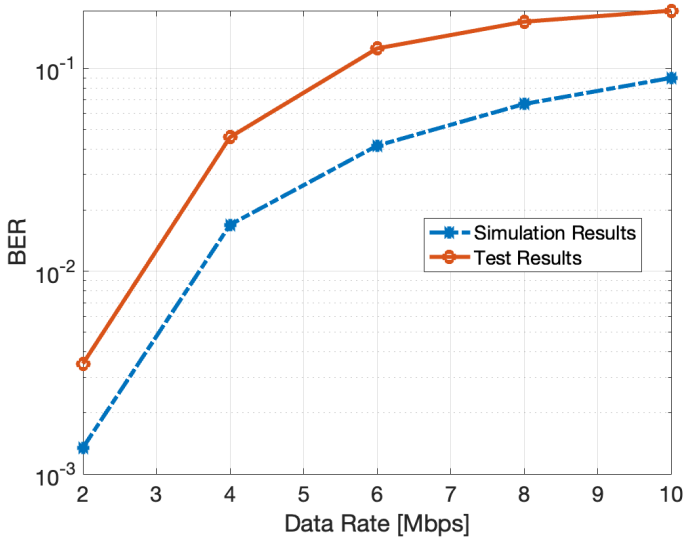

(b)

Figure 5-13: (a) Experimental BER comparisons of the clock-driven (CD) mode under variant signal power and background power with the data rate = 2 Mbps (16-SPAD array with 0.7 V V_{CON} and on-off keying (OOK) modulation; (b) The experimental and simulation BER comparisons of the CD mode under variant data rate with signal power = 20 □W and background power = 1 □W (16-SPAD array with 0.7 V V_{CON} and OOK modulation).

The testing results and the related simulation results of the TG receiver are presented in Figure 5-14 based on OOK modulation. In Figure 5-14 (a), the data rate of the OWC test platform is set to 2 Mbps with the background optical power is 1 μW, in Figure 5-14 (b), the signal power and the background optical power are 20 μW and 1 μW, respectively. Similar to the FR mode and CD mode. As signal power increases, the improvement in

SPAD performance is attributed to the higher signal power brings the higher likelihood of detecting more photons (Figure 5-14 (a)). As the data rate increases, the BER results exhibit a rising trend, which is due to the lower detection time reduces the average counted photons.

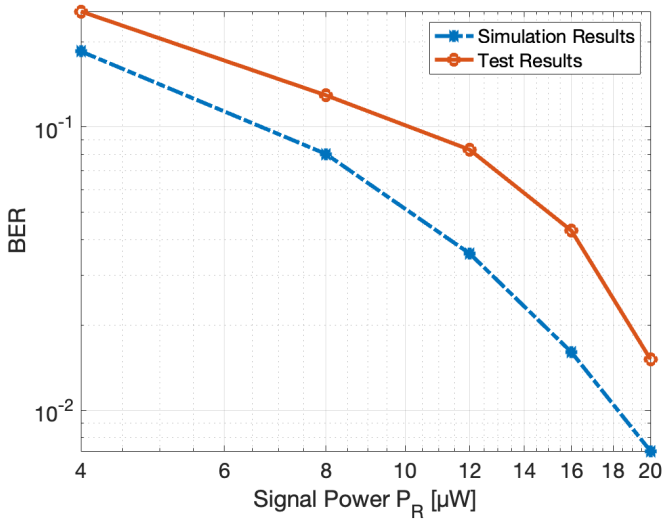

(a)

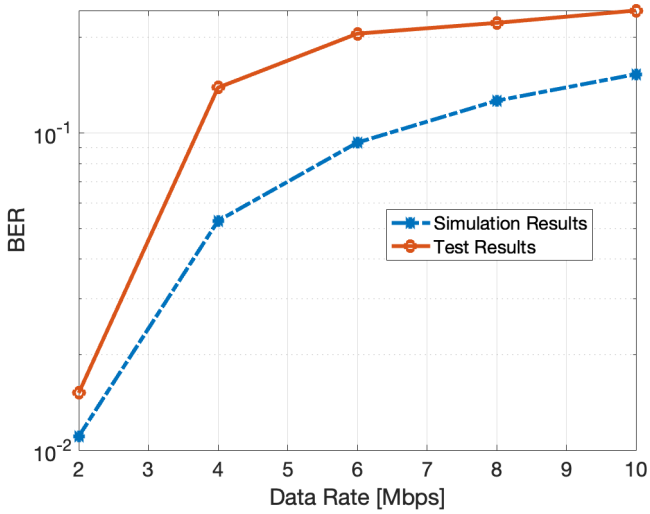

(b)

Figure 5-14: (a) Experimental BER comparisons of the time-gated (TG) mode under variant signal power and background power with the data rate = 2 Mbps (16-SPAD array with 0.7 V V_{CON} and on-off keying (OOK) modulation; (b) The experimental and simulation BER comparisons of the TG mode under variant data rate with signal power = 20 □W and background power = 1 □W (16-SPAD array with 0.7 V V_{CON} and OOK modulation).

By comparing the BER performance of TG mode with FR mode and CD mode under the same communication conditions, it is observed that the BER of TG mode is higher than that of FR mode and CD mode. This is because TG mode can only demonstrate its

advantages under high data rate and high optical power conditions. For instance, as described in Chapter 4.2.3, under high data rate and high optical power conditions, FR mode suffers from severe ISI effects, while TG mode effectively reduces the impact of ISI on receiver performance. In contrast, under low data rate and low optical power conditions, the ISI effect on FR mode is minimal, and TG mode's performance is affected by the fewer effective SPAD pixels caused by the 4-channel detection mode.

By comparing simulation and experimental results, we observed that in FR, CD, and TG modes, the simulation results have a better BER performance compared to the experimental results. This is because in our experiments, our SPAD receiver is affected by DCR and afterpulsing, which are not considered in our SPAD model. Under low optical power conditions, the impact of DCR and AP on the SPAD receiver system's performance is more significant. This is because the low optical power results in a lower number of detected photons by the SPAD, thus increasing the proportion of DCR and AP counts in the overall SPAD counts.

5.5. Conclusions

In this Chapter, a OWC platform is built for measuring the performances and functions of SPAD pixel and SPAD receivers in different modes. The DCRs and photon count rates of single SPAD pixel are measured. The DCR variation shows a function of the V_{bias}, and the output pulse width of the SPAD pixel is observed to have an increased trend with the higher V_{CON}, that shows a correct function of the voltage-controlled hold-off time circuit. The reactions to modulated optical signals from single SPAD pixels and SPAD arrays are tested to show the SPAD pixels and SPAD arrays have an expected response.

Subsequently, we conducted BER tests on FR mode receivers, CD mode receivers, and TG mode receivers under various modulation schemes and communication conditions. Comparing the experimental and simulation results, the trends of BER changing with varying optical power and varying background power are consistent in both simulation and experiments. Discrepancies between certain experimental and simulated data are observed,

primarily due to the presence of variables in the experiments that were not fully captured in the simulations, compounded by the inherent experimental uncertainties.

The experimental results confirm that our designed SPAD receiver functions properly and achieves good performance. By comparing simulation and experimental results, both exhibit consistent trends in BER variation with optical power and data rate changes. To further assess our designed SPAD receiver, we use the model into existing published work and compared the BER performance under the same communication conditions and same SPAD parameters (size and dead time). The performance comparisons with other SPAD-based receivers are presented in the Table 5-2. In the simulation of CD, FR and TG modes, we maintained a background power at 5% of the signal power because this ratio is consistent with the maximum signal power to background power ratio mentioned in Chapter 5.4 and is widely used in the simulation of SPAD-based OWC systems [82]. A figure-of-merit (FoM) is designed with the parameters of data rate, size, signal power and BER. With the varied communication conditions and SPAD parameters, the proposed CD mode always achieve best performance in these comparisons due to its ability on reducing the ISI effect. Compared with other modes, the TG mode simulations exhibit higher BER, which is due to the large SPAD size brings a high photon detection ability in the FR mode and CD mode, however, the TG mode in this condition suffers from the low optical power and low data rate. In large size SPAD array, higher optical power and higher data rate are needed to make the TG mode achieve better performance than the FR mode. In small scale SPAD arrays, as shown in the comparisons with [118], the TG mode has a closer performance for the FR mode, as the data rate and optical powers are high to cause serious ISI effect in the FR mode. In the Table 5-2, through FoM comparisons, our design demonstrates ideal performance, and has a high sensitivity. Only -71 dBm signal power are required to achieve 3.3×10^{-3} BER.

To explore potential future applications, as shown in Table 5-3, we applied the three proposed SPAD modes to higher data rates using simulations. To maintain simulation consistency, we adjusted the background power to 5% of the signal power. The target BER was set to the FEC limit, a metric used to assess the SPAD's ultimate performance. The

Table 5-2: Performance comparison with other SPAD-based receivers

Ref	Array Size	Data Rate	Optical Power	Modulation	Dead Time	BER	FR (Simulation)	CD (Simulation)	TG (Simulation)	FoM
[63]	64 × 64 SPAD	500 Mbps	-46.1 dBm	OOK	12 ns	2×10^{-3}	4.26×10^{-6}	2.12×10^{-6}	1.1×10^{-2}	2.49
[122]	64 × 64 SPAD	100 Mbps	3 nW	OOK	20 ns	2×10^{-3}	1.76×10^{-4}	1.6×10^{-4}	3.6×10^{-2}	4.07
[123]	32 × 32 SPAD	100 Kbps	-64 dBm	PAM	-	10^{-5}	-	-	-	24.53
[34]	5676	2.4 Gbps	-29 dBm	OOK	-	10^{-3}	-	-	-	0.34
[118]	2 × 2 SPAD	100 Mbps	-46.3 dBm	OOK	3.5 ns	2×10^{-3}	1.6×10^{-3}	4.98×10^{-6}	4.9×10^{-2}	533.23
My Work	4 × 4 SPAD	2 Mbps	-71 dBm	OOK	10 ns	3.3×10^{-3}				177.56

A simple figure-of-merit for this SPAD receiver is defined as: FoM = Data Rate [Mbps] / (Array Size × Optical Power [nW] × BER).

Table 5-3: FoM Comparison of three SPAD modes

Mode	Data Rate	Optical Power	BER	FoM
FR	100 Mbps	5.9 nW	3.8×10^{-3}	278.77
CD	100 Mbps	2.85 nW	3.8×10^{-3}	577.1
TG	200 Mbps	20.8 nW	3.8×10^{-3}	158.15

results in terms of Figure-of-Merit (FoM) indicate that the CD mode achieved the highest FoM results. Although the TG mode exhibits the highest data rate, its FoM remains lower than that of the FR mode. This is attributed to the TG mode's requirement for very high optical power to operate the SPAD effectively. In fact, as analyzed in Chapter 4, the high data rate application limits the maximum data rate achievable by the FR mode. Figure 4-13 demonstrates that with increasing signal power, the FR mode experiences greater ISI effects, which restrict its BER performance.

In this work, our attention is focused on the performance comparison between time-controlled modes (CD and TG) and FR mode receivers. As in the experiments to test the BER, we kept the input of background light throughout. Therefore, our BER performance will always be influenced by the background light and cannot reach its minimum value. In addition, due to limitations in experimental conditions and methods, we did not pursue testing at high data rates (the highest data rate was limited to only 10 Mbps). This is also a significant reason for the relatively small performance gap between FR mode and time-controlled modes because SPADs are often not strongly affected by ISI at low data rates. Furthermore, by comparing the area between the optical power meter and the SPAD active area, we estimated that for CD and FR modes, the received signal power in the experiments ranged from 1.6×10^{-11} (signal power = 4 □W) to 8×10^{-11} (signal power = 20 □W). Meanwhile, for the TG mode receiver, the received signal power in the experiments also ranged from 4×10^{-12} (signal power = 1 □W) to 2×10^{-11} (signal power = 20 □W). Consequently, the optical intensity received by the SPAD array in the experiments was extremely limited. This limitation represents a significant factor hindering the proposed SPAD receiver from achieving a low BER.

Chapter 6
Conclusions and Future Work

6.1. Conclusion

In this study, A SPAD receiver with three operation modes for optical wireless communication (OWC) are designed and tested. With the novel SPAD receiver that manufactured in standard CMOS processes, we propose two time-controlled modes to address the limitations of traditional SPAD receivers under conditions of low optical power and high data rate communication. The basic free-running (FR) mode SPAD receiver achieves low dead time with adjustable hold-off time. Based on the FR SPAD receiver, the clock-driven (CD) mode SPAD receiver and the time-gated (TG) SPAD receiver are designed to reduce the intersymbol interference (ISI) effect and improve the performance. To record and calculate the detected optical signal, a data process circuit is designed and composed of 4-bit counters and adder trees. An up-to-date model is built to simulate the designed 3 SPAD operation modes in OWC system, the ISI effect is added to the proposed OWC simulation model and linked with the optical power and communication data rate. To test the SPAD receiver, a OWC test platform is established with a LED transmitter. The BERs of SPAD receiver with 3 operation modes are measured with on-off keying (OOK) modulation. The test results show an expected circuits functions and 3 operation modes characteristics.

In designing the SPAD front-end circuit, a mixed passive-active quench and reset structure is designed for fast quench and reset processes and achieves a minimum dead time of 2.6 ns. Incorporating a voltage-controlled delay and a Schmitt trigger, the circuit gains the capability of adjustable hold-off time and adjustable dead time. This enhancement significantly broadens the potential applications of the SPAD receiver. By adjusting the hold-off time, we can control the photon detection rate and afterpulsing rate of the SPAD, enabling

the proposed SPAD receiver to be applicable in applications that require high photon detection rates, such as OWC, or applications that demand low noise levels, such as medical imaging. By adding two more transistors in different connections, the CD mode and TG mode are introduced to the basic FR mode circuit and operated by the CD signal generation circuit and TG signal generation circuit, respectively. A forcible reset mechanism in the CD mode reset the SPAD at the beginning of every detection interval. In the TG mode receiver, SPAD array is separate to 4 sub-SPAD arrays and realise a continues loop detection.

Four D-flip-flops (DFFs) are connected to count the outputs from single SPAD pixels and the Q terminal of every DFF forms a 4-bit binary outputs of every single SPAD pixel in one detection interval. The 4-bit binary outputs are added by adder tree that composed of full adders. The CD signal which is generated by the CD signal generation circuit is used to connect the reset terminals of every DFF and full adders to reset the data process circuit at the beginning of every bit interval. For a SPAD array, an 8-bit binary output is designed for expressing the detected photons of a SPAD array in every bit interval.

A OWC model for simulating the proposed SPAD modes is presented in this study. The photon detection condition of SPAD can be derived through the Geiger-Muller detector mode, as the SPAD is a type of Geiger-mode photon detector, and the photon incidents follow the Poisson distribution. IThe OWC model calculates the photon count distribution probabilities of SPAD receivers in different communication conditions and derives the BERs. The ISI effect evaluation is added in this model by using the Monte-Carlo simulation, that makes the OWC model is more accurate. The 3 SPAD modes are simulated in the OWC model under different modulations, different signal powers, different background powers and different data rates. The results show that, compared with the FR mode SPAD receiver, the CD mode and the TG mode SPAD receiver improve the performance of the SPAD receiver.

The proposed SPAD receiver is manufactured by the TSMC 65 nm process and tested by the OWC test platform. A printed circuit board is designed to connect the SPAD receiver and the OWC platform for better measuring. The dark count rate (DCR) of the SPAD pixel is measured for verifying the noise level and circuit function. By increasing the control

voltage (V_{CON}), the output pulse width is increased and the photon count rate of the SPAD pixel is decreased due to the dead time increases with the V_{CON}. The outputs of single SPAD pixel and SPAD array under the illumination of modulated optical signal are demonstrated to show the processes of detecting photons and data process.

The proposed SPAD receiver are tested under the modulations of OOK. By analysing the BER test results, the CD mode SPAD receiver performs better in low data rate condition due to the reduction of ISI effect and the TG mode SPAD receiver achieves lower BERs in high data rate high optical power condition, because the continue detection mode reduces both the ISI effect and photon count ability. In the case of the FR mode, it excels particularly under conditions of low optical power and high data rate, thus achieving superior performance. In such circumstances, the TG mode may exhibit suboptimal performance due to its reduced photon detection capability, while the CD mode may encounter elevated errors attributed to a potentially high afterpulsing rate associated with the short bit interval due to high data rate.

6.2. Future Work

Based on the current study, future directions can be categorized into three aspects. First, the SPAD receiver proposed in this research holds potential for broader application in diverse OWC scenarios, such as other communication modulations or different timing control modes. Second, the research for programmable SPAD circuits is promising for advancing SPAD-based OWC applications. Third, the current SPAD-based OWC communication model has primarily considered the fundamental operation of SPAD, neglecting other SPAD parameters such as the DCR and AP. Therefore, a valuable research direction involves incorporating additional parameters into the SPAD communication model to enhance its accuracy and improving its performance.

A. TG Mode Application

In the design of TG mode SPAD receiver, we separate the SPAD array to 4 sub-SPAD arrays and a 4-stage continue detection mode is achieved for reducing the ISI effect. This fixed four-channel mode can restrict the applicability of the TG mode. For instance, at

lower data rates, the TG mode might suffer low performance issues due to a reduced number of effective SPAD pixels. Similarly, at higher data rates, specifically when T_d exceeds four times T_S, the TG mode can be susceptible to ISI effects. From the outset of our design, we recognized this concern and therefore incorporated an adaptive feature. In the complete functionality of our chip, the number of sub-SPAD arrays in the TG mode is not fixed at four; rather, it is adjustable. Through control, the TG mode can be configured into a single-channel mode (FR mode), a two-channel mode, a three-channel mode, or the original four-channel mode. This versatility in TG mode expands its range of applications, allowing for the selection of the optimal TG mode based on conditions such as low data rate and low optical power conditions. This is because reducing the number of channels in the TG mode can enhance the photon detection capability of the SPAD receiver, allowing it to perform better under low-light conditions. Moreover, in low data rate communication, a lower number of channels can help mitigate the ISI effect. Compared to a fixed 4-channel TG mode, this design offers higher photon detection capability, thus improving the performance of the TG mode in low data rate communication. In fact, in larger-scale SPAD arrays, the TG mode could offer even more channel settings to meet diverse OWC requirements. For example, If the minimum value for a channel is four SPADs, then a 16-SPAD array can only support a maximum of 4-channel mode. In this mode, for the SPAD receiver to be unaffected by ISI, the shortest bit interval is approximately equal to one-fourth of the dead time. However, a 64-SPAD array can achieve a 16-channel mode operation. In other words, assuming each SPAD's performance remains constant, for a 64-SPAD array, the shortest bit interval, without being affected by ISI, can be as short as one-sixteenth of the dead time. This represents one of the potential expansion applications for the future, building upon the foundation of this study.

B. Programmable SPAD Circuits

In Section II, we highlighted the interdependence of SPAD parameters in OWC applications. Through circuit control, we can strike a balance between these parameters in various application scenarios to achieve optimal values that maximize the performance of the SPAD receiver. In future research, the emphasis can be placed on the circuit

programmability, enabling the adjustment of SPAD parameters through the design of more versatile control circuits [119]–[121]. For example, in the conditions of high optical power levels, SPADs often achieve high photon detection rates without requiring a very high PDP. Therefore, reducing excess voltage can lower the noise of SPAD while maintaining a high photon detection rate, leading to optimal performance. Consequently, future circuit designs can follow this concept to achieve controllable excess voltage, ensuring it can be adjusted to the optimal value under any optical conditions. In the current design, once V_{HV} is determined, we are unable to adjust the excess voltage through the circuit. In addition, the voltage control circuit for hold-off time is relatively simple. The issue is we cannot accurately control the hold-off time. However, in low data rate communication, we can increase the hold-off time to reduce the afterpulsing rate, thus optimizing the performance of the SPAD receiver. These aspects present opportunities for optimization. In future designs, precise control of excess voltage and dead time through digitized inputs can optimize SPAD performance and broaden the application scenarios for SPAD receivers.

In addition to controlling SPAD parameters, the application of programmable circuits extends further to enhance the functionalities of SPAD receivers. In the design presented in this thesis, the TG mode and CD mode are applied to two separate SPAD arrays and cannot be switched due to different front-end circuits. In future designs, more intricate front-end circuits could be devised to integrate TG mode and CD mode into a single SPAD array, thus saving chip space. Furthermore, aside from these two time-controlled modes, other SPAD operating modes such as Event-driven (ED) mode could also be considered for application in SPAD-based OWC systems.

C. SPAD-based OWC model

The SPAD-based OWC model we are currently using is built upon the Geiger mode photon detector, which leads to certain SPAD parameters not being incorporated into our model, such as DCR and AP. This is also a primary reason for the discrepancies observed between our experimental and simulated results. In future model designs, it is imperative to include these SPAD parameters as input conditions for more accurate outcomes. This is because noise can affect the signal-to-noise ratio (SNR) of the communication system and

reduce the performance of SPAD receivers. For instance, as depicted in the Figure 6-1, while keeping other conditions constant, DCR can significantly influence BER, causing an increase in BER with higher DCR. The various SPAD parameters, as the simulation conditions, are summarized in the Table 6-1.

The depiction in the Figure 6-1 simply illustrates the exponential increase in DCR and the subsequent observation of BER variations. In future model designs, the real challenge lies in establishing interdependencies between different parameters, thereby capturing the

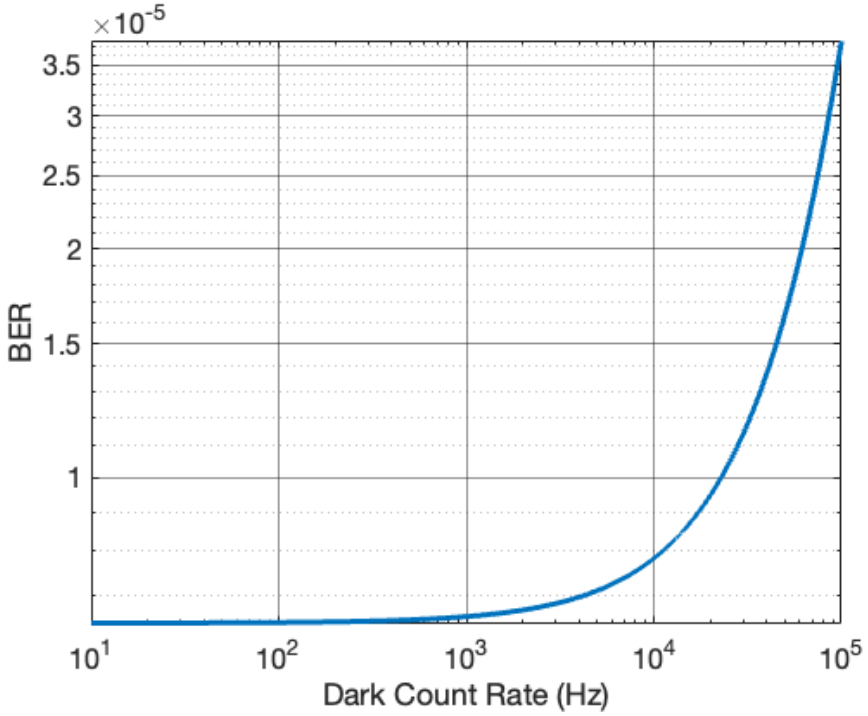

Figure 6-1: The BER variation with the increased dark count rate (DCR) of a SPAD array.

intricate relationships between them within the model. For example, we can establish a relationship between excess voltage, PDP, and DCR using the SPAD model, and apply this relationship to the OWC model, making the model more closely resemble the actual performance of the SPAD receiver.

Table 6-1: Simulation parameters of the Figure 1-6.

Communication Parameters	Values
SPAD Circuit	FR mode
SPAD Number	128

PDP	0.38
Bit Interval	200 ns
Dead Time	150 ns
Signal Optical Power	0.3 nW
Background Optical Power	0.1 nW

References

[1] "Global mobile data traffic 2022 | Statista." Accessed: Jul. 27, 2023. [Online]. Available: https://www.statista.com/statistics/271405/global-mobile-data-traffic-forecast/

[2] Z. Xu and W. Gong, "Enabling ZigBee Backscatter Communication in a Crowded Spectrum," *Proceedings - International Conference on Network Protocols, ICNP*, vol. 2022-October, 2022, doi: 10.1109/ICNP55882.2022.9940384.

[3] Y. Qi and B. Wu, "Radio Frequency Spectrum Control Based on Wideband Jamming and Photonic Jamming Cancellation," *Frontiers in Optics + Laser Science APS/DLS (2019), paper JW3A.65*, p. JW3A.65, Sep. 2019, doi: 10.1364/FIO.2019.JW3A.65.

[4] X. Tan, Z. Sun, J. M. Jornet, and D. Pados, "Increasing indoor spectrum sharing capacity using smart reflect-array," *2016 IEEE International Conference on Communications, ICC 2016*, Jul. 2016, doi: 10.1109/ICC.2016.7510962.

[5] H. Elgala, R. Mesleh, and H. Haas, "Indoor optical wireless communication: Potential and state-of-the-art," *IEEE Communications Magazine*, vol. 49, no. 9, pp. 56–62, Sep. 2011, doi: 10.1109/MCOM.2011.6011734.

[6] "What is OPTICWISE? - OPTICWISE (Optical Wireless Communications – An Emerging Technology)." Accessed: Aug. 09, 2023. [Online]. Available: https://web.archive.org/web/20180105053409/http://opticwise.uop.gr/index.php/aboutopticwise/whatisopticwise.html

[7] "Smart Lighting Engineering Research Center | Boston University." Accessed: Aug. 09, 2023. [Online]. Available: https://www.bu.edu/smartlighting/

[8] M. Jackson, "802.11bb Standard Released for WiFi Style Visible Light LiFi Networks," *ISPreview UK*, Jul. 2023, Accessed: Aug. 09, 2023. [Online]. Available: https://www.ispreview.co.uk/index.php/2023/07/802-11bb-standard-released-for-wifi-style-visible-light-lifi-networks.html

[9] F. E. Goodwin, "A Review of Operational Laser Communication Systems," *Proceedings of the IEEE*, vol. 58, no. 10, pp. 1746–1752, 1970, doi: 10.1109/PROC.1970.7998.

[10] A. R. Ndjiongue, H. C. Ferreira, and T. M. N. Ngatched, "Visible Light Communications (VLC) Technology," *Wiley Encyclopedia of Electrical and Electronics Engineering*, pp. 1–15, Jun. 2015, doi: 10.1002/047134608X.W8267.

[11] L. Flannigan, L. Yoell, and C. Q. Xu, "Mid-wave and long-wave infrared transmitters and detectors for optical satellite communications—a review," *Journal of Optics*, vol. 24, no. 4, p. 043002, Mar. 2022, doi: 10.1088/2040-8986/AC56B6.

[12] T. Kavitha, P. Nagarajan, R. Ganesamoorthy, A. Arulmary, and S. Jana, "Investigating Wireless Optical Communication Systems for İnter Satellite Communication Using QPSK Modulation Technique," pp. 849–856, 2022, doi: 10.1007/978-981-16-6460-1_66.

[13] K. E. Wilson, "An overview of the GOLD experiment between the ETS-6 satellite and the table mountain facility," *The Telecommunications and Data Acquisition Report*, 1996.

[14] M. A. Khalighi and M. Uysal, "Survey on free space optical communication: A communication theory perspective," *IEEE Communications Surveys and Tutorials*, vol. 16, no. 4, pp. 2231–2258, Apr. 2014, doi: 10.1109/COMST.2014.2329501.

[15] A. Palmeiro, M. Martín, I. Crowther, and M. Rhodes, "Underwater radio frequency communications," *OCEANS 2011 IEEE - Spain*, 2011, doi: 10.1109/OCEANS-SPAIN.2011.6003580.

[16] J. Xu and J. Xu, "Underwater wireless optical communication: why, what, and how? [Invited]," *Chinese Optics Letters, Vol. 17, Issue 10, pp. 100007-*, vol. 17, no. 10, pp. 100007-, Oct. 2019, Accessed: Aug. 09, 2023. [Online]. Available: https://opg.optica.org/abstract.cfm?uri=col-17-10-100007

[17] Y. F. Huang, C. T. Tsai, Y. C. Chi, D. W. Huang, and G. R. Lin, "Filtered Multicarrier OFDM Encoding on Blue Laser Diode for 14.8-Gbps Seawater

Transmission," *Journal of Lightwave Technology*, vol. 36, no. 9, pp. 1739–1745, May 2018, doi: 10.1109/JLT.2017.2782840.

[18] S. Li, C. Lu, J. Wang, and Z. Xu, "100 m/500 Mbps underwater optical wireless communication using an NRZ-OOK modulated 520 nm laser diode," *Optics Express, Vol. 27, Issue 9, pp. 12171-12181*, vol. 27, no. 9, pp. 12171–12181, Apr. 2019, doi: 10.1364/OE.27.012171.

[19] H. Chen *et al.*, "Toward Long-Distance Underwater Wireless Optical Communication Based on A High-Sensitivity Single Photon Avalanche Diode," *IEEE Photonics J*, vol. 12, no. 3, Jun. 2020, doi: 10.1109/JPHOT.2020.2985205.

[20] S. Hassan and K. Saeed, "Li-Fi Technology: Data Transmission through Visible Light," *International Journal of Electronics and Communication Engineering*, vol. 11, no. 7, pp. 923–926, Aug. 2017, doi: 10.5281/ZENODO.1132246.

[21] H. Haas, L. Yin, Y. Wang, and C. Chen, "What is LiFi?," *Journal of Lightwave Technology*, vol. 34, no. 6, pp. 1533–1544, Mar. 2016, doi: 10.1109/JLT.2015.2510021.

[22] Y. Wang, D. A. Basnayaka, X. Wu, and H. Haas, "Optimization of Load Balancing in Hybrid LiFi/RF Networks," *IEEE Transactions on Communications*, vol. 65, no. 4, pp. 1708–1720, Apr. 2017, doi: 10.1109/TCOMM.2017.2654249.

[23] H. H. Lu *et al.*, "A 56 Gb/s PAM4 VCSEL-Based LiFi Transmission with Two-Stage Injection-Locked Technique," *IEEE Photonics J*, vol. 9, no. 1, Feb. 2017, doi: 10.1109/JPHOT.2016.2637564.

[24] J. Kosman, O. Almer, A. V. N. Jalajakumari, S. Videv, H. Haas, and R. K. Henderson, "60 Mb/s, 2 meters visible light communications in 1 klx ambient using an unlensed CMOS SPAD receiver," *2016 IEEE Photonics Society Summer Topical Meeting Series, SUM 2016*, pp. 171–172, Aug. 2016, doi: 10.1109/PHOSST.2016.7548773.

[25] M. Notomi, K. Nozaki, A. Shinya, S. Matsuo, and E. Kuramochi, "Toward fJ/bit optical communication in a chip," *Opt Commun*, vol. 314, pp. 3–17, Mar. 2014, doi: 10.1016/J.OPTCOM.2013.09.073.

[26] D. Guckenberger *et al.*, "Chip-to-chip optical interconnects," *Optical Fiber Communication Conference and Exposition and The National Fiber Optic Engineers Conference (2006), paper OFA3*, p. OFA3, Mar. 2006, Accessed: Aug. 08, 2023. [Online]. Available: https://opg.optica.org/abstract.cfm?uri=OFC-2006-OFA3

[27] S. Assefa, F. Xia, and Y. A. Vlasov, "Reinventing germanium avalanche photodetector for nanophotonic on-chip optical interconnects," *Nature 2010 464:7285*, vol. 464, no. 7285, pp. 80–84, 2010, doi: 10.1038/nature08813.

[28] "Intel® Silicon Photonics: How Does It Work? | Intel." Accessed: Aug. 08, 2023. [Online]. Available: https://www.intel.com/content/www/us/en/architecture-and-technology/silicon-photonics/silicon-photonics-overview.html

[29] C. W. Chow, C. H. Yeh, and Y. Liu, "Optical Wireless Communications (OWC) - Technologies and Applications," *25th Opto-Electronics and Communications Conference, OECC 2020*, Oct. 2020, doi: 10.1109/OECC48412.2020.9273663.

[30] D. K. Borah, A. C. Boucouvalas, C. C. Davis, S. Hranilovic, and K. Yiannopoulos, "A review of communication-oriented optical wireless systems," *EURASIP Journal on Wireless Communications and Networking 2012 2012:1*, vol. 2012, no. 1, pp. 1–28, Mar. 2012, doi: 10.1186/1687-1499-2012-91.

[31] M. H. Chang, D. Das, P. V. Varde, and M. Pecht, "Light emitting diodes reliability review," *Microelectronics Reliability*, vol. 52, no. 5, pp. 762–782, May 2012, doi: 10.1016/J.MICROREL.2011.07.063.

[32] H. Zhong, T. Duan, H. Lan, M. Zhou, and F. Gao, "Review of Low-Cost Photoacoustic Sensing and Imaging Based on Laser Diode and Light-Emitting Diode," *Sensors 2018, Vol. 18, Page 2264*, vol. 18, no. 7, p. 2264, Jul. 2018, doi: 10.3390/S18072264.

[33] C. T. Tsai, C. H. Cheng, H. C. Kuo, and G. R. Lin, "Toward high-speed visible laser lighting based optical wireless communications," *Prog Quantum Electron*, vol. 67, p. 100225, Sep. 2019, doi: 10.1016/J.PQUANTELEC.2019.100225.

[34] W. Matthews, Z. Ahmed, W. Ali, and S. Collins, "A 3.45 Gigabits/s SiPM-Based OOK VLC Receiver," *IEEE Photonics Technology Letters*, vol. 33, no. 10, pp. 487–490, May 2021, doi: 10.1109/LPT.2021.3069802.

[35] D. Milovancev, J. Weidenauer, B. Steindl, M. Hofbauer, R. Enne, and H. Zimmermann, "Visible light communication at 50 Mbit/s using a red LED and an SPAD receiver," *2018 11th International Symposium on Communication Systems, Networks and Digital Signal Processing, CSNDSP 2018*, Sep. 2018, doi: 10.1109/CSNDSP.2018.8471890.

[36] Y. wei Ji, G. feng Wu, C. Wang, and E. feng Zhang, "Experimental study of SPAD-based long distance outdoor VLC systems," *Opt Commun*, vol. 424, pp. 7–12, Oct. 2018, doi: 10.1016/J.OPTCOM.2018.04.008.

[37] I. Aggarwal, P. Chawla, R. G.-A. in E. ad, and undefined 2013, "Performance evaluation of intersatellite free space optical communication system with varied parameters and transceiver diversity," *ripublication.comI Aggarwal, P Chawla, R GuptaAdvances in Electronic ad Electric Engineering, 2013•ripublication.com*, vol. 3, no. 7, pp. 847–852, 2013, Accessed: Aug. 08, 2023. [Online]. Available: https://www.ripublication.com/aeee/027%20%20pp%20%20847-852.pdf

[38] S. O. Adebusola, P. A. Owolawi, and J. S. Ojo, "Performance Evaluation of Inter Satellite Optical Wireless Communication Link at Multiple Optical Wavelengths Using Diverse Modulation Techniques," *2020 2nd International Multidisciplinary Information Technology and Engineering Conference, IMITEC 2020*, Nov. 2020, doi: 10.1109/IMITEC50163.2020.9334086.

[39] T. Dong, J. Simões, and Z. Yang, "Flexible Photodetector Based on 2D Materials: Processing, Architectures, and Applications," *Adv Mater Interfaces*, vol. 7, no. 4, p. 1901657, Feb. 2020, doi: 10.1002/ADMI.201901657.

[40] S. Huang *et al.*, "Single-Photon Counting Receivers for 6G Optical Wireless Communications," May 2023, Accessed: May 28, 2023. [Online]. Available: https://arxiv.org/abs/2305.09821v1

[41] R. Hui, "Introduction to fiber-optic communications," 2019, Accessed: May 28, 2023. [Online]. Available: https://books.google.com/books?hl=zh-CN&lr=&id=I7OLDwAAQBAJ&oi=fnd&pg=PP1&dq=Introduction+to+Fiber-Optic+Communications&ots=8YhTikMfYH&sig=A9xIaopIw7UIdizAnQw-fppkhWQ

[42] M. Grundmann, "The Physics of Semiconductors," 2010, doi: 10.1007/978-3-642-13884-3.

[43] K. Brennan, "The physics of semiconductors: with applications to optoelectronic devices," 1999, Accessed: May 28, 2023. [Online]. Available: https://books.google.com/books?hl=zh-CN&lr=&id=6JElXbZpX3IC&oi=fnd&pg=PR11&dq=Brennan+K+F.+The+physics+of+semiconductors:+with+applications+to+optoelectronic+devices%5BM%5D.+Cambridge+university+press,+1999.&ots=aA6v0l7XA8&sig=L96X_GGRp5U_BtPzeBafpF12Prc

[44] X. Wang *et al.*, "Semiconductor ultraviolet photodetectors based on ZnO and MgxZn1−xO," *J Phys D Appl Phys*, vol. 47, no. 28, p. 283001, Jun. 2014, doi: 10.1088/0022-3727/47/28/283001.

[45] P. Aliparast and M. Shaveisi, "Mid-wave infrared optical receiver based on an InAsSb-nBn photodetector using the barrier doping engineering technique for low-power satellite optical wireless communication," *Applied Optics, Vol. 62, Issue 10, pp. 2675-2683*, vol. 62, no. 10, pp. 2675–2683, Apr. 2023, doi: 10.1364/AO.483627.

[46] O. Kharraz and D. Forsyth, "Performance comparisons between PIN and APD photodetectors for use in optical communication systems," *Optik (Stuttg)*, vol. 124, no. 13, pp. 1493–1498, Jul. 2013, doi: 10.1016/J.IJLEO.2012.04.008.

[47] Q. Long, J. Zhang, L. Cao, and W. Wang, "Indoor Visible Light Positioning System Based on Point Classification Using Artificial Intelligence Algorithms," *Sensors 2023, Vol. 23, Page 5224*, vol. 23, no. 11, p. 5224, May 2023, doi: 10.3390/S23115224.

[48] Y. K. Cheong, X. W. Ng, and W. Y. Chung, "Hazardless biomedical sensing data transmission using VLC," *IEEE Sens J*, vol. 13, no. 9, pp. 3347–3348, 2013, doi: 10.1109/JSEN.2013.2274329.

[49] F. Capasso, "Chapter 1 Physics of Avalanche Photodiodes," *Semiconductors and Semimetals*, vol. 22, no. PD, pp. 1–172, Jan. 1985, doi: 10.1016/S0080-8784(08)62952-X.

[50] F. C.-S. and semimetals and undefined 1985, "Physics of avalanche photodiodes," *Elsevier*, Accessed: Jan. 01, 2023. [Online]. Available: https://www.sciencedirect.com/science/article/pii/S008087840862952X

[51] V. Saveliev and V. Golovin, "Silicon avalanche photodiodes on the base of metal-resistor-semiconductor (MRS) structures," *Nucl Instrum Methods Phys Res A*, vol. 442, no. 1–3, pp. 223–229, Mar. 2000, doi: 10.1016/S0168-9002(99)01225-5.

[52] V. Saveliev and V. Golovin, "Silicon avalanche photodiodes on the base of metal-resistor-semiconductor (MRS) structures," *Nucl Instrum Methods Phys Res A*, vol. 442, no. 1–3, pp. 223–229, Mar. 2000, doi: 10.1016/S0168-9002(99)01225-5.

[53] H. W. Ruegg, "An Optimized Avalanche Photodiode," *IEEE Trans Electron Devices*, vol. ED-14, no. 5, pp. 239–251, 1967, doi: 10.1109/T-ED.1967.15937.

[54] M. Tang, Z. Wu, G. Li, T. Miangang, W. Zhigang, and L. Guohui, "CMOS compatible avalanche photodetector and its application in communications," *https://doi.org/10.1117/12.2071179*, vol. 9296, pp. 16–23, Nov. 2014, doi: 10.1117/12.2071179.

[55] M. McClish, R. Farrell, R. Myers, F. Olschner, G. Entine, and K. S. Shah, "Recent advances of planar silicon APD technology," *Nucl Instrum Methods Phys Res A*, vol. 567, no. 1, pp. 36–40, Nov. 2006, doi: 10.1016/J.NIMA.2006.05.055.

[56] P. M. Bloomfield *et al.*, "The design and physical characteristics of a small animal positron emission tomograph," *Phys Med Biol*, vol. 40, no. 6, p. 1105, Jun. 1995, doi: 10.1088/0031-9155/40/6/010.

[57] M. Azadeh, "Fiber Optics Engineering," 2009, doi: 10.1007/978-1-4419-0304-4.

[58] I. I. Izhnin *et al.*, "Single-photon avalanche diode detectors based on group IV materials," *Applied Nanoscience 2021 12:3*, vol. 12, no. 3, pp. 253–263, Feb. 2021, doi: 10.1007/S13204-021-01667-0.

[59] D. Bronzi, F. Villa, S. Tisa, A. Tosi, and F. Zappa, "SPAD Figures of Merit for Photon-Counting, Photon-Timing, and Imaging Applications: A Review," *IEEE Sens J*, vol. 16, no. 1, pp. 3–12, Jan. 2016, doi: 10.1109/JSEN.2015.2483565.

[60] W. Jiang, R. Scott, and M. J. Deen, "High-speed active quench and reset circuit for SPAD in a standard 65 nm CMOS technology," *IEEE Photonics Technology Letters*, vol. 33, no. 24, pp. 1431–1434, Dec. 2021, doi: 10.1109/LPT.2021.3124989.

[61] W. Jiang, Y. Chalich, and M. J. Deen, "Sensors for Positron Emission Tomography Applications," *Sensors 2019, Vol. 19, Page 5019*, vol. 19, no. 22, p. 5019, Nov. 2019, doi: 10.3390/S19225019.

[62] S. Zhu, X. Chen, X. Liu, G. Zhang, and P. Tian, "Recent progress in and perspectives of underwater wireless optical communication," *Prog Quantum Electron*, vol. 73, p. 100274, Sep. 2020, doi: 10.1016/J.PQUANTELEC.2020.100274.

[63] J. Kosman *et al.*, "29.7 A 500Mb/s -46.1dBm CMOS SPAD Receiver for Laser Diode Visible-Light Communications," *Dig Tech Pap IEEE Int Solid State Circuits Conf*, vol. 2019-February, pp. 468–470, Mar. 2019, doi: 10.1109/ISSCC.2019.8662427.

[64] C. Chen, M. Safari, S. Huang, H. Haas, and R. Bian, "5 Gbps optical wireless communication using commercial SPAD array receivers," *Optics Letters, Vol. 47, Issue 9, pp. 2294-2297*, vol. 47, no. 9, pp. 2294–2297, May 2022, doi: 10.1364/OL.454994.

[65] F. Acerbi *et al.*, "Characterization of single-photon time resolution: From single SPAD to silicon photomultiplier," *IEEE Trans Nucl Sci*, vol. 61, no. 5, pp. 2678–2686, Oct. 2014, doi: 10.1109/TNS.2014.2347131.

[66] Y. Xu, P. Xiang, X. Xie, and Y. Huang, "A new modeling and simulation method for important statistical performance prediction of single photon avalanche diode

detectors," *Semicond Sci Technol*, vol. 31, no. 6, p. 065024, May 2016, doi: 10.1088/0268-1242/31/6/065024.

[67] C. L. Forrest Ma, M. J. Deen, L. E. Tarof, and J. C. H. Yu, "Temperature Dependence of Breakdown Voltages in Separate Absorption, Grading, Charge, and Multiplication InP/InGaAs Avalanche Photodiodes," *IEEE Trans Electron Devices*, vol. 42, no. 5, pp. 810–818, 1995, doi: 10.1109/16.381974.

[68] C. Veerappan and E. Charbon, "A low dark count p-i-n diode based SPAD in CMOS technology," *IEEE Trans Electron Devices*, vol. 63, no. 1, pp. 65–71, Jan. 2016, doi: 10.1109/TED.2015.2475355.

[69] H. Finkelstein, M. J. Hsu, S. Zlatanovic, and S. Esener, "Performance trade-offs in single-photon avalanche diode miniaturization," *Review of Scientific Instruments*, vol. 78, no. 10, p. 103103, Oct. 2007, doi: 10.1063/1.2796146/354546.

[70] J. A. Richardson, L. A. Grant, and R. K. Henderson, "Low dark count single-photon avalanche diode structure compatible with standard nanometer scale CMOS technology," *IEEE Photonics Technology Letters*, vol. 21, no. 14, pp. 1020–1022, Jul. 2009, doi: 10.1109/LPT.2009.2022059.

[71] C. Accarino *et al.*, "Low Noise and High Photodetection Probability SPAD in 180 nm Standard CMOS Technology," *Proceedings - IEEE International Symposium on Circuits and Systems*, vol. 2018-May, Apr. 2018, doi: 10.1109/ISCAS.2018.8351173.

[72] R. H. Haitz and R. H. Haitzt, "Mechanisms Contributing to the Noise Pulse Rate of Avalanche Diodes," *J Appl Phys*, vol. 36, no. 10, pp. 3123–3131, Oct. 1965, doi: 10.1063/1.1702936.

[73] M. A. Itzler, X. Jiang, and M. Entwistle, "Power law temporal dependence of InGaAs/InP SPAD afterpulsing," *https://doi.org/10.1080/09500340.2012.698659*, vol. 59, no. 17, pp. 1472–1480, 2012, doi: 10.1080/09500340.2012.698659.

[74] R. K. Henderson *et al.*, "5.7 A 256×256 40nm/90nm CMOS 3D-Stacked 120dB Dynamic-Range Reconfigurable Time-Resolved SPAD Imager," *Dig Tech Pap*

IEEE Int Solid State Circuits Conf, vol. 2019-February, pp. 106–108, Mar. 2019, doi: 10.1109/ISSCC.2019.8662355.

[75] M. A. Wayne, A. Restelli, J. C. Bienfang, and P. G. Kwiat, "Afterpulse reduction through prompt quenching in silicon reach-through single-photon avalanche diodes," *Journal of Lightwave Technology*, vol. 32, no. 21, pp. 4097–4103, Nov. 2014, doi: 10.1109/JLT.2014.2346736.

[76] W. Jiang and M. J. Deen, "Random Telegraph Signal in n+/p-Well CMOS Single-Photon Avalanche Diodes," *IEEE Trans Electron Devices*, vol. 68, no. 6, pp. 2764–2769, Jun. 2021, doi: 10.1109/TED.2021.3070557.

[77] E. Sarbazi, M. Safari, and H. Haas, "The Impact of Long Dead Time on the Photocount Distribution of SPAD Receivers," *2018 IEEE Global Communications Conference, GLOBECOM 2018 - Proceedings*, 2018, doi: 10.1109/GLOCOM.2018.8647814.

[78] W. Jiang, Y. Chalich, and M. J. Deen, "Sensors for Positron Emission Tomography Applications," *Sensors 2019, Vol. 19, Page 5019*, vol. 19, no. 22, p. 5019, Nov. 2019, doi: 10.3390/S19225019.

[79] C. Veerappan and E. Charbon, "CMOS SPAD Based on Photo-Carrier Diffusion Achieving PDP >40% from 440 to 580 nm at 4 v Excess Bias," *IEEE Photonics Technology Letters*, vol. 27, no. 23, pp. 2445–2448, Dec. 2015, doi: 10.1109/LPT.2015.2468067.

[80] F. Gramuglia *et al.*, "Engineering Breakdown Probability Profile for PDP and DCR Optimization in a SPAD Fabricated in a Standard 55 nm BCD Process," *IEEE Journal of Selected Topics in Quantum Electronics*, vol. 28, no. 2, 2022, doi: 10.1109/JSTQE.2021.3114346.

[81] W. Jiang, R. Scott, and M. J. Deen, "High-speed active quench and reset circuit for SPAD in a standard 65 nm CMOS technology," *IEEE Photonics Technology Letters*, vol. 33, no. 24, pp. 1431–1434, Dec. 2021, doi: 10.1109/LPT.2021.3124989.

[82] J. Liu, W. Jiang, and M. J. Deen, "Time-Gated Circuit for SPAD-based OWC," *2022 IEEE Photonics Conference, IPC 2022 - Proceedings*, 2022, doi: 10.1109/IPC53466.2022.9975721.

[83]. Z Li, M. J. Deen, Q. Fang, and P. R. Selvaganapathy, "Towards a portable Raman spectrometer using a concave grating and a time-gated CMOS SPAD," *Optics Express, Vol. 22, Issue 15, pp. 18736-18747*, vol. 22, no. 15, pp. 18736–18747, Jul. 2014, doi: 10.1364/OE.22.018736.

[84] I. M. Antolovic, S. Burri, C. Bruschini, R. Hoebe, and E. Charbon, "Nonuniformity analysis of a 65-kpixel CMOS SPAD imager," *IEEE Trans Electron Devices*, vol. 63, no. 1, pp. 57–64, Jan. 2016, doi: 10.1109/TED.2015.2458295.

[85] I. M. Antolovic, C. Bruschini, and E. Charbon, "Dynamic range extension for photon counting arrays," *Optics Express, Vol. 26, Issue 17, pp. 22234-22248*, vol. 26, no. 17, pp. 22234–22248, Aug. 2018, doi: 10.1364/OE.26.022234.

[86] E. Sarbazi, M. Safari, and H. Haas, "The Bit Error Performance and Information Transfer Rate of SPAD Array Optical Receivers," *IEEE Transactions on Communications*, vol. 68, no. 9, pp. 5689–5705, Sep. 2020, doi: 10.1109/TCOMM.2020.2993374.

[87] R. Enne, B. Steindl, M. Hofbauer, and H. Zimmermann, "Fast cascoded quenching circuit for decreasing afterpulsing effects in 0.35-µm CMOS," *IEEE Solid State Circuits Lett*, vol. 1, no. 3, pp. 62–65, Mar. 2018, doi: 10.1109/LSSC.2018.2827881.

[88] J. Rhim *et al.*, "Monolithically-Integrated Single-Photon Avalanche Diode in a Zero-Change Standard CMOS Process for Low-Cost and Low-Voltage LiDAR Application," *Instruments 2019, Vol. 3, Page 33*, vol. 3, no. 2, p. 33, Jun. 2019, doi: 10.3390/INSTRUMENTS3020033.

[89] S. Lindner, S. Pellegrini, Y. Henrion, B. Rae, M. Wolf, and E. Charbon, "A High-PDE, Backside-Illuminated SPAD in 65/40-nm 3D IC CMOS Pixel with Cascoded Passive Quenching and Active Recharge," *IEEE Electron Device Letters*, vol. 38, no. 11, pp. 1547–1550, Nov. 2017, doi: 10.1109/LED.2017.2755989.

[90] D. Bronzi, S. Tisa, F. Villa, S. Bellisai, A. Tosi, and F. Zappa, "Fast sensing and quenching of CMOS SPADs for minimal afterpulsing effects," *IEEE Photonics Technology Letters*, vol. 25, no. 8, pp. 776–779, 2013, doi: 10.1109/LPT.2013.2251621.

[91] X. Jiang *et al.*, "Afterpulsing effects in free-running InGaAsP single-photon avalanche diodes," *IEEE J Quantum Electron*, vol. 44, no. 1, pp. 3–11, Jan. 2008, doi: 10.1109/JQE.2007.906996.

[92] N. R. Mahapatra, S. V. Garimella, and A. Tareen, "An empirical and analytical comparison of delay elements and a new delay element design," *Proceedings - IEEE Computer Society Workshop on VLSI 2000: System Design for a System-on-Chip Era, IWV 2000*, pp. 81–86, 2000, doi: 10.1109/IWV.2000.844534.

[93] Z. Wang, "CMOS Adjustable Schmitt Triggers," *IEEE Trans Instrum Meas*, vol. 40, no. 3, pp. 601–605, 1991, doi: 10.1109/19.87026.

[94] I. M. Antolovic, S. Burri, C. Bruschini, R. Hoebe, and E. Charbon, "Nonuniformity analysis of a 65-kpixel CMOS SPAD imager," *IEEE Trans Electron Devices*, vol. 63, no. 1, pp. 57–64, Jan. 2016, doi: 10.1109/TED.2015.2458295.

[95] I. M. Antolovic, C. Bruschini, and E. Charbon, "Dynamic range extension for photon counting arrays," *Optics Express, Vol. 26, Issue 17, pp. 22234-22248*, vol. 26, no. 17, pp. 22234–22248, Aug. 2018, doi: 10.1364/OE.26.022234.

[96] M. Kokkonen and S. Pietilä, "A new bit synchronization method for a GPS receiver," *Record - IEEE PLANS, Position Location and Navigation Symposium*, pp. 85–90, 2002, doi: 10.1109/PLANS.2002.998893.

[97] E. Sarbazi and H. Haas, "Detection statistics and error performance of SPAD-based optical receivers," *IEEE International Symposium on Personal, Indoor and Mobile Radio Communications, PIMRC*, vol. 2015-December, pp. 830–834, Dec. 2015, doi: 10.1109/PIMRC.2015.7343412.

[98] E. Sarbazi, M. Safari, and H. Haas, "Photon detection characteristics and error performance of SPAD array optical receivers," *2015 4th International Workshop on*

Optical Wireless Communications, IWOW 2015, pp. 132–136, Nov. 2015, doi: 10.1109/IWOW.2015.7342281.

[99] S. H. Lee and R. P. Gardner, "A new G–M counter dead time model," *Applied Radiation and Isotopes*, vol. 53, no. 4–5, pp. 731–737, Nov. 2000, doi: 10.1016/S0969-8043(00)00261-X.

[100] E. Sarbazi, M. Safari, and H. Haas, "On the Information Transfer Rate of SPAD Arrays," *IEEE Wireless Communications and Networking Conference, WCNC*, vol. 2020-May, May 2020, doi: 10.1109/WCNC45663.2020.9120696.

[101] E. Sarbazi, M. Safari, and H. Haas, "Statistical Modeling of Single-Photon Avalanche Diode Receivers for Optical Wireless Communications," *IEEE Transactions on Communications*, vol. 66, no. 9, pp. 4043–4058, Sep. 2018, doi: 10.1109/TCOMM.2018.2822815.

[102] S. Huang, S. M. Patanwala, J. Kosman, R. K. Henderson, and M. Safari, "Optimal Photon Counting Receiver for Sub-Dead-Time Signal Transmission," *Journal of Lightwave Technology*, vol. 38, no. 18, pp. 5225–5235, Sep. 2020, doi: 10.1109/JLT.2020.3000723.

[103] W. Jiao, H. Liu, J. Yin, Z. Wei, A. Luo, and D. Deng, "Performance of a QAM/FSO communication system employing spatial diversity in weak and saturation turbulence channels," *https://doi.org/10.1080/09500340.2019.1596321*, vol. 66, no. 9, pp. 965–975, May 2019, doi: 10.1080/09500340.2019.1596321.

[104] L. Zhang *et al.*, "A Comparison of APD- and SPAD-Based Receivers for Visible Light Communications," *Journal of Lightwave Technology*, vol. 36, no. 12, pp. 2435–2442, Jun. 2018, doi: 10.1109/JLT.2018.2811180.

[105] E. Sarbazi, M. Safari, and H. Haas, "The Bit Error Performance and Information Transfer Rate of SPAD Array Optical Receivers," *IEEE Transactions on Communications*, vol. 68, no. 9, pp. 5689–5705, Sep. 2020, doi: 10.1109/TCOMM.2020.2993374.

[106] S. Huang and M. Safari, "Time-Gated Photon Counting Receivers for Optical Wireless Communication," *Journal of Lightwave Technology*, vol. 39, no. 22, pp. 7113–7123, Nov. 2021, doi: 10.1109/JLT.2021.3112828.

[107] E. Sarbazi, M. Safari, and H. Haas, "The Impact of Long Dead Time on the Photocount Distribution of SPAD Receivers," *2018 IEEE Global Communications Conference, GLOBECOM 2018 - Proceedings*, 2018, doi: 10.1109/GLOCOM.2018.8647814.

[108] C.-C. Chen, "Effect of Detector Dead Time on the Performance of Optical Direct-Detection Communication Links." 1988.

[109] D. S. Shiu and J. M. Kahn, "Differential pulse-position modulation for power-efficient optical communication," *IEEE Transactions on Communications*, vol. 47, no. 8, pp. 1201–1210, 1999, doi: 10.1109/26.780456.

[110] A. E. Elfiqi, H. S. Khallaf, S. F. Hegazy, A. Elsonbaty, H. M. H. Shalaby, and S. S. A. Obayya, "Chaotic Polarization-Assisted DPSK-MPPM Modulation for Free-Space Optical Communications," *IEEE Trans Wirel Commun*, vol. 18, no. 9, pp. 4225–4237, Sep. 2019, doi: 10.1109/TWC.2019.2920970.

[111] E. E. Elsayed, D. Kakati, M. Singh, A. Grover, and G. Anand, "Design and analysis of a dense wavelength-division multiplexed integrated PON-FSO system using modified OOK/DPPM modulation schemes over atmospheric turbulences," *Opt Quantum Electron*, vol. 54, no. 11, pp. 1–27, Nov. 2022, doi: 10.1007/S11082-022-04142-4/FIGURES/13.

[112] M. Noshad and M. Brandt-Pearce, "Application of expurgated PPM to indoor visible light communications-Part I: Single-User systems," *Journal of Lightwave Technology*, vol. 32, no. 5, pp. 875–882, Mar. 2014, doi: 10.1109/JLT.2013.2293341.

[113] N. Kumar, "2.50 Gbit/s optical wireless communication system using PPM modulation schemes in HAP-to-satellite links," *Optik (Stuttg)*, vol. 125, no. 14, pp. 3401–3404, Jul. 2014, doi: 10.1016/J.IJLEO.2014.01.047.

[114] N. Faramarzpour, M. J. Deen, S. Shirani, and Q. Fang, "Fully integrated single photon avalanche diode detector in standard CMOS 0.18-μm technology," *IEEE Trans Electron Devices*, vol. 55, no. 3, pp. 760–767, Mar. 2008, doi: 10.1109/TED.2007.914839.

[115] H. Finkelstein, M. J. Hsu, and S. C. Esener, "STI-bounded single-photon avalanche diode in a deep-submicrometer CMOS technology," *IEEE Electron Device Letters*, vol. 27, no. 11, pp. 887–889, Nov. 2006, doi: 10.1109/LED.2006.883560.

[116] H. Finkelstein *et al.*, "A new single-photon avalanche diode in 90nm standard CMOS technology," *Optics Express, Vol. 18, Issue 21, pp. 22158-22166*, vol. 18, no. 21, pp. 22158–22166, Oct. 2010, doi: 10.1364/OE.18.022158.

[117] F. Nolet *et al.*, "Quenching Circuit and SPAD Integrated in CMOS 65 nm with 7.8 ps FWHM Single Photon Timing Resolution," *Instruments 2018, Vol. 2, Page 19*, vol. 2, no. 4, p. 19, Sep. 2018, doi: 10.3390/INSTRUMENTS2040019.

[118] B. Steindl, M. Hofbauer, K. Schneider-Hornstein, P. Brandl, and H. Zimmermann, "Single-Photon Avalanche Photodiode Based Fiber Optic Receiver for Up to 200 Mb/s," *IEEE Journal of Selected Topics in Quantum Electronics*, vol. 24, no. 2, Mar. 2018, doi: 10.1109/JSTQE.2017.2764682.

[119] W. Bogaerts *et al.*, "Programmable photonic circuits," *Nature 2020 586:7828*, vol. 586, no. 7828, pp. 207–216, Oct. 2020, doi: 10.1038/s41586-020-2764-0.

[120] A. Hoynes-O'Connor and T. S. Moon, "Programmable genetic circuits for pathway engineering," *Curr Opin Biotechnol*, vol. 36, pp. 115–121, Dec. 2015, doi: 10.1016/J.COPBIO.2015.08.007.

[121] K. Alsnaie, S. M. A. Ghaly, and M. A. Ali, "Study and Design of a Multi-range Programmable Sensor for Temperature Measurement," *Engineering, Technology & Applied Science Research*, vol. 12, no. 6, pp. 9601–9606, Dec. 2022, doi: 10.48084/ETASR.5284.

Appendix A
PCB Schematic Design

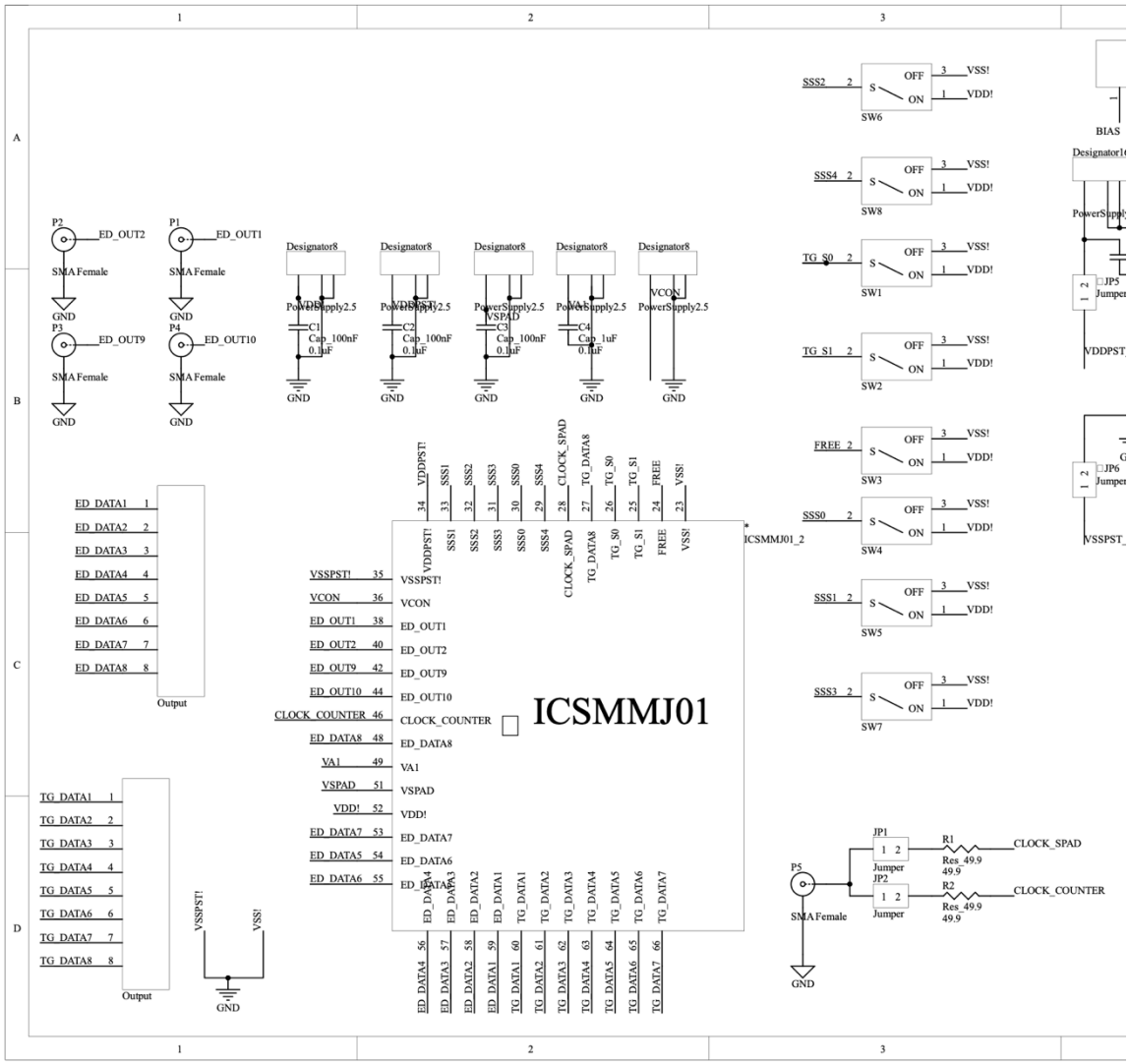

MATLAB Code

OOK Modulation

```
N = ; % number of SPAD Pixel
Td = ; % Dead time value
Ts = ;% bit interval value
PR = ;
Pb = 0;
PDE = ; %

h = ;v =;% constant
BER_Final = [];

for  PR =
%     Ts = 1./(DR.*1024.*1024);

lambda_0 = (PDE.*Pb)./(N.*h.*v);
lambda_1 = (PDE.*(PR+Pb))./(N.*h.*v);
BER_I = inline('(U1-U0)./((sqrt(Sigma1) + sqrt(Sigma0)))','U1','U0','Sigma1','Sigma0');
%%%%%%%%%%%%%%%%%%%%%%%%%%%%%%%%%%%%%%%%%%%%
Sigma_ISI = [];
Mu_ISI = [];
Sigma_ISI1 = [];% summation of total SPAD's variance
Sigma_ISI0 = [];
Mu_ISI1 = [];
Mu_ISI0 = [];
BER_Seg = [];
BER0 = [];
BER1 = [];
Sigma = [];
Mu = [];
%%%%%%%%%%%%%%%%%%%%%%%%%%%%%%%%%%%%%%%
TB0 =[];
Mu_loop1 = [];
Sigma_loop1 = [];
for loop1 = 0:1:1
    if loop1 == 0
        lambda = lambda_0;
    else
        lambda = lambda_1;
    end

Kmax =(floor(Ts./Td) + 1);
lambdak = inline('lambda.*(T-(k.*t))','lambda','T','k','t');
psai = inline('((u.^i).*exp(-u))./factorial(i)','u','i');
y1_m = [];
for k = 0:1:(Kmax - 1)
lambdak1_1 = lambdak(lambda,Ts,k,Td);
y1 = [];
   for i = 0:1:k
     psai1_1 = psai(lambdak1_1,i);
```

```
    for a = 1:length(psai1_1)
        y1 = [y1,psai1_1(a)];
    end
   end
   y1_m = [y1_m,y1];
end
c = sum(y1_m);
Uk = Kmax - c;
y1_s = [];
for k = 0:1:(Kmax - 1)
lambdak1_2 = lambdak(lambda,Ts,k,Td);
y2 = [];
   for i = 0:1:k
     psai1_2 = psai(lambdak1_2,i);
     p = psai1_2.*((2.*Kmax) - (2.*k) - 1);
    for b = 1:length(p)
    y2 = [y2,p(b)];
    end
   end
   y1_s = [y1_s,y2];
end
d = sum(y1_s);
Sigma = d - (c.^2);
Mu_loop1 = [Mu_loop1,Uk];
Sigma_loop1 = [Sigma_loop1,Sigma];
%%%%%%%%%%%%%%%%%%%%%%%%%%%%%%%%%%%%%%%%
TB = []; %block times of all SPAD pixels
for m = 1:1:N % N SPAD pixels are independent
     f = [];% all values from Monte Carlo Simulations
  for j = 1:1:1000 % the number of Monte Carlo Simulations
e = ceil(normrnd(Uk,Sigma,1,1));
%Generate random numbers that conform to normal distribution, and results
%are integers
    if e >= 0 && e <= Kmax
     Tb = max (Td - (rand.*(Ts - ((e-1).*Td))),0);
    f = [f Tb];
    else
    end
  end
  M = mean(f);
TB = [TB M]
end
    if loop1 == 0
        TB0 = TB
    else
        TB1 = TB;
    end
end
 %%%%%%%%%%%%%%%%%%%%%%%%%%%%%%%%%%%%%%%%
 for loopbit = 0:1:1
     if loopbit == 0;
         TB2bit = TB0;
     else
```

```
        TB2bit = TB1;
    end
 for loop2 =0:1:1
    if loop2 == 0
        lambda = lambda_0;
    else
        lambda = lambda_1;
    end
   Sigma_2 = [];
Uk_2 = [];
for o = 1:1:N
   y1_m2 = [];
   TB2 = TB2bit(1,o);
% TB2_0 = TB0(1,o);
% TB2_1 = TB1(1,o);
% TB2 = (TB2_0 + TB2_1)./2;
Ts2 = Ts - TB2;
Kmax2 =(floor(Ts2./Td) + 1);
for k2 = 0:1:(Kmax2 - 1)
lambdak1_12 = lambdak(lambda,Ts2,k2,Td);
y12 = [];
  for i2 = 0:1:k2
    psai1_12 = psai(lambdak1_12,i2);
   for a = 1:length(psai1_12)
       y12 = [y12,psai1_12(a)];
   end
  end
  y1_m2 = [y1_m2,y12];
end
c2 = sum(y1_m2);
Uk2 = Kmax2 - c2;
Uk_2 = [Uk_2,Uk2];
y1_s2 = [];
for k2 = 0:1:(Kmax2 - 1)
lambdak1_22 = lambdak(lambda,Ts2,k2,Td);
y22 = [];
  for i2 = 0:1:k2
    psai1_22 = psai(lambdak1_22,i2);
    p2 = psai1_22.*((2.*Kmax2) - (2.*k2) - 1);
   for b2 = 1:length(p2)
   y22 = [y22,p2(b2)];
   end

  end
  y1_s2 = [y1_s2,y22];
end
d2 = sum(y1_s2);
Sigma2 = d2 - (c2.^2);
Sigma_2 = [Sigma_2,Sigma2];
end
Sigma_f = sum(Sigma_2);
Uk_f = sum(Uk_2);
```

```
% Sigma_ISI = [Sigma_ISI,Sigma_f];
% Mu_ISI = [Mu_ISI,Uk_f];

if loop2 == 0
       Sigma_ISI0 = Sigma_f;
       Mu_ISI0 = Uk_f;
   else
     Sigma_ISI1 = Sigma_f;
     Mu_ISI1 = Uk_f;

end
Sigma = [Sigma,Sigma_ISI1];
     Mu = [Mu,Mu_ISI1];
SNR = BER_I(Mu_ISI1,Mu_ISI0,Sigma_ISI1,Sigma_ISI0);
BER = qfunc(SNR);

 if loopbit == 0
        BER0 = BER;
    else
        BER1 = BER;
    end
 end
 end
% pdf_normal4 = pdf('Normal',1:1:Kmax.*N,Uk_f,Sigma_f);
% plot(1:1:Kmax.*N,pdf_normal4,'LineWidth',2);hold on;
 BER_Final = [BER_Final,(plus(BER0,BER1)./2)];
% pdf_normal0 = pdf('Normal',1:1:Kmax.*N,Mu_ISI0,Sigma_ISI0);
pdf_normal1 = pdf('Normal',1:1:Kmax.*N,Mu_ISI1,Sigma_ISI1);
plot(1:1:Kmax.*N,pdf_normal1,'LineWidth',1);hold on;
% plot(1:1:Kmax.*N,pdf_normal1,'LineWidth',1);hold on;
% plot(Sigma_ISI);hold on;
% plot(Mu_ISI1);hold on;
% plot(Mu_ISI0);hold on;
end
```

PPM Modulation

```
N =; % number of SPAD Pixel
Td =; % Dead time value
% Ts =;% bit interval value
PR =;
Pb = ;
PDE =; %
h = ;v = ;% constant
BER1 = [];
bit_N = 100000;
bit = round(rand(1,bit_N)*3);

for Ts = 15.*10^-9:5.*10^-9:35.*10^-9
 k1 = [];  k2 = [];  k3 = [];  k4 = [];
 N_bit = 1;Tb1 = 0;error_bit = 0;
```

```
for N = 1:1:16
for PPM_a = bit
y1_m = [];y1_m2 = [];y1_m3 = [];y1_m4 = [];

  lambda_0 = (PDE.*Pb)./(N.*h.*v);
  lambda_1 = (PDE.*(PR+Pb))./(N.*h.*v);

  lambdak = inline('lambda.*(T-(k.*t))','lambda','T','k','t');
  psai = inline('((u.^i).*exp(-u))./factorial(i)','u','i');


    if PPM_a == 0;
      lambda1 = lambda_1;
    else
      lambda1 = lambda_0;
    end

    if PPM_a == 1;
      lambda2 = lambda_1;
    else
      lambda2 = lambda_0;
    end

    if PPM_a == 2;
      lambda3 = lambda_1;
    else
      lambda3 = lambda_0;
    end

    if PPM_a == 3;
      lambda4 = lambda_1;
    else
      lambda4 = lambda_0;
    end

%%%%%%%%% slot
Ts1 = Ts;
  Kmax1 =(floor(Ts1./Td) + 1);
 for k = 0:1:(Kmax1 - 1)
       lambdak1_1 = lambdak(lambda1,Ts1,k,Td);
        y1 = [];
   for i = 0:1:k
     psai1_1 = psai(lambdak1_1,i);
    for a = 1:length(psai1_1)
        y1 = [y1,psai1_1(a)];
    end
   end
   y1_m = [y1_m,y1];
end
c = sum(y1_m);
Uk = Kmax1 - c;
y1_s = [];
```

```
for k = 0:1:(Kmax1 - 1)
lambdak1_2 = lambdak(lambda1,Ts1,k,Td);
y2 = [];
   for i = 0:1:k
     psai1_2 = psai(lambdak1_2,i);
     p = psai1_2.*((2.*Kmax1) - (2.*k) - 1);
    for b = 1:length(p)
    y2 = [y2,p(b)];
    end
   end
   y1_s = [y1_s,y2];
end
d = sum(y1_s);
Sigma = d - (c.^2);


    %%block time%%

e1 = ceil(normrnd(Uk,Sigma,1,1));

  %%%%%%%%%%%%%% slot 2 %%%%%%%%%%%%%%%%%%

Ts2 = Ts;
  Kmax2 =(floor(Ts2./Td) + 1);
 for k = 0:1:(Kmax2 - 1)
       lambdak1_1 = lambdak(lambda2,Ts2,k,Td);
        y12 = [];
   for i = 0:1:k
     psai1_1 = psai(lambdak1_1,i);
    for a = 1:length(psai1_1)
       y12 = [y12,psai1_1(a)];
    end
   end
   y1_m2 = [y1_m2,y12];
end
c = sum(y1_m2);
Uk = Kmax2 - c;
y1_s2 = [];

for k = 0:1:(Kmax2 - 1)
lambdak1_2 = lambdak(lambda2,Ts2,k,Td);
y22 = [];
   for i = 0:1:k
     psai1_2 = psai(lambdak1_2,i);
     p = psai1_2.*((2.*Kmax2) - (2.*k) - 1);
    for b = 1:length(p)
    y22 = [y22,p(b)];
    end
   end
   y1_s2 = [y1_s2,y22];
end
d = sum(y1_s2);
```

```
Sigma = d - (c.^2);


   %%block time%%

e2 = ceil(normrnd(Uk,Sigma,1,1));
 %%%%%%%%%%%%%%%%%%%%%%%% slot 3
 Ts3 = Ts;
  Kmax3 =(floor(Ts3./Td) + 1);
 for k = 0:1:(Kmax3 - 1)
      lambdak1_1 = lambdak(lambda3,Ts3,k,Td);
       y13 = [];
   for i = 0:1:k
     psai1_1 = psai(lambdak1_1,i);
    for a = 1:length(psai1_1)
       y13 = [y13,psai1_1(a)];
    end
   end
   y1_m3 = [y1_m3,y13];
end
c = sum(y1_m3);
Uk = Kmax3 - c;
y1_s3 = [];

for k = 0:1:(Kmax3 - 1)
lambdak1_2 = lambdak(lambda3,Ts3,k,Td);
y23 = [];
   for i = 0:1:k
     psai1_2 = psai(lambdak1_2,i);
     p = psai1_2.*((2.*Kmax3) - (2.*k) - 1);
    for b = 1:length(p)
    y23 = [y23,p(b)];
    end
   end
   y1_s3 = [y1_s3,y23];
end
d = sum(y1_s3);
Sigma = d - (c.^2);
   %%block time%%
e3 = ceil(normrnd(Uk,Sigma,1,1));
%%%%%%%%%%%%%%%% slot 4
  Kmax4 =(floor(Ts4./Td) + 1);
 for k = 0:1:(Kmax4 - 1)
      lambdak1_1 = lambdak(lambda4,Ts4,k,Td);
       y14 = [];
   for i = 0:1:k
     psai1_1 = psai(lambdak1_1,i);
    for a = 1:length(psai1_1)
       y14 = [y14,psai1_1(a)];
    end
   end
   y1_m4 = [y1_m4,y14];
end
```

```
c = sum(y1_m4);
Uk = Kmax4 - c;
y1_s4 = [];
for k = 0:1:(Kmax4 - 1)
lambdak1_2 = lambdak(lambda4,Ts4,k,Td);
y24 = [];
  for i = 0:1:k
   psai1_2 = psai(lambdak1_2,i);
   p = psai1_2.*((2.*Kmax4) - (2.*k) - 1);
  for b = 1:length(p)
  y24 = [y24,p(b)];
  end
 end
 y1_s4 = [y1_s4,y24];
end
d = sum(y1_s4);
Sigma = d - (c.^2);
   %%block time%%
e4 = ceil(normrnd(Uk,Sigma,1,1));
 k1 = [k1,e1]; k2 = [k2,e2]; k3 = [k3,e3]; k4 = [k4,e4];
end
end
ks1_M = sum(reshape(k1,bit_N,N),2);
ks2_M = sum(reshape(k2,bit_N,N),2);
ks3_M = sum(reshape(k3,bit_N,N),2);
ks4_M = sum(reshape(k4,bit_N,N),2);

for PPM_a = bit

ks1 = ks1_M(N_bit,1);
ks2 = ks2_M(N_bit,1);
ks3 = ks3_M(N_bit,1);
ks4 = ks4_M(N_bit,1);
 if PPM_a == 0
    if ks1 > ks2 && ks1 > ks3 && ks1 > ks4
    else
       error_bit = error_bit +1;
    end
 end

 if PPM_a == 1
   if ks2 > ks1 && ks2 > ks3 && ks2 > ks4
    else
       error_bit = error_bit +1;
    end
 end

 if PPM_a == 2
     if ks3 > ks1 && ks3 > ks2 && ks3 > ks4
    else
       error_bit = error_bit +1;
     end
 end
```

```
  if PPM_a == 3
        if ks4 > ks1 && ks4 > ks2 && ks4 > ks3
      else
          error_bit = error_bit +1;
      end
  end
N_bit = N_bit + 1;
end
BER2 = [BER2,(error_bit ./ bit_N)];
end
semilogy(15:5:35,BER2);hold on
```

Verilog Code

```
module prbs_generator(clk, rst, random_bit);
    input clk, rst;
    output reg random_bit;
    reg [7:0] lfsr;
    always @(posedge clk or posedge rst) begin
        if (rst) begin
            lfsr <= 8'hFF; // reset the LFSR to all 1's
            random_bit <= 0;
        end else begin
            lfsr <= {lfsr[6:0], lfsr[7] ^ lfsr[6]}; // LFSR feedback tap
            random_bit <= lfsr[0];
        end
    end
endmodule
```